# Electrical Properties of Inverse Silicon Opals for Optically Enhanced Silicon Solar Cells

**by**

**Takashi Suezaki**

A thesis submitted in conformity with the requirements
for the degree of Doctor of Philosophy
Graduate School of Materials Science
Nara Institute of Science and Technology

**Electrical Properties of Inverse Silicon Opals for Optically Enhanced Silicon Solar Cells**

Takashi Suezaki

Ph. D., Graduate School of Materials Science Nara Institute of Science and Technology, 2011

# Abstract

It has just been over two decades since John and Yablonovitch theoretically predicted the existence of a complete photonic bandgap in 3D silicon photonic crystals, a range of wavelengths for which light is forbidden to propagate in all three spatial dimensions. This breakthrough inspired global research activity to transform the idea into practice, at the time driven mainly by the field of optical telecommunications. In particular, the inverse silicon opal (i-Si-o) with a high refractive index contrast has attracted a great deal of attention because of its demonstrated complete photonic bandgap at 1.5 microns and the ability to synthesize it on a large scale. While there have been many investigations of the optical properties of i-Si-o, little research has been done on its electrical behavior, the knowledge of which would underpin the development of any kind of electro-optical device founded upon i-Si-o . It is the purpose of this work presenting herein to understand the electrical properties of i-Si-o, focusing in particular on the influence of the photonic crystal lattice constant and crystallinity, the controllability of electrical properties with impurity doping and the spectral responses for the electrical properties of i-Si-o, and consequently the enhanced photoelectric generation by slow photons were firstly observed at the bandedges of photonic bands and a prototype p-i-n junction solar cell based on the inverse silicon opal was reduced to practice and its opto-electronic behavior evaluated at the first time in the world.

# Acknowledgements

I thank Professor Takashi Fuyuki for the opportunity, support and guidance to my doctoral research. More importantly, I thank his support since I entered at Graduate School of Materials Science NAIST even after finishing my master course more than 10 years ago. At my master course time, I learned much of basic knowledge of semiconductor science and approach to research, which have given me much help to work in industrial stage at Kaneka Corporation. When I got the chance to study in University of Toronto, he kindly recommended me to U of T and then after coming back to Japan he gave me the opportunity to complete the study in NAIST.

I thank Professor Geoffrey Ozin for the inspiration, freedom, support and guidance to my doctoral research. More importantly, I thank him for the unrelenting encouragements, on both scientific and personal levels, that he has provided throughout the past four years. I am further indebted to him for the great opportunity to work in such a diverse interdisciplinary research group that has widened my knowledge and perspective on materials science tremendously.

I also thank Kaneka Corporation, especially Dr. Kenji Yamamoto, for all opportunity of my doctoral research. Despite severe research and business situation, he has allowed me to keep studying such very creative and might be said “risky” work.

Several co-workers were indispensable to the completion of my doctoral work. I am deeply indebted to Dr. Jennifer I-Ling Chen for her innumerable vital suggestions that have lead to the success of my projects. I also thank her for being a great friend who continuously encouraged me, in addition to being a selfless colleague who put my interests before her own on many occasions. I thank Sue Mamiche for all her assistance to Prof. Ozin in managing group businesses and the help in some engineering aspects of my projects.

Of the other collaborators, I thank Professor Nazir Kherani and Dr. Paul O'brien for their support of electrical measurements; Edward Loso for his work on optimization for silica opal process; Ilya Gourevich, Neil Coombs and Sal Boccia for SEM and STEM; Srebri Petrov for XRD and Alexei Esmanski for silicon CVD and RIE. I also thank Susum Fukuda, Tomomi Megro, Masahiro Goto, Wataru Yoshida, Keisuke Matsumoto and Yuko Tawada for all measurement at Kaneka Corporation. I also appreciate Professor Yukiharu Uraoka, Professor Hisao Yanagi, Associate Professor Takuya Nakajima, Associate Professor Yasuaki Ishikawa for advice and guidance to my doctoral research; Assistant Professor Tomoaki Hatayama, Assistant Professor Hiroshi Yano, Hidenori Koketsu, Emi Sugimura and Tomohiro Funatani for my experiments in NAIST.

Past and present Fuyuki group, Ozin group and Kaneka members have made the last four years enjoyable and scientifically rewarding. I thank all of the support, friendship and understanding that they have provided. I shall not try to list them all. However I will mention a few who have made my first experience of living out of Japan particularly interesting and joyful. I am fortunate to have Jen as a great colleague and friend, who has taught me a great deal about photonic crystals and nano-chemistry in addition to being enthusiastic of the various sports activities, cultural exchange and weekly dine-outs. I also appreciate Edward and John for their friendship and frivolous talking, which made my English skill improve a lot, Kun and Wendong for interesting (sometimes "hard") cultural discussions, Danny, Leo and Lud for their kind invitation to thanks giving party or some others.

Lastly I thank the people who are the most important to me – my wife and daughter. I thank my wife Mayumi for her patience, understanding and support of my workaholic attitude even away from Japan. Mayumi and our daughter Yui have given me a peace of mind in pursuing my career as a scientist. I believe this experience and accomplishment will award wonderful future to my family.

# Table of Contents

## CHAPTER 1 – Introduction 1

LIST OF FIGURES

CHAPTER 1

CHAPTER 2

CHAPTER 3

CHAPTER 4

CHAPTER 5

CHAPTER 6

CHAPTER 7

LIST OF TABLES

CHAPTER 2

CHAPTER 3

# CHAPTER 1

# Introduction

## Abstract

A driving force in the rapidly developing field of photonic crystals has been the photonic bandgap, a range of energies where the propagation of light is completely forbidden. The photonic bandgap allows the design of photonic lattices that localize, guide and bend light at sub-micron length scales, providing opportunities for the creation of miniature optical devices and integrated optical circuits to help drive the revolution in photonics. A less well known attribute of photonic crystals is their ability and possibility to application for opt-electrical devices, especially for photovoltaics. This chapter introduces the theory of photonic crystal, and presents how photonic crystals can be possible to utilize for photovoltaic device applications.

## 1.1 Photonic Crystal

The idea of controlling the flow of light by structuring a material into a periodic array was independently formed by John and Yablonovitch in 1987. [1,2] These materials, known as photonic crystals, are ordered structures that have periodic-dielectric modulation (in one-, two- or three-dimension) in the length scale of the wavelength of light.[3] They can alter the propagation of light and change the interaction between light and matter. For example, constructive Bragg diffraction of light by the periodic structure gives the high iridescence of opal gem stones[4] and the color of butterfly wings[5-7] and beetle scales[8, 9].(Figure 1.1)

Aside from the natural photonic structures, the most common types of artificial photonic crystals are Bragg stack [10] (1D), rods [11] (2D), woodpile [12] (3D) and colloidal crystals [13] also referred to as opals (3D). Their structures are shown in Fig. 1.2. Bragg stacks

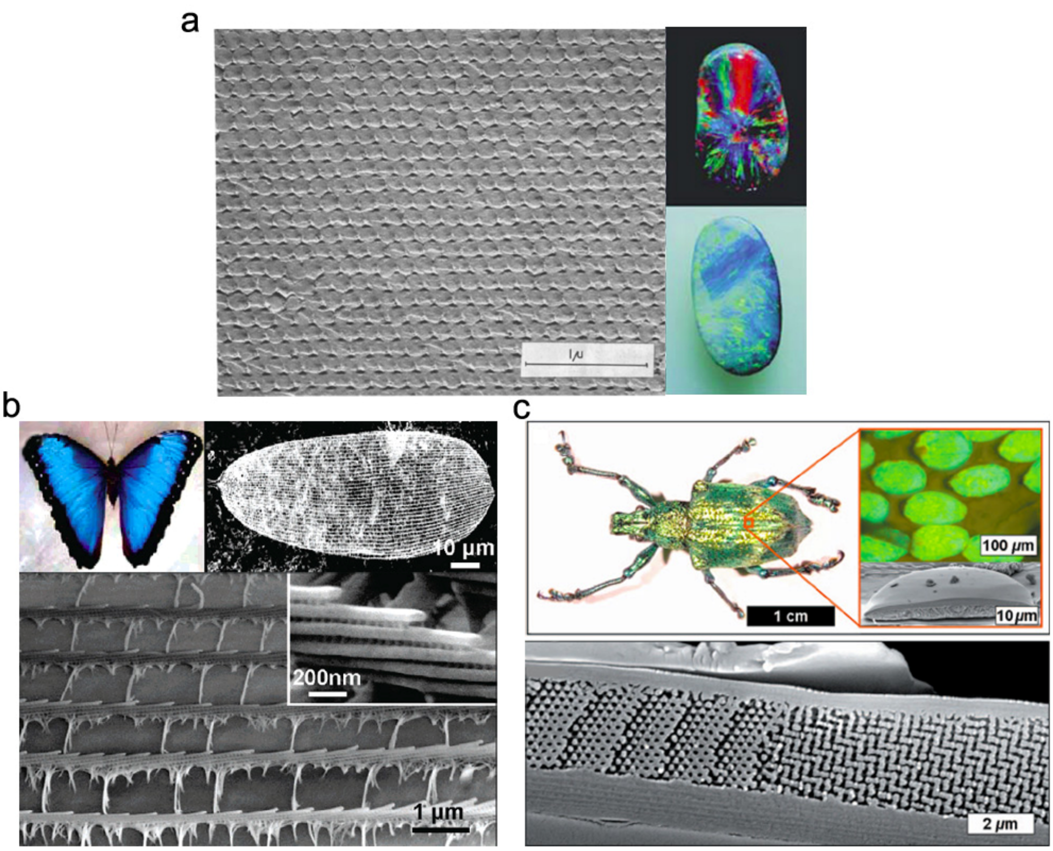

**Figure 1.1** Photographs and scanning electron images showing the submicron periodic structure of natural photonic crystals: opal gem stones (a), butterfly wings (b) and beetle scales (c). (from ref 4, 7 and 9)

have long been used as distributed Bragg reflectors in waveguides and optical fibers; they consist of alternating layers of materials with different refractive index such that light is diffracted at each layer boundary to give constructive interference. They can be fabricated via top-down approach, e.g. by sputtering or evaporation of thin films, or via bottom-up techniques, such as controlled electrochemical etching of Si [10] or spin-coating of different layers of nanoparticles.[14] Two-dimensional photonic crystal most often consists of dielectric rods in air or cylindrical holes in a material.[11, 15] Much of the earlier works on photonic crystal have focused on 2D structures owing to the ease of their fabrication using lithography. Because of the lack of periodicity along one axis, theoretical calculation is also more readily obtainable for 2D than 3D photonic crystals. Hence they are particularly valuable for studying waveguides, light localization at point defects[16] and the effect of structural disorder on photonic properties.[17, 18]

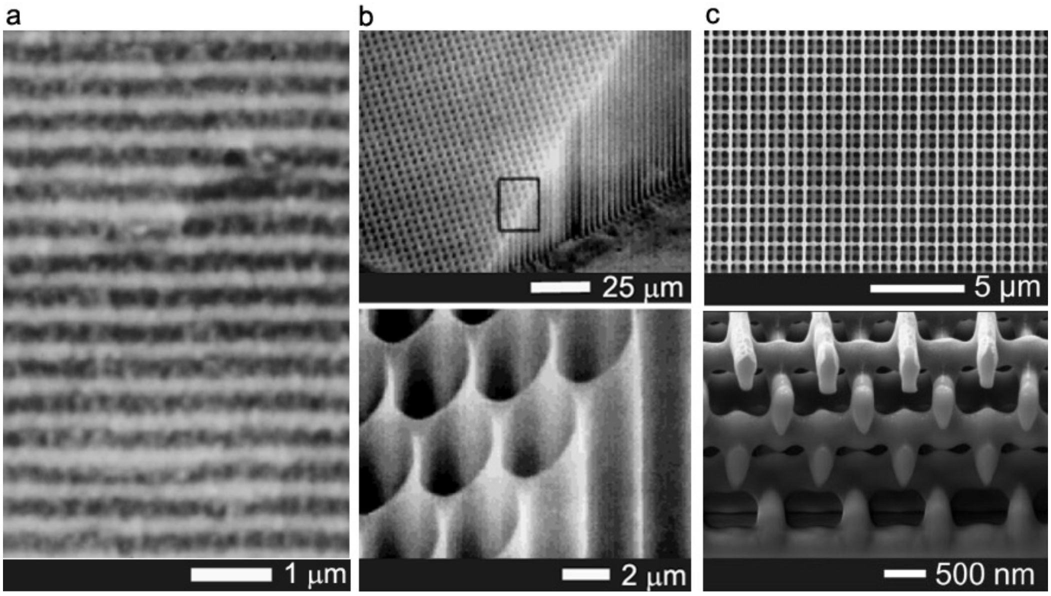

**Figure 1.2** Examples of artificial one-, two- and three-dimensional photonic crystals comprised of: alternating layers of porous Si (a); cylindrical holes in Si (b) and woodpile structure of chalcogenide sulfide (c).(from ref 10, 11 and 12)

### 1.1.1. Three-dimensional Colloidal Photonic Crystal

Three-dimensional photonic crystal is the subject of this thesis and therefore will be discussed in detail below. Although the physics of 3D photonic crystal is more complicated than that of 1D and 2D, 3D photonic crystal in the form of colloidal crystal is the most accessible photonic structure to chemists, as the building blocks are monodisperse sub-micron spheres. With the ability to synthesize highly monodisperse spheres, synthetic opals can be obtained by self-assembling the spheres into an ordered-array of cubic-closed packed colloidal crystal. The self-assembly can be induced by sedimenting the spheres or evaporating off the solvent of a solution of spheres. The former produces powders while the latter yields a single-crystal film with (111) plane parallel to the surface of a flat substrate (Fig. 1.3).[19, 20] Once an opal structure is obtained, it can be used as a template for making 3D photonic crystals of endless materials in the form of inverse opals.[21-23] To obtain inverse opals, first the voids of the opal are filled with material of interest, typically alkoxides for metal oxides like $TiO_2$ and $ZrO_2$, chemical-vapor-deposition precursors for semiconducting materials like Si, or monomers for polymeric blends. Upon solidification of the newly introduced material, the template spheres are removed to leave behind a 3D open framework that is the inverse replica of the opal. Materials of a wide range of functions have been made into photonic crystals using this method, many of which respond to different stimuli such as light[24, 25], pH[26], mechanical stress[27] and electric potential[28] or chemicals like glucose,[29] heavy metal ions[30] and gas molecules.[31] Other inorganic inverse opals have been fabricated for potential applications in batteries,[32-34] solar cells[35] and fuel cells.[36]

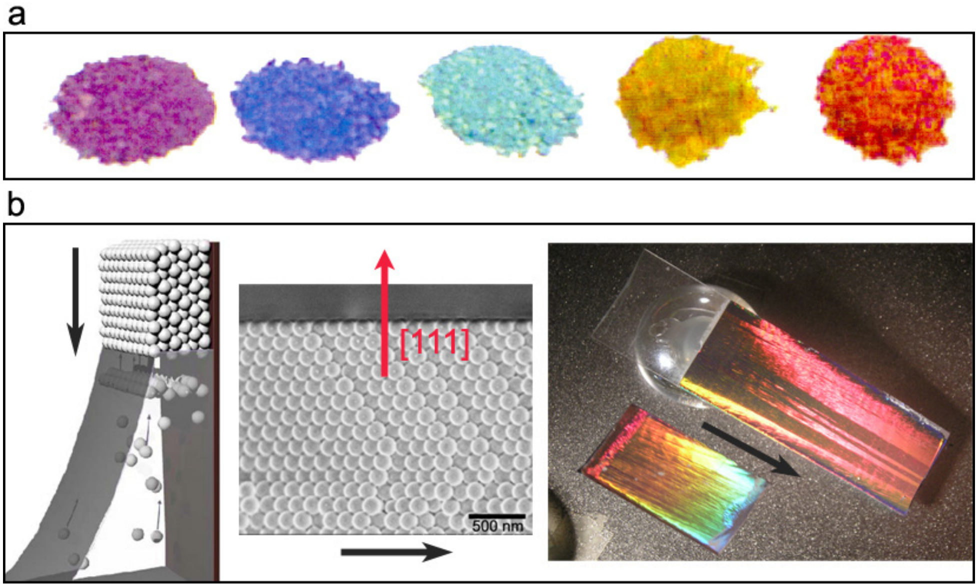

**Figure 1.3** Powders of inverse colloidal crystals of various periodicities obtained from sedimentation (a) and single-crystal opal films obtained from evaporation-induced self-assembly (b). The scheme on the left in (b) shows the deposition of spheres along the meniscus of an evaporating solvent; the ordered face-centered cubic structure can be seen in the SEM image where the [111] direction is normal to the substrate; the resultant opalescence is shown in the photograph on the right. The black arrows indicate the direction of the growth of the films.(from ref 22)

Thin films of opal and inverse opal with sphere sizes ~150 nm to 1 μm show vivid colors, which can be explained based on a combination of Bragg's law of constructive interference in diffraction

$$n\lambda = 2d\sin\theta \tag{1.1}$$

and Snell's law of refraction of light

$$\frac{n_1}{n_2} = \frac{\sin \alpha}{\sin \beta} \tag{1.2}$$

Note that by definition the angle θ is with respect to the normal of the film, while α and β are with respect to the surface of the medium. Therefore, by using cosine law to equate α and β to the normal of the film, the modified Bragg's equation becomes

$$n\lambda = 2d\sqrt{n_{eff}^2 - \sin^2 \theta} \tag{1.3}$$

where n is 1 (for fundamental stop band as explained in the following section), d is the (111) interplanar distance, θ is the angle between incident beam and the normal of the film, and $n_{eff}$ is the effective refractive index approximated by

$$n_{eff} = fn_{sphere} + (1 - f)n_{void} \tag{1.4}$$

with f being the filling fraction of the face-centered cubic structure (f = 0.74). Equation 1.3 accurately determines the wavelength of the reflected light by opals and also provides a facile way to monitor the filling of the pores of the opal during the inversion process.

In addition to mimicking structural color, the artificial photonic crystals are designed to control other properties of light such as localizing the electromagnetic field or reducing the group velocity of light within the photonic crystal to enhance light-matter interactions. To better understand these phenomena, fundamental understanding of photonic band diagram is needed.

## 1.2 Theory of Photonic Band Diagram

The photonic properties are described by a photonic band diagram, just as electronic properties are described by an electronic band diagram. Like any other macroscopic electromagnetic event, the propagation of light in photonic crystal is governed by the four macroscopic Maxwell's equations.[3] They are

$$\nabla \bullet B = 0 \tag{1.5a}$$

$$\nabla \bullet D = 4\pi\rho \tag{1.5b}$$

$$\nabla \times E + \frac{1}{c}\frac{\partial B}{\partial t} = 0 \tag{1.5c}$$

$$\nabla \times H - \frac{1}{c}\frac{\partial D}{\partial t} = \frac{4\pi}{c}J \tag{1.5d}$$

where c is the speed of light, E and H are the electric and magnetic fields, B and D are the displacement and magnetic induction field, and ρ and J are the free charges and currents that can be assumed as zero. In most cases, magnetic permeability is close to unity so that B = H; also, the displacement field, D(r), can be approximated as ε(r)E(r) where ε(r) is the dielectric constant. Then equations 1.5a – 1.5d become

$$\nabla \bullet H(r,t) = 0 \tag{1.6a}$$

$$\nabla \bullet \varepsilon(r)E(r,t) = 0 \tag{1.6b}$$

$$\nabla \times E(r,t) + \frac{1}{c}\frac{\partial H(r,t)}{\partial t} = 0 \tag{1.6c}$$

$$\nabla \times H(r,t) - \frac{\varepsilon(r)}{c}\frac{\partial E(r,t)}{\partial t} = 0 \tag{1.6d}$$

Note that the assumptions and approximations have restricted the photonic structure to be lossless and linear in optical response. Next, the fields described by Maxwell's equations can be written as harmonic modes that vary sinusoidally with time so that H and E can be written as

$$H(r,t) = H(r)e^{i\omega t} \tag{1.7}$$

$$E(r,t) = E(r)e^{i\omega t} \tag{1.8}$$

Substituting these expressions of H and E into equations 1.6a – 1.6d gives

$$\nabla \times E(r) + \frac{1}{c} H(r) = 0 \tag{1.9}$$

$$\nabla \times H(r) - \frac{i\omega}{c} \varepsilon(r) E(r) = 0 \tag{1.10}$$

where E(r) can now be expressed in terms of H(r). With some rearrangement, the result is an equation that is entirely governed by H(r).[37, 38]

$$\nabla \times \left( \frac{1}{\varepsilon(r)} \nabla \times H(r) \right) = \left( \frac{\omega}{c} \right)^2 H(r) \tag{1.11}$$

This master equation shows that the electromagnetism is an Eigenvalue problem where the operation on a function yields the function itself multiplied by a constant. To solve this differential equation, plane-wave expansion method based on the Bloch-Floquent theorem is used. The theorem suggests that the Eigen solutions of differential equations with periodic coefficients may be expressed as a product of plane waves and lattice periodic functions. The solutions obtained are plotted as a photonic band diagram; an example is shown in Fig. 1.4. The photonic band diagram summarizes the dispersion relation between the energy of light and the wave vector k in the reciprocal lattice. The energy is often expressed as ωa/2πc (a is the unit cell length and ω is the angular frequency) while k has a magnitude of 2π/λ in k direction within the Brillouin zone.

### 1.2.1. Group Velocity and Density of States

From the photonic band diagram two important properties can be derived: the group velocity of light ($\upsilon_g$) and the density of states (DOS). The former is defined as ∂ω/∂k (i.e. the derivative of the dispersion relation) while the latter is the integral of Bloch states of a chosen frequency over the Brillouin zone. Not only can total density of states be calculated, but local

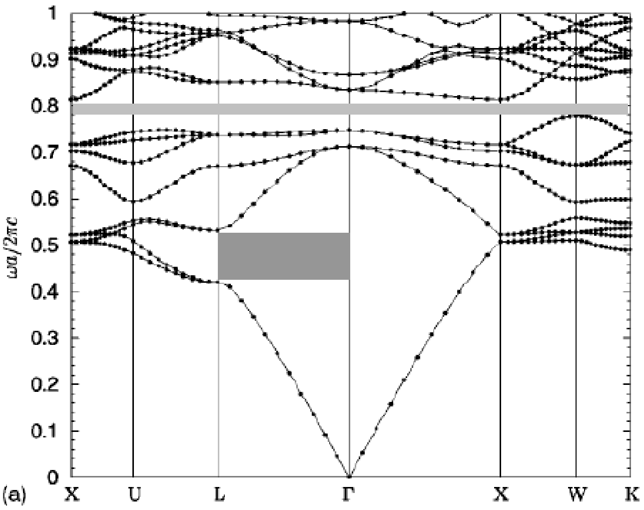

**Figure 1.4** Photonic band diagram of an inverse Si opal showing the dispersion relation between energy of light and the wave vector. The light-grey shaded area indicates the complete bandgap while the dark-grey shaded area indicates one of the stop bands in this structure. (from ref 39)

density of states at a specified region of the photonic crystal can also be calculated.[39] As a result, information on the energy and spatial distribution of the electromagnetic field within the periodic structure can be obtained. An example of the total vs local density of states of a photonic structure for different energy of light is shown in Fig. 1.5. For this non-closed-packed face-centered structure, the DOS at lower energy are concentrated in the background medium while the DOS at the higher energy are localized on the dielectric spheres. The distribution of electromagnetic field can further be numerically characterized by the confinement factor, which is the ratio of local DOS over total DOS at some frequency and wave vector.[40]

When the DOS are depleted for some range of frequency, the corresponding energy of light cannot propagate through the photonic crystal. When this energy gap persists throughout all directions, it is referred to as the photonic bandgap; an example of such a complete bandgap is found between the 8th and 9th bands for an inverse Si opal[41], as indicated by the light-grey shaded area in Fig. 1.4. On the other hand, most photonic crystals only have vanishing DOS for a specific direction of light propagation. These gaps are known as photonic stop bands, an example of which can also be found in the Γ-L Brillouin zone in Fig. 1.4 (dark-grey shaded area). In cubic-closed-packed colloidal photonic crystal, stop bands are a result of light diffraction from the (111) planes. The position of this fundamental stop band can also be calculated using Bragg's law (equation 1.3).

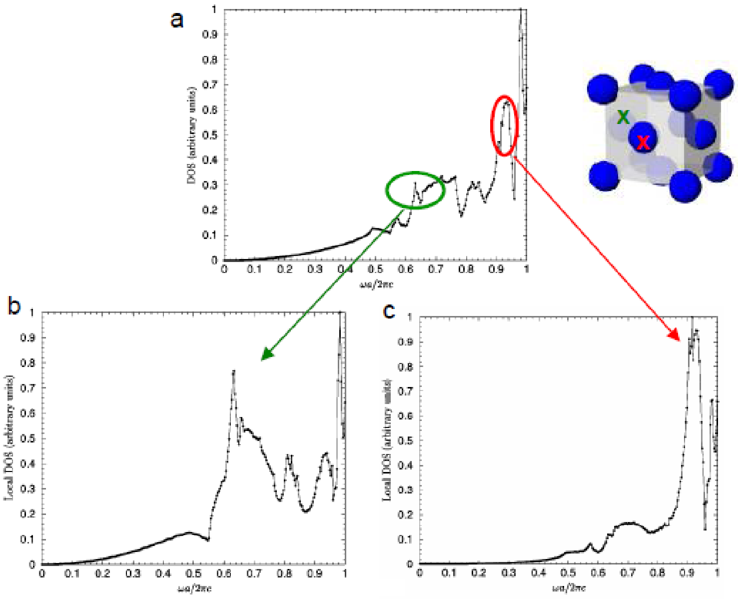

**Figure 1.5** A comparison of total DOS (a) and local DOS (b and c) for a fcc structure of TiO2 spheres in water. The local DOS calculated at midway between two adjacent spheres (b) and at the center of sphere (c). The filling fraction of TiO2 is 25%. (from ref 39)

The other important property derived from the photonic band diagram is $\upsilon_g$, in particular the slow-photon phenomenon that arises at energies near the edges of photonic stop band. Slow photon can be perceived as a transition between full transmission of light with energy outside of the photonic band gap to the full attenuation of light with energy within the band gap. With photonic bands flattening out as Bloch states vanish near the band gap, light propagates at a reduced group velocity as $\partial\omega/\partial k$ approaches 0 theoretically. This phenomenon effectively increases the optical path length of light and the interaction of light with the material. If the material is photoactive, changes in fundamental properties like absorption may occur as a result of slow photons. To better understand the impact of the reduced light group velocity on the gain and loss of the material, a dynamical treatment to the propagation of an envelope of light is required.

### 1.2.2. Absorption and Non-linear Optical Properties in Photonic Crystal

As mentioned above, the calculation of the photonic band diagram generally assumes linear, non-dispersive and lossless material. In other words, the dielectric constant of the photonic crystal is energy-independent and the absorption of light is absent. To account for any absorption or non-linearity that may arise during the propagation of an envelope of light, a dynamical treatment using Maxwell's and Schrödinger's equations was performed by Bhat and Sipe.[42] After extensive mathematical derivation, they arrive at:

$$\frac{\partial\Psi(s)}{\partial t}+\upsilon_g(\vec{k})\frac{\partial\Psi(s)}{\partial s}=\frac{1}{2}i\frac{\partial^2\omega}{\partial^2 k}\frac{\partial^2\Psi(s)}{\partial^2 s}+i\omega\sigma\Psi(s)+i\frac{\alpha}{\varepsilon_0\upsilon_g(\vec{k})}\Psi(s)\left|\Psi(s)\right|^2 \qquad (1.12)$$

for a wave packet moving in the ŝ direction through the photonic crystal. Ψ is the Schrödinger's envelope function of the field, $\upsilon_g$ is the group velocity as before, and $\varepsilon_o$ is the permittivity in vacuum. The dynamical treatment now modifies the solutions in terms of two important factors: dielectric-dispersion and non-linearity of the material. First, the effective index modification to the linear optical properties is represented by σ, which is defined as

$$\sigma=\frac{1}{2}\int\frac{d^3r}{\Omega_{cell}}\frac{\varepsilon_c(\vec{r})}{\varepsilon_0}\left|E_{\alpha\vec{k}}(\vec{r})\right|^2 \qquad (1.13)$$

where $\varepsilon_c$ is the corrective dielectric constant that has both real and imaginary parts. Second, the non-linearity, which may arise due to localization of electromagnetic field, is taken into account by α, also known as the effective Kerr coefficient. It again is an integral of functions in Maxwell's equations and other variables (the details of which can be found in ref. 40).

Now suppose the field is time independent and group velocity dispersion ($\partial^2\omega/\partial k^2$)

and non-linearity are negligible, equation 1.12 simplifies to

$$\upsilon_g(\vec{k})\frac{\partial\Psi(s)}{\partial s} = i\omega\sigma\Psi(s) \qquad (1.14)$$

By writing

$$\Psi(s) = \Psi(0)\exp\left[i\tilde{n}(\omega s)/c\right] \qquad (1.15)$$

we arrive at the following relationship

$$\tilde{n} = \sigma\left(\frac{c}{\upsilon_g(\vec{k})}\right) \qquad (1.16)$$

where ñ is the effective refractive index. In other words, the normal refractive index of a material upon being incorporated into a photonic structure will now be altered to ñ. The real part of ñ is associated with changes in effective phase velocity while the imaginary part describes the effect of gain or loss on propagation. Equation 1.16 shows that ñ is inversely proportional to $\upsilon_g$; it suggests that absorption, which is governed by the imaginary part of ñ may be significantly increased for light traveling at reduced group velocity. This derivation is very important for photovoltaic applications.

## 1.3 Recent Progress on Incorporating Photonic Structures in Photovoltaic Applications

Most photovoltaic (solar) cells are made from crystalline silicon (c-Si), which has an indirect band gap. This gives rise to weak absorption of one-third of usable solar photons. Therefore, improved light trapping schemes are needed, particularly for c-Si thin film solar cells. 1D photonic crystal, also called ‘Bragg Stacks’, has dielectric contrasts one dimensionally and that is able to achieve perfect mirror at certain controllable wavelength range. As a example, porous silicon layers have been successfully applied to maximize internal reflection at the interface between a silicon substrate and an epitaxially grown layer.[42] The stack is consist of alternating porous layers of high and low porosity, defined by the quarter-wavelength rule. During the hydrogen bake prior to epitaxial growth of the epitaxial layer, the porous silicon stack crystallizes in the form of thin quasi-monocrystalline silicon layers incorporating large voids. Experimental data of the measured external reflectance have been linked to the internal reflectance. An optical-path-length enhancement factor of seven was calculated in the wavelength range of 900–1200 nm. Application on thin-film epitaxial solar cells showed a 12% increase in short-circuit current and efficiency.

Not only 1D but also 2D back reflector has been investigated.[43-46] A 1D photonic crystal or distributed Bragg reflector (DBR) with alternating dielectric layers acts as low loss back reflector. A 2D photonic crystal between the absorber layer and the Bragg reflector diffracts light at oblique angles within the absorber. The photonic crystal geometry is optimized to obtain maximum absorption. The photonic crystal provides lossless diffraction of photons, increasing the photon path length within the absorber layer. The simulation predicts significantly enhanced photon harvesting below the band edge, and an absorption increase by more than a factor of 10 near the band edge. The optical path length ratio can exceed the classical limit predicted for randomly roughened scattering surfaces at most wavelengths near the band edge.

As an another approach, vertically aligned silicon nanowire solar cells (Si NW SCs) have already been shown theoretically to be much less sensitive to impurities versus planar Si SCs. Erik C. Garnett et. al reported the fabrication of wafer-scale arrays of n-type Si NWs with a solution-phase etching method, deposition of p-type amorphous Si (a-Si) using low pressure chemical vapor deposition (LPCVD) and subsequent crystallization with rapid thermal annealing (RTA). [47] That yielded core-shell n-p junction Si NW array SCs fabricated using only low-energy, scalable processes. The reported efficiency was about 0.5%, but further optimization has been undergoing.

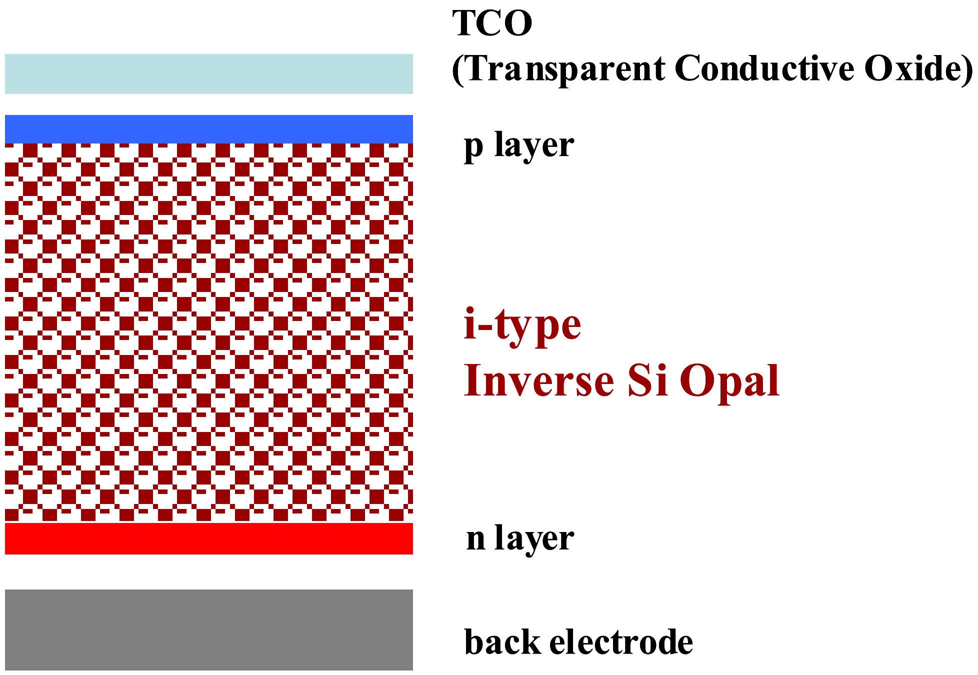

**Figure 1.6** A schematic diagram of the structure of the concept of optically enhanced silicon photonic crystal solar cell

## 1.4 New Concept of Optically Enhanced Silicon Photonic Crystal Solar Cells

Most studies for incorporating photonic structures in solar cells have applied 1D or 2D or 3D photonic crystals for back side reflector. However, the concept presenting in this thesis is quite different and unique. In that concept, inverse silicon opal is applied to active photo-generation layer for solar cells. Figure 1.6 shows a sketch of the structure of this concept. The active layer, composed with inverse silicon opal, enhance the photo-generation by two means. One is setting photonic band gap (PBG) around 950 nm in which air moisture absorbs solar radiation, therefore even PBG reflect the light around 950 nm, it doesn’t decrease photons going into solar cells and in contrast it's possible to enhance photon absorption higher at the edge of PBG by slow photon effect. The other one is more challenging, that utilize the complete PBG to inhibit of emission for carrier recombination for letting photo-generated carriers' life time longer. This idea is still hypothesis, however Jia et.al reported the sign of this effect in a study for photo-luminescence of PbSe quantum dots infiltrated into 3D photonic crystals. [48] They have observed that the photo-luminescence was suppressed by the stop gap effect.

## 1.5 References

[1] E. Yablonovitch, Phys. Rev. Lett. 1987, 58, 2059.

[2] S. John, Phys. Rev. Lett. 1987, 58, 2486.

[3] J. D. Joannopoulos, P. R. Villeneuve, S. Fan, Nature 1997, 386, 143.

[4] J. V. Sanders, Acta Crystallogr., Sect. A: Found. Crystallogr. 1968, 24, 427.

[5] L. P. Biro, Z. Balint, K. Kertesz, Z. Vertesy, G. I. Mark, Z. E. Horvath, J. Balazs, D. Mehn, I. Kiricsi, V. Lousse, J. P. Vigneron, Phys. Rev. E 2003, 67.

[6] P. Vukusic, R. Sambles, J. Soc. Dyers Colour. 2000, 116, 376.

[7] J. Y. Huang, X. D. Wang, Z. L. Wang, Nano Lett. 2006, 6, 2325.

[8] A. R. Parker, V. L. Welch, D. Driver, N. Martini, Nature 2003, 426, 786.

[9] J. W. Galusha, L. R. Richey, J. S. Gardner, J. N. Cha, M. H. Bartl, Phys. Rev. E 2008, 77, 050904.

[10] V. Agarwal, J. A. del Rio, Appl. Phys. Lett. 2003, 82, 1512.

[11] A. Birner, U. Gruning, S. Ottow, A. Schneider, F. Muller, V. Lehmann, H. Foll, U. Gosele, Phys. Status Solidi A 1998, 165, 111.

[12] S. Wong, M. Deubel, F. Perez-Willard, S. John, G. A. Ozin, M. Wegener, G. von Freymann, Adv. Mater. 2006, 18, 265.

[13] S. Wong, V. Kitaev, G. A. Ozin, J. Am. Chem. Soc. 2003, 125, 15589.

[14] S. Colodrero, M. Ocana, H. Miguez, Langmuir 2008, 24, 4430.

[15] W. M. Robertson, G. Arjavalingam, R. D. Meade, K. D. Brommer, A. M. Rappe, J. D. Joannopoulos, J. Opt. Soc. Am. B: Opt. Phys. 1993, 10, 322.

[16] E. Yablonovitch, T. J. Gmitter, R. D. Meade, A. M. Rappe, K. D. Brommer, J. D. Joannopoulos, Phys. Rev. Lett. 1991, 67, 3380.

[17] D. M. Beggs, M. A. Kaliteevski, R. A. Abram, D. Cassagne, J. P. Albert, J. Phys.: Condens. Matter 2005, 17, 1781.

[18] M. A. Kaliteevski, J. Manzanares Martinez, D. Cassagne, J. P. Albert, Phys. Rev. B 2002, 66, 1131011.

[19] P. Jiang, J. F. Bertone, K. S. Hwang, V. L. Colvin, Chem. Mater. 1999, 11, 2132.

[20] D. M. Mittleman, J. F. Bertone, P. Jiang, K. S. Hwang, V. L. Colvin, J. Chem. Phys. 1999, 111, 345.

[21] J. E. G. J. Wijnhoven, W. L. Vos, Science 1998, 281, 802.

[22] R. C. Schroden, M. Al-Daous, C. F. Blanford, A. Stein, Chem. Mater. 2002, 14, 3305.

[23] A. Stein, R. C. Schroden, Curr. Opin. Solid State Mater. Sci. 2001, 5, 553.

[24] M. K. Maurer, I. K. Lednev, S. A. Asher, Adv. Func. Mater. 2005, 15, 1401.

[25] M. Kamenjicki, I. K. Lednev, A. Mikhonin, R. Kesavamoorthy, S. A. Asher, Adv. Func. Mater. 2003, 13, 774.

[26] K. Lee, S. A. Asher, J. Am. Chem. Soc. 2000, 122, 9534.

[27] A. C. Arsenault, T. J. Clark, G. von Freymann, L. Cademartiri, R. Sapienza, J. Bertolotti, E. Vekris, S. Wong, V. Kitaev, I. Manners, R. Z. Wang, S. John, D. Wiersma, G. A. Ozin, Nature Mater. 2006, 5, 179.

[28] A. C. Arsenault, D. P. Puzzo, I. Manners, G. A. Ozin, Nature Photonics 2007, 1, 468.

[29] M. Ben-Moshe, V. L. Alexeev, S. A. Asher, Anal. Chem. 2006, 78, 5149.

[30] A. V. Goponenko, S. A. Asher, J. Am. Chem. Soc. 2005, 127, 10753.

[31] K. W. Kimble, J. P. Walker, D. N. Finegold, S. A. Asher, Anal. Bioanal. Chem. 2006, 385, 678.

[32] N. S. Ergang, J. C. Lytle, K. T. Lee, S. M. Oh, W. H. Smyrl, A. Stein, Adv. Mater. 2006, 18, 1750.

[33] K. T. Lee, J. C. Lytle, N. S. Ergang, S. M. Oh, A. Stein, Adv. Func. Mater. 2005, 15, 547.

[34] J. Lee, W. Choi, J. Phys. Chem. B 2005, 109, 7399.

[35] S. Nishimura, N. Abrams, B. A. Lewis, L. I. Halaoui, T. E. Mallouk, K. D. Benkstein, J. Van de Lagemaat, A. J. Frank, J. Am. Chem. Soc. 2003, 125, 6306.

[36] G. A. Umeda, W. C. Chueh, L. Noailles, S. M. Haile, B. S. Dunn, Energy Environ. Sci. 2008, 1, 484.

[37] S. Satpathy, Z. Zhang, M. R. Salehpour, Phys. Rev. Lett. 1990, 64, 1239.

[38] K. M. Ho, C. T. Chan, C. M. Soukoulis, Phys. Rev. Lett. 1990, 65, 3152.

[39] K. Busch, S. John, Phys. Rev. E 1998, 58, 3896.

[40] R. D. Meade, A. M. Rappe, K. D. Brommer, J. D. Joannopoulus, J. Opt. Soc. Am. B: Opt. Phys. 1993, 10, 328.

[41] A. Blanco, E. Chomski, S. Grabtchak, M. Ibisate, S. John, S. W. Leonard, C.

[42] F. Duerinckx, I. Kuzma-Filipek, K. Van Nieuwenhuysen, G. Beaucarne, and J. Poortmans, IEEE ELECTRON DEVICE LETTERS, VOL. 27, NO. 10, OCTOBER 2006

[43] D. Zhou and R. Biswas, J. Appl. Phys. 103, 093102, 2008

[44] P. Bermel, C. Luo, L. Zeng, L. C. Kimerling and J. D. Joannopoulos, OPTICS EXPRESS 16986, Vol. 15, No. 25, 2007

[45] L. Zeng, P. Bermel, Y. Yi, N. Feng, B. A. Alamariu, C. Hong, X. Duan, J. Joannopoulos and L. C. Kimerling, Mater. Res. Soc. Symp. Proc. Vol. 974, CC02-06, 2007

[46] P. G. O'Brien, N. P. Kherani, S. Zukotynski, G. A. Ozin, E. Vekris, N. Tetreault, A. Chutinan, S. John, A. Mihi, and H. Míguez, Adv. Mater. 2007, 19, 4177–4182

[47] E. C. Garnett and P. Yang, J. Am. Chem. Soc., 2008, 130 (29), pp 9224–9225

[48] J. Li, B. Jia, G. Zhou, C. Bullen, J. Serbin, and M. Gu, Adv. Mater. 2007, 19, 3276–3280

# CHAPTER 2

## Inverse Crystalline Silicon Opals (i-cSi-o)

### Abstract

The inverse opal structure has been getting great attentions since its interesting feature that is possibility of possessing complete photonic band gap. In particular, the inverse silicon opal (i-Si-o) with a high refractive index contrast has attracted a great deal of attention because of its demonstrated complete photonic bandgap at 1.5 microns and the ability to be synthesized on a large scale. While there have been many reports of the fabrication of inverse “amorphous” silicon opal (i-aSi-o), little research has been done on inverse “crystalline” silicon opal (i-cSi-o), which should have more advantages for electrical device application than that of amorphous one because the crystalline silicon materials have higher majority carriers’ mobility and longer minority carriers’ lifetime. This chapter provides the detail procedure of i-cSi-o and the method for analysis its properties.

### 2.1 Introduction

It has just been over two decades since John and Yablonovitch theoretically predicted the existence of a complete photonic bandgap in 3D silicon photonic crystals [1.2], a range of wavelengths for which light is forbidden to propagate in all three spatial dimensions. In particular, the inverse silicon opal (i-Si-o) with a high refractive index contrast has attracted a great deal of attention because of its demonstrated complete photonic band gap at 1.5 microns and the ability to synthesize it on a large scale. [3] In fact, the progress of this field has required strategies for the efficient synthesis of high quality, large-scale i-Si-o with photonic band gaps at micrometer and sub-micrometer wavelengths. Since i-Si-o with a complete three-dimensional photonic band gap, produced by growing silicon inside the voids of an opal template of close-packed silica spheres that are connected by small `necks' formed during sintering, followed by removal of the silica template, we have been free from complex lithographic procedures which resulted in a thickness of only two unit cells in the growth direction. [4]

However, the silicon matrix on i-Si-o fabricated with the standard method is actually amorphous silicon and little research for crystalline silicon which has many advantages for electrical applications.

In this chapter, the detail process for inverse silicon opal based on well known standard method is explained and the way for new attempt to obtain inverse “crystalline” silicon opal is presented.

## 2.2 Experimental Methods

### 2.2.1. Fabrication of Silica Opal

#### 2.2.1.1. Silica Microsphere

Monodisperse silica microspheres are made by the Stöber [5] or modified Stöber process involving the base catalyzed hydrolytic polycondensation of tetraethoxyorthosilicate:

$$Si(OEt)_4 + 2H_2O \rightarrow SiO_2 + 4EtOH$$

The single stage process is limited to microsphere sizes below 700-800 nm while the re-growth process extends to 3-4 µm.

In this work, ammonium hydroxide was used as a catalyser for the reaction of silica microspheres synthesis. Since the supreme purpose of this work is an application of inverse silicon opal for solar cell, silica microspheres with diameters between 145 nm and 700 nm were prepared.

#### 2.2.1.2. Silica Opal - Microsphere Self-Assembly

Silica Opal is the material that has a face centered cubic structure formed by monodisperse silica microspheres and that is used as a template for inverse silicon opal. In order to form the silica opal templates, the evaporation induced self-assembly (EISA) method was employed, shown in Figure 2.1, in which a substrate is placed vertically in a dispersion of silica microspheres in ethanol.[6] As the ethanol evaporates, the silica microspheres are driven by convective forces to the meniscus, whereby they are coerced by capillary forces to self-assemble into an opal film, with a layer thickness determined by the microsphere diameter, volume concentration, and the wetting properties of the ethanol on the substrate of interest. To grow films of silica microspheres with diameter larger than 450 nm, an accelerated evaporation must be employed to counter rapid sedimentation. Both heat [4,7] and vacuum [8] can be used for this purpose.

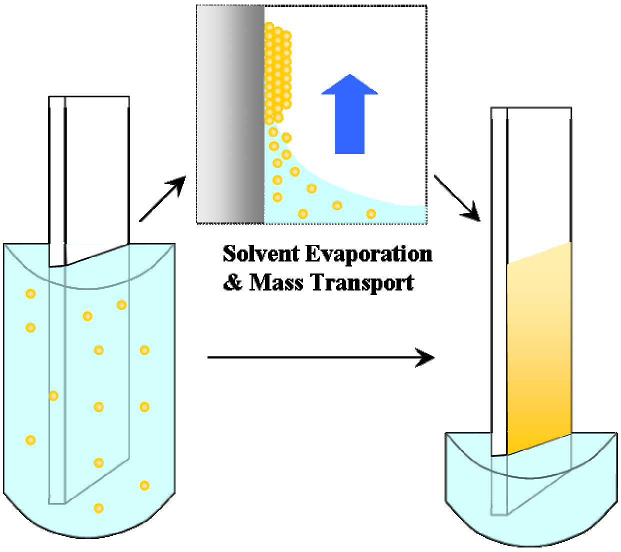

**Figure 2.1** Schematic diagram of EISA

Figure 2.2 shows the schematic diagram of actual set up for EISA in this work. Substrates were cleaned by piranha solution; consisted with sulfuric acid (96%) and hydrogen peroxide (30%) in the ratio of three to one; before silica opal film formation. A substrate was set vertically in vial which has well dispersed silica microspheres solution by clips (a). As mentioned, there are two way, for small sphere (b) and large sphere (c). For small sphere, the process room was controlled at 30 ˚C and the vials were placed on a vibration isolation system to keep meniscus stable. In addition, to remove the effect of air stream or physical contact, the vials were covered by large glassware with a space not to seal. For large sphere, the vials were placed in a vacuum desiccator on a vibration isolation. The vacuum desiccator was connected to a vacuum pump and a vacuum gauge through Tygon tube as vacuum line, which has a needle valve for manipulate pumping speed.

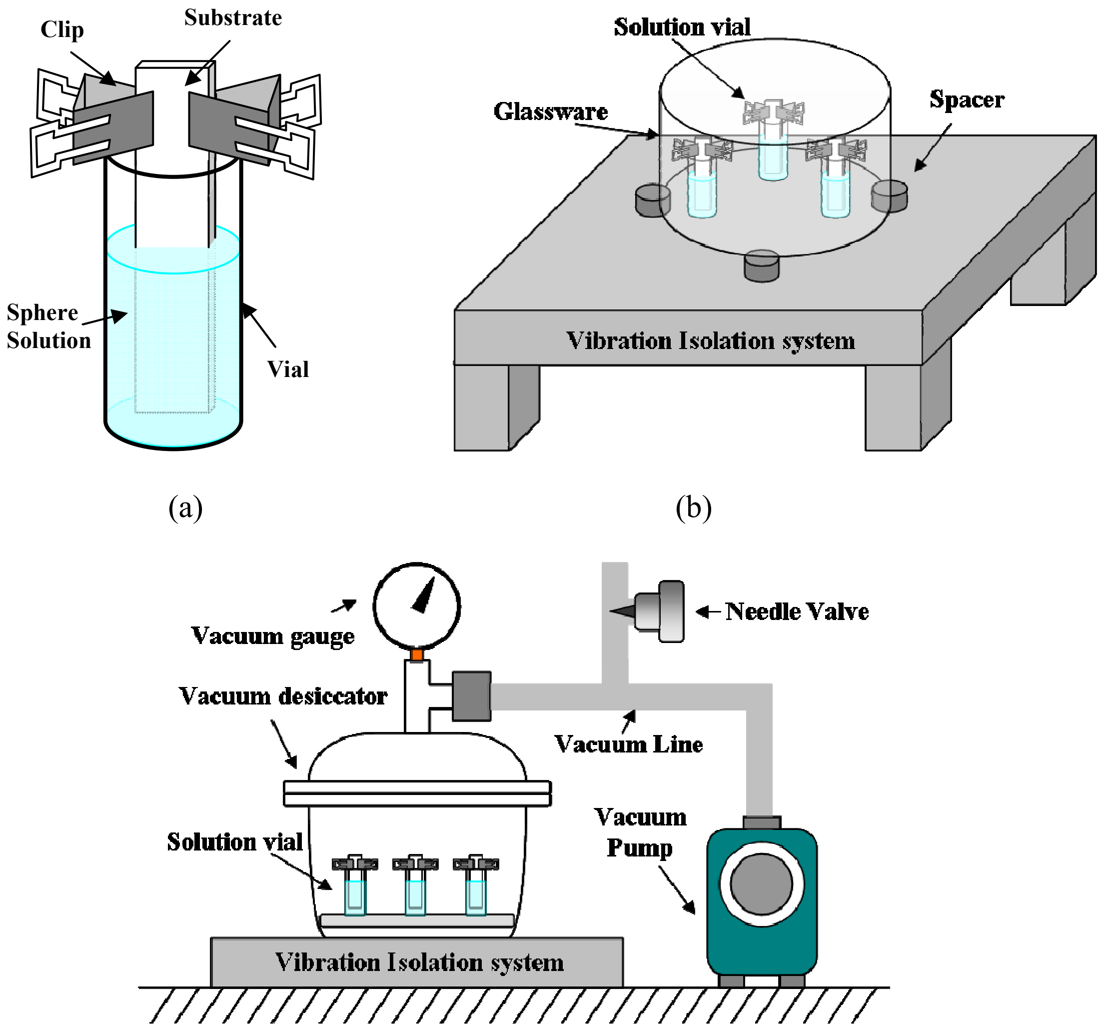

(a) (b)

(c)

**Figure 2.2** The schematic diagram of experimental set up of substrate & sphere solution (a), small silica microsphere (b) and large silica microsphere (c) for EISA in this work

Table 2.1 shows the each condition for preparation of silica opals. Every solution contained 5 vol % water to improve opal formation. Sonication time is the length for dispersion of source solution after preparation in a water bath sonicator. Process pressure; strongly related to evaporation speed; is controlled by the needle valve and very important to obtain good structural order. Basically slow forming speed is better for opal preparation because of less probability for sphere aggregation. However, to avoid silica microspheres sedimentation, evaporation speed must be faster than sedimentation speed that is relative to sphere weight. Therefore, the evaporation speed was optimized for each sphere size.

**Table 2.1** EISA condition for silica opal preparation of each sphere size.

| spher size nm | substrate | process | press torr | soltion vol ml | H2O vol% | sphere wt % | sonication hours |
|---|---|---|---|---|---|---|---|
| 300 | glass | a | atmospheric | 8 | 5 | 2.55 | 5 |
| 390 | glass | a | atmospheric | 8 | 5 | 2.77 | 5 |
| 470 | glass | b | 40 | 8 | 5 | 3.79 | 5 |
| 600 | glass | b | 45 | 8 | 5 | 2.54 | 8 |

Figures 2.3 are a typical appearance (a) and a scanning electron microscopy image (b) of silica opal film. Figure 2.4 is reflectance spectra for silica opals formed by each sphere sizes. Every reflectance spectrum of silica opal shows the stop-band reflection at 689, 902, 1034 and 1396 nm respectively with well defined peaks from higher energy bands. Each stop-band positions were well matched for theoretical calculation (formula (1.3), (1.4)). Not only theoretically well matched stop-band but also small reflections from Fabry-Pèrot interference at lower energy range than stop band energy [9] was another evidence of a highly ordered opal lattice.

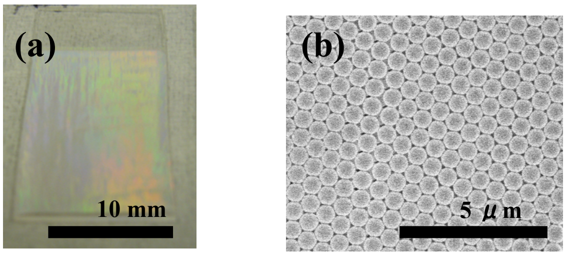

**Figure 2.3** A typical appearance (a) and a SEM image (b) of silica opal film.

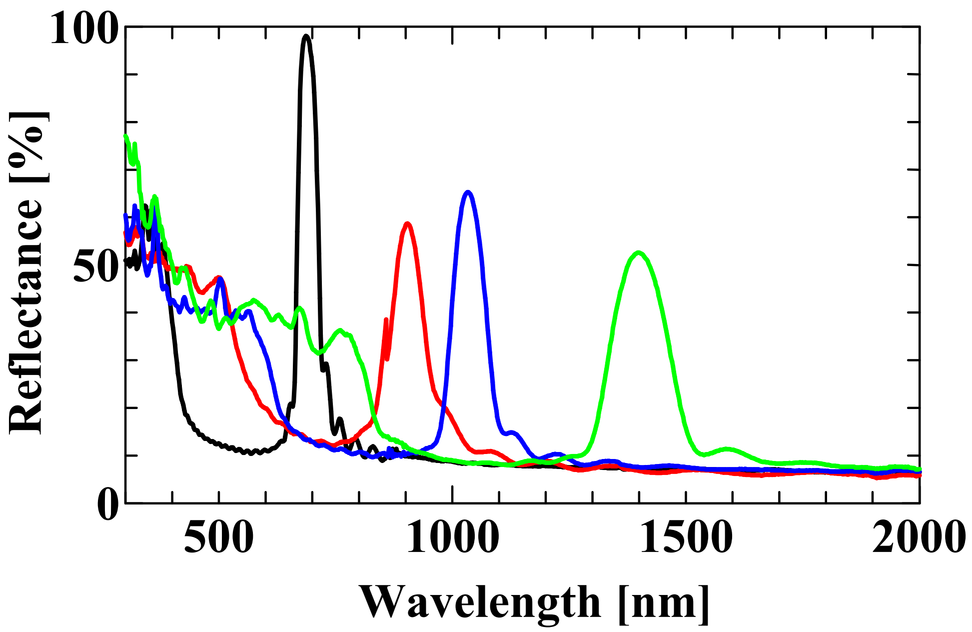

**Figure 2.4** Reflectance spectra for silica opals formed by microspheres with diameter of 300 nm (black), 390 nm (red), 470 nm (blue) and 600 nm (light green).

### 2.2.2. Fabrication of Inverse Silicon Opal

#### 2.2.2.1. Silicon Infiltration

The inverse silicon opal is the 3D silicon photonic crystal made by bottom-up self-assembly with a complete PBG. It presents a face centered cubic photonic lattice of interconnected air spheres in a silicon matrix. The inverse silicon opal is made by the CVD of silicon by thermal decomposition of disilane within the interstitial voids of silica opal template. It is very important for silicon infiltration within the interstitial voids to form silicon part omni-directionally, otherwise some voids space are clogged and stop source gas supply during silicon deposition at other voids space. Therefore, plasma enhanced CVD (PECVD), that is one of the most useful silicon deposition method, cannot be applied for this process because of its one-directional deposition feature. In addition, the reason for use of disilane instead of monosilane is to reduce process temperature for avoiding silica spheres melting.

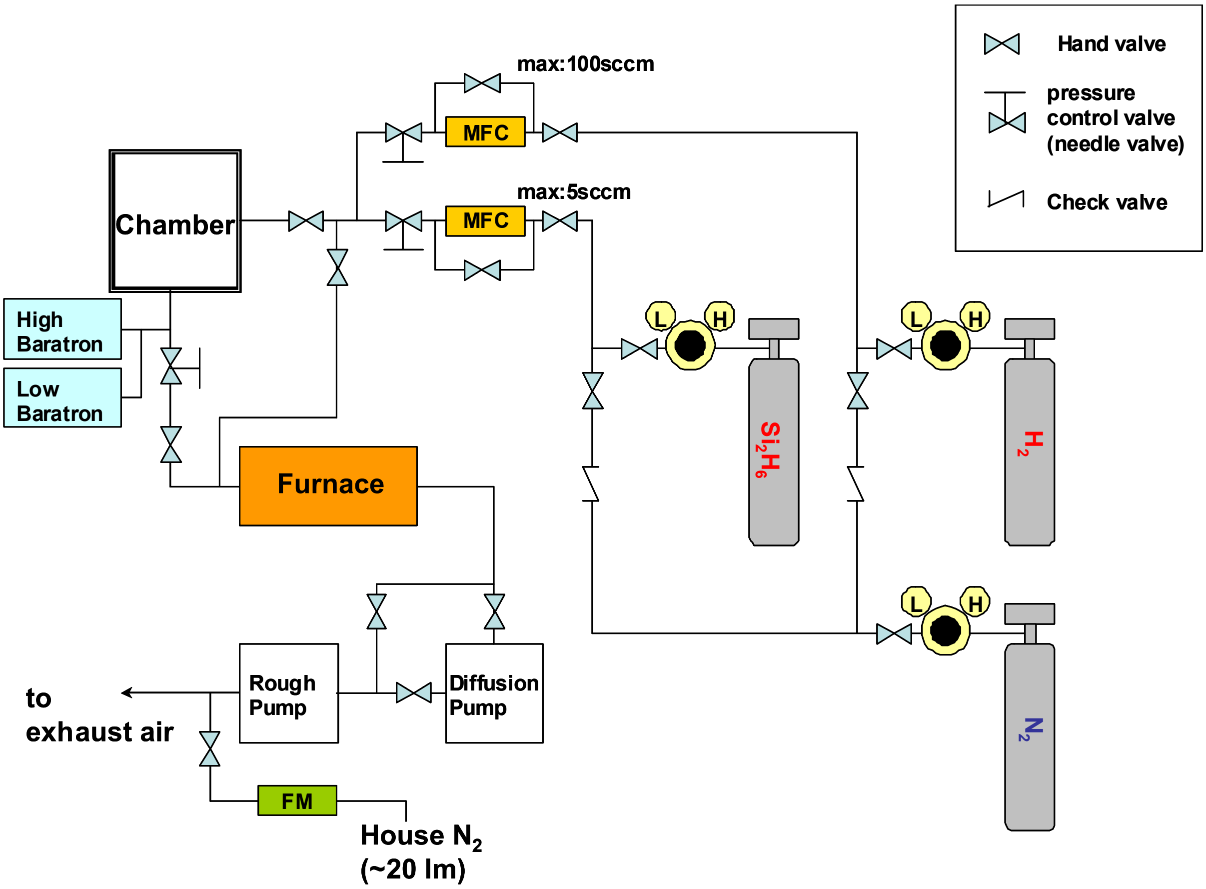

**Figure 2.5a** A schematic diagrams for silicon CVD system in this work.

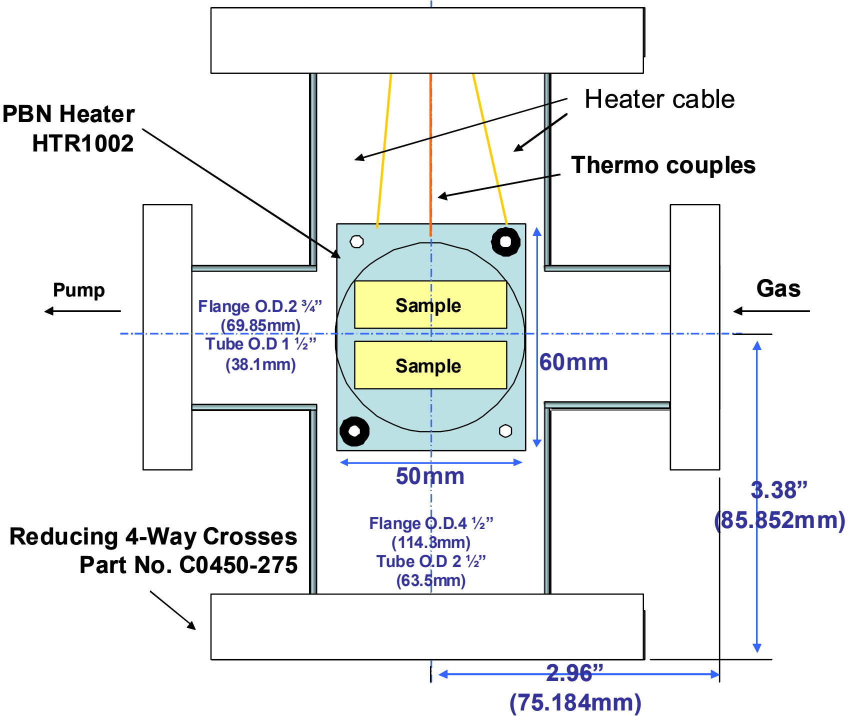

**Figure 2.5b** A schematic diagrams of silicon deposition chamber (top view) for silicon CVD system in this work.

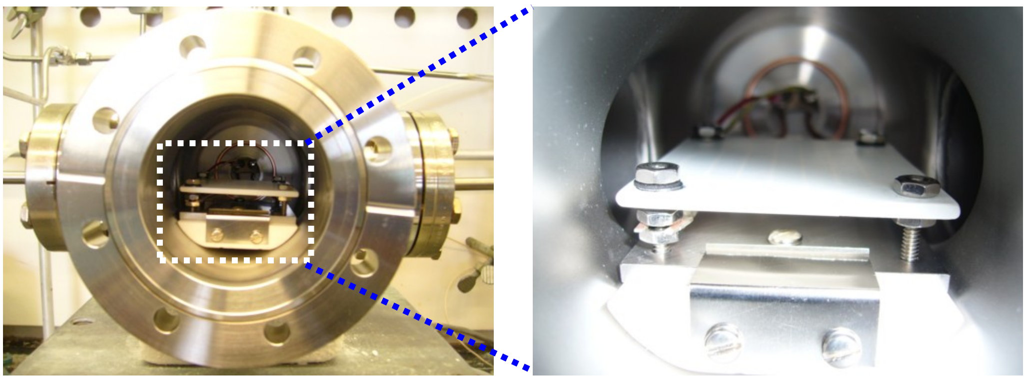

**Figure 2.5c** The front view of the pictures for the inside of silicon deposition chamber. The heater part is insulated from chamber by ceramic board.

Figure 2.5 are schematic diagrams for silicon CVD system and pictures of an actual setup for this work. Substrates are placed on a boron nitride coating carbon heater insulated electrically in a reaction chamber made of stainless steel. The reaction chamber has gas inlet line for source gas which is supplied from a cylinder and its flow rate is precisely controlled by mass flow controller (MFC). The reaction chamber also has another outlet line for gas exhaust and pumping the chamber. A furnace connected to outlet line decomposes the exhausted gas thermally at 800 ˚C to be harmless. The pumping system contains a rotary pump and a diffusion pump to get high vacuum. Moreover it is possible to manipulate the process pressure by not only gas flow rate but also needle valve placed at the outlet line.

A typical silicon CVD condition is listed in Table 2.2. In fact, even thermal CVD that has omni-directional deposition feature, it is inevitable for interstitial voids to remain small vacant part theoretically. [10] In addition, silica opal got some over-layer during silicon infiltration (Figure 2.6), hence the reflectance spectrum showed joint feature of silica-silicon opal and Si layers interference (Figure 2.7).

**Table 2.2** A typical silicon CVD condition

| **heater temperature deg C** | **back pressure torr** | **process pressure torr** | **$Si_2H_6$ flow sccm** | **deposition time hours** |
|---|---|---|---|---|
| 480 | $10^{-4}$ | 2.0 | 0.1 | 2 |

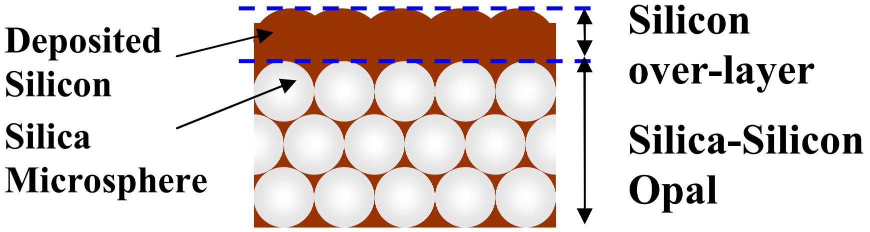

**Figure 2.6** A schematic image of the cross section for silica opal template formed silicon by CVD. Silicon over layer is formed on the top of the silica opal template.

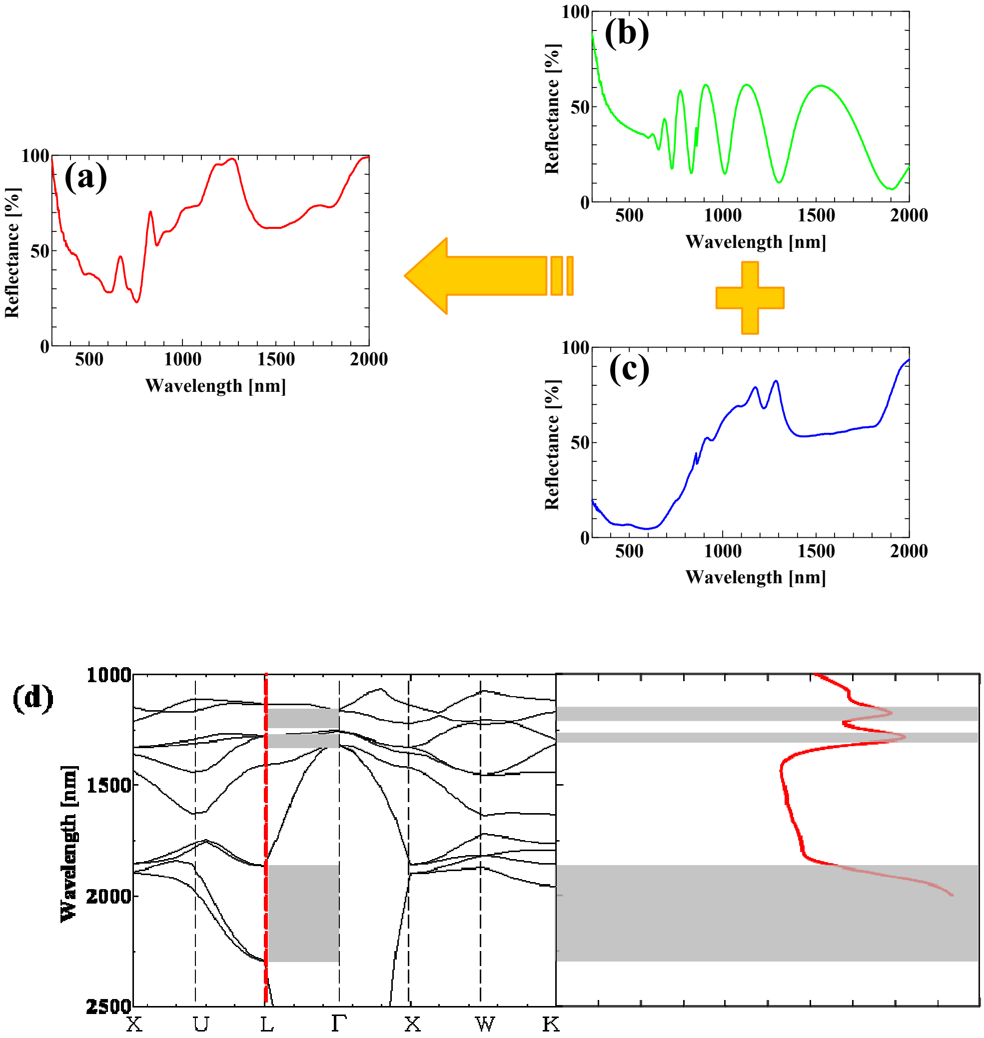

**Figure 2.7** Reflectance spectra for silica-silicon opal with Si over-layer prepared from 600 nm silica microspheres (a), silicon layer prepared at the same time on glass substrate (b) and silica-silicon opal without Si over layer by removing RIE (c). A comparison of optical property of i-cSi-o from theoretical calculation and experimental result. The left side is a photonic band diagram for i-cSi-o fabricated by silica spheres with 600 nm for diameter from theoretical calculation. The right side is a Reflectance spectrum of i-cSi-o obtained from 600 nm spheres.(d)

### 2.2.2.2. Etching and Inversion

It is necessary to remove a silica opal template after silicon infiltration for obtaining an inverse silicon opal. The most common and easiest way to remove silica opal template is a chemical etching by buffered hydrofluoric acid. However, an opal template after silicon infiltration process has a silicon over-layer on top of the film as mentioned last section, and that over-layer prevent buffered hydrofluoric acid reaching the silica opal template. Consequently, we have to remove the over-layer before buffered hydrofluoric acid treatment. Reactive ion etching (RIE) process is very useful for selective one directional silicon etching. In this work, RIE system was utilized. The process condition is in Table 2.3 and that process time is depend on each samples. It is able to know whether the silicon over-layer is enough removed from the observation of samples surface appearance; after over-layer removal, the surface becomes less shine since silica microsphere and interstitial silicon surface is optically scattering; the figure 2.7a explains that with reflectance spectra for examples on this work. The reflectance spectrum after RIE lost Si over-layers interference and that was well matched to theoretical calculation by MIT Photonic-Bands (MPB). (Figure 2.7d)

**Table 2.3** A typical RIE condition

| **temperature** | **back pressure torr** | **process pressure torr** | **RIE RF power W** | **$CHF_3$ flow sccm** | **$O_2$ flow sccm** | **etching time min** |
|---|---|---|---|---|---|---|
| Room temperature | $10^{-6}$ | 0.38 | 200 | 48 | 2 | 10 - 30 |

Since RIE process got the silica opal template surface out, 4 % buffered hydrofluoric acid could etch silica microspheres in a few hours. At the same time, the interface between glass substrate and silica opal template or silicon matrix was also etched and then finally an inverse silicon opal film, which was peeled off from the substrate and a free standing fragile film, was achieved.

The appearance of inverse silicon opal film re-placed on glass substrate, the SEM image and its reflectance spectrum was showed in Figure 2.8. Its SEM image exhibited inverse opal structure but the reflectance spectrum didn’t show expected properties from theoretical calculation (refer to Chapter 3). It might be from two reason, one is the less smooth surface of re-placed inverse silicon opal film that some area should contain air layer at the interface with that substrate disturbing reflectance measurement and the other is a size of probe light of reflectance measurement (about 4 $mm^2$) was much larger than SEM observation scale. In any case, an improvement for optical properties of inverse silicon opal would be one of the most significant issues and solved later (in Chapter 3).

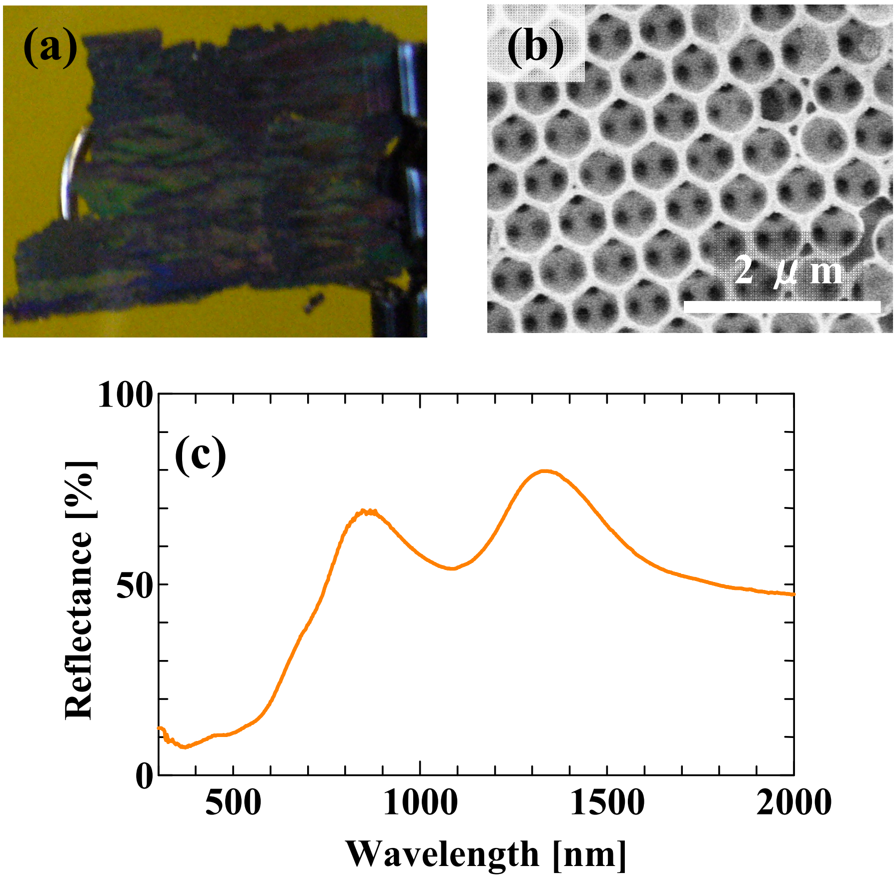

**Figure 2.8** The appearance of inverse silicon opal film re-placed on glass substrate (a), its SEM image (b) and its reflectance spectrum (c).

### 2.2.3. Materials Characterization

#### 2.2.3.1 Scanning Electron Microscopy

A field emission scanning electron microscopy (FE-SEM), Hitachi S-5200, was used for observation of samples microstructures and obtaining images.

#### 2.2.3.2 UV-Vis Spectroscopy

Optical spectra were measured using a Perkin Elmer UV/VIS/NIR spectrometer Lambda 900. Normal transmission mode was used to measure the extinction of the films while the diffuse reflectance and real absorbance spectra were obtained using an integrating sphere detector. For the latter, a highly reflecting plate of $BaSO_4$ was placed at the back of the film so that the probe light passes through the sample twice and only light absorbed by the sample will be absent in the detection process.

#### 2.2.4.3. Raman Spectroscopy

Raman spectra were obtained using JASCO, NRS-1000 with 532 nm He-Ne laser as an excitation for distinct crystallinity of silicon.

### 2.3 Solid Phase Crystallization to Inverse Amorphous Silicon Opals

The as-deposited Si in the interstitial voids of silica opal templates by CVD is amorphous. We denote them as inverse amorphous silicon opals (i-aSi-o). In order to integrate i-Si-o in optical, electro-optical or electrical devices, it is important to achieve inverse crystalline silicon opals (i-cSi-o) because crystalline silicon has a much higher conductivity than amorphous silicon.

Figure 2.9 shows the appearance of a-Si thin film with the same condition of silicon infiltration and c-Si thin film formed from a-Si using the solid phase crystallization (SPC) technique [11] on glass substrate. The a-Si was annealed at 630 ˚C in nitrogen ambient for 5 hours in order to crystallize amorphous silicon. After SPC process, the appearance of a-Si film was obviously changed and it must be recognized from the change of refractive index and the amount of light absorption ratio. Usually crystalline silicon has less refractive index and light absorption ratio than those of amorphous, therefore the change of appearance was reasonable. Not only the observation of appearance change but also the raman spectra showed the broad small peak around 478 cm-1 for a-Si thin film and the narrow peak at 520 cm-1 for c-Si thin film correspond well to the TO phonon modes of each phase, suggesting that the c-Si thin film is well crystallized after SPC. (Figure 2.10).

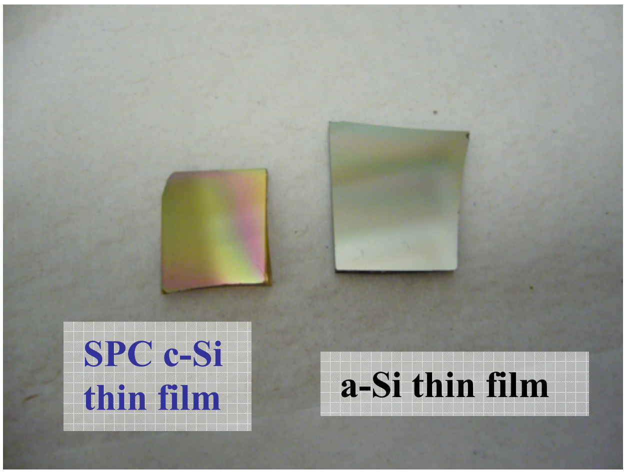

**Figure 2.9** The appearance of a-Si thin film with the same condition of silicon infiltration and c-Si thin film formed from a-Si using the solid phase crystallization (SPC) technique.

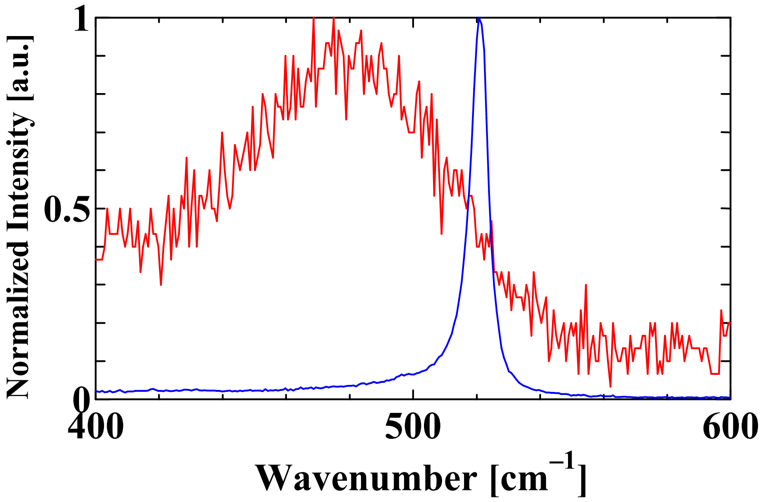

**Figure 2.10** Normalized raman spectra for a-Si thin film (red) and SPC c-Si thin film (blue).

Similarly, the i-aSi-o was annealed at the same condition of the SPC for a-Si film in order to crystallize amorphous silicon and form inverse crystalline silicon opals (i-cSi-o). In addition, Figure 2.11, which shows the SEM image of both i-aSi-o and i-cSi-o by SPC, revealed the i-cSi-o kept its structural order even after suffering SPC process.

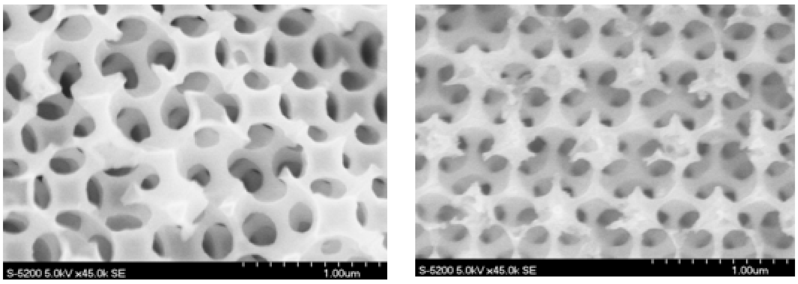

i-cSi-o i-aSi-o

**Figure 2.11** The SEM image of both i-aSi-o and i-cSi-o by SPC

## 2.4 Conclusion

This chapter explained the common process for preparation of inverse silicon opals and a new attempt of this work to obtain inverse crystalline silicon opals. Despite the objective of this work (i-cSi-o) was achieved, it left problems for optical properties of inverse silicon opals and handlings of fragile free standing films.

## 2.5 References

[1] S. John, Phys. Rev. Lett., 58, 2486, 1987.

[2] E. Yablonovitch, Phys. Rev. Lett., 58, 2059, 1987.

[3] K. Busch, S. John, Phys. Rev. E., 1998, 58, 3896.

[4] A. Blanco, E. Chomski, S. Grabtchak, M.Ibisate, S. John, S. W. Leonard, C. Lopez, F. Meseguer, H. Miguez, J. P. Mondia, G. A. Ozin, O. Toader, H. M. van Driel, Nature, 2000, 405, 437.

[5] W. Stöber, A. Fink and E. Bohn, J. Colloid Interface Sci., 1968, 26, 62

[6] P. Jiang, J. F. Bertone, K. S. Hwang and V. L. Colvin, Chem. Mater., 1999, 11, 2132.

[7] S. Wong, V. Kitaev and G. A. Ozin, J. Am. Chem. Soc., 2003, 125, 15589.

[8] V. Kitaev and G. A. Ozin, Adv. Mater., 2003, 15, 75.

[9] E. Hecht, in *OPTICS 4th ed*, (Eds: A. Black), Addison Wesley, San Francisco, CA, USA **2002.**

[10] H. Míguez, N. Tétreault, S.M. Yang, V. Kitaev and G.A. Ozin, *Adv. Mater.,* **2003***, 15,* 597.

[11] Y. Masaki, P. G. LeComber, A. G. Fitzgerald, *J. Appl. Phys.,* **1993***, 74,* 129.

# CHAPTER 3

## Electrical Properties for Inverse Crystalline Silicon Opals

### Abstract

This chapter presents the process for rigid inverse “crystalline” silicon opal (i-cSi-o) film, which is able to stand a process of forming electrodes and keep comparable optical qualities to the i-Si-o film from common process. In addition, the first electrical conductivity measurements of inverse crystalline silicon opals (i-cSi-o) having different lattice constants, ranging from 145 nm to 700 nm, that were fabricated from as-synthesized or pre-sintered silica spheres are presented. The electrical conductivity of i-Si-o is found to be independent of the periodicity of the crystal lattice as well as the inverse opal structural quality. Furthermore, the charge transport is significantly improved by crystallizing and hydrogen plasma passivating the silicon in the inverse opal framework. For the first time, electrical properties that are acceptable for device applications have been achieved in i-Si-o.

### 3.1 Introduction

In spite of enormous research activities of i-Si-o for optical device applications, little effort to utilize i-Si-o for electrical active materials since no one has tried to investigate the electrical properties of i-Si-o. As it was already mentioned in Chapter 2, since the standard process for i-Si-o gives us fragile free-standing film, it made us difficulty to form electrodes on the fragile free-standing film for investigation of any electrical properties. This chapter presents the process for rigid inverse “crystalline” silicon opal (i-cSi-o) film, which is able to stand a process of forming electrodes and keep comparable optical qualities to the i-Si-o film from common process. Moreover the electrical properties of i-Si-o and their correlations to photonic lattice constant are investigated.

## 3.2 Preparation of Rigid and High Quality i-cSi-o

### 3.2.1. i-Si-o on Different Substrates

Instead of a fragile free standing inverse silicon opal film, a rigid film adhered on a substrate is indispensable for the investigation of electrical properties. The requirements for this purpose are resistivity for chemical etching by hydrofluoric acid, high stability for high temperature and high electrical resistivity. A sapphire (aluminum oxide: $Al_2O_3$) substrate satisfies these requirements, which is widely used and commercially available.

A silica opal with 600 nm diameter microspheres was prepared on a smooth surface of sapphire substrate (one side polished substrate) with completely the same procedure as the case of glass substrate. Figure 3.1a shows the comparison of reflectance spectra for silica opals on a glass substrate (black line) and a sapphire substrate (red line) with the spectra of substrates themselves (dashed lines). The reflectance of the sapphire substrate was about 20 % for all measured wavelength because of scattering from unpolished back side surface. The reflectance spectrum of silica opal on a sapphire substrate showed wider and shorter stop band peak and less number of higher bands reflection; that means small peaks from 300 nm to 900nm; than that of a glass substrate; it was a clear proof of less ordered photonic crystal. The insets in Figure 3.1a that are pictures of each silica opals also tell optical qualities of photonic crystal from appearance. It was supposed that the different hydrophilicity on the surface made the meniscus condition change and silica microspheres aggregations; caused defects and disorder in opal structure; must be more probable to occur on a sapphire substrate. Therefore, the process conditions including substrate treatments, concentration of solution and pumping speed were optimized. Table 3.1 shows the comparison of optimized process conditions between on a glass substrate and on a sapphire substrate and it tells less concentration, slower pumping speed and air plasma treatment important for the process on a sapphire. The reflectance spectrum of silica opal fabricated by the optimized condition (light green) compares with the spectrum by former condition (red) in Figure 3.1b. Not only both the stop band and the higher band peaks were clearly observed for optimized condition but also the appearance was similar to silica opal on a glass substrate that had a good opalescence.

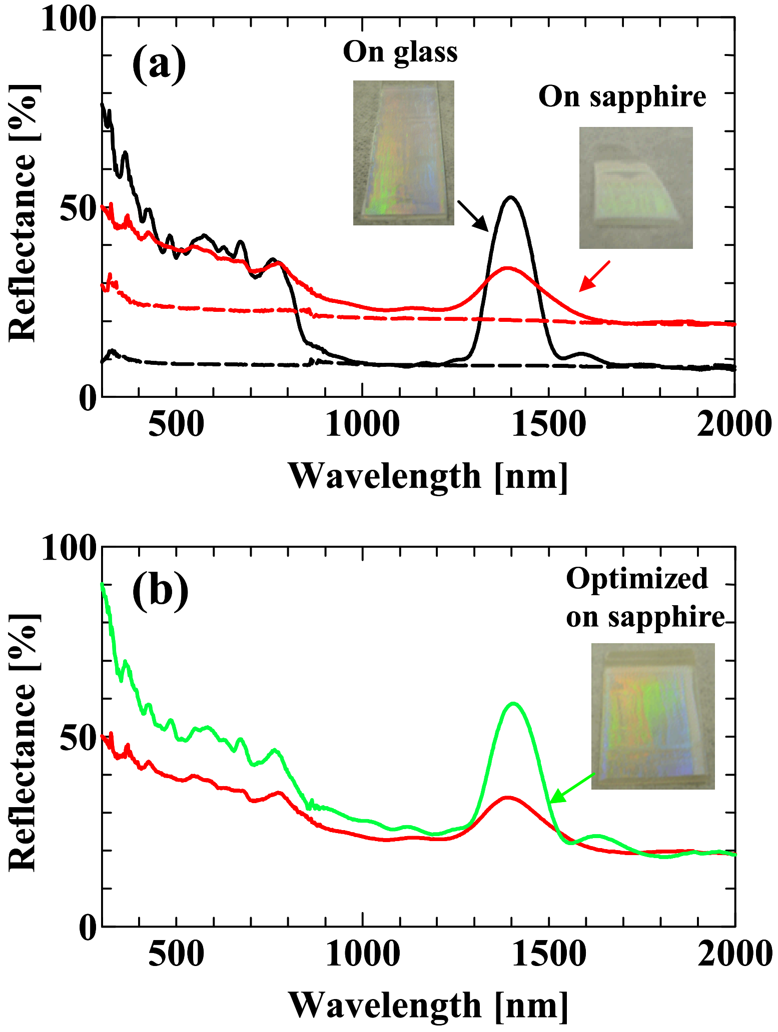

**Figure 3.1** Reflectance spectra for silica opals on a glass substrate (black line) and a sapphire substrate (red line) with the spectra of substrates themselves (dashed lines) (a). The reflectance spectrum of silica opal fabricated by the optimized condition (light green) compares with the spectrum by former condition (red) (b). The insets show pictures of the appearance for each silica opal films.

**Table 3.1** The comparison of optimized EISA conditions between on a glass substrate and on a sapphire substrate

| spher size nm | substrate | process | press torr | soltion vol ml | H2O vol% | sphere wt % | sonication hours |
|---|---|---|---|---|---|---|---|
| 300 | glass | a | atmospheric | 8 | 5 | 2.55 | 5 |
| 390 | glass | a | atmospheric | 8 | 5 | 2.77 | 5 |
| 470 | glass | b | 40 | 8 | 5 | 3.79 | 5 |
| 600 | glass | b | 45 | 8 | 5 | 2.54 | 8 |
| 145 | **sapphire** | a | atmospheric | 8 | 5 | **1.21** | 5 |
| 300 | **sapphire** | a | atmospheric | 8 | 5 | **1.02** | 5 |
| 470 | **sapphire** | b | **90** | 8 | 5 | **1.11** | 5 |
| 560 | **sapphire** | b | **100** | 8 | 5 | **1.33** | 8 |
| 600 | **sapphire** | b | **110** | 8 | 5 | **1.52** | 8 |
| 700 | **sapphire** | b | **120** | 8 | 5 | **0.95** | 8 |

It was possible to prepare inverse crystalline silicon opals on sapphire substrate with the same procedure and condition as on glass substrates after obtaining good silica opal templates. Figure 3.2a shows the reflectance spectra of silica opal self-assembled using 520 nm (pre-sintered spheres; refer in 3.2.2) diameter spheres and the corresponding inverse silicon opals i-aSi-o and i-cSi-o. The scanning electron microscopy (SEM) image of i-cSi-o can be seen in the inset of Figure 3.2a. The reflectance spectrum of silica opal template shows the stop-band reflection at 1190 nm with well defined peaks from higher energy bands and small reflections from Fabry-Pèrot interference,[1] evidence of a highly ordered opal lattice. The i-aSi-o has the stop-band reflection and distinctive two higher bands ("second band" and "third band") reflections at 1863 nm, 1145 nm and 1011 nm, respectively. The i-cSi-o also shows the stop-band reflection, the second band reflection and the third band reflection, although the positions are blue-shifted from those of i-aSi-o, consistent with the difference of refractive index between amorphous Si ($n \approx 4.0$) and crystalline Si ($n \approx 3.45$).[2] It should be noted that the position of the third band corresponds to the energy of the full photonic bandgap according to theoretical calculations, [3] and its existence implies that both i-aSi-o and i-cSi-o have retained the good structural order of the silica opal. The inset in the SEM image further supports the high structural quality of i-cSi-o. Figures 3.2b and 3.2c show the reflectance spectra of samples templated with silica opals having 420 nm (pre-sintered) and 275 nm (pre-sintered) diameter spheres, respectively. With decreasing sphere size, all of the photonic properties as expected were blue shifted. It is noteworthy that reflections from the higher bands were still distinguishable, indicating the high structural quality of all the i-cSi-o samples. For comparison, Figure 3.2d shows the reflectance spectra of the sapphire substrate, a-Si thin film and c-Si thin film fabricated with exactly the same deposition and crystallization conditions as used for i-Si-o. The spectra of a-Si and c-Si thin films show Fabry-Pèrot interference fringes of different magnitude, which manifest the differences in the absorption coefficients and refractive indices between the two phases of Si.

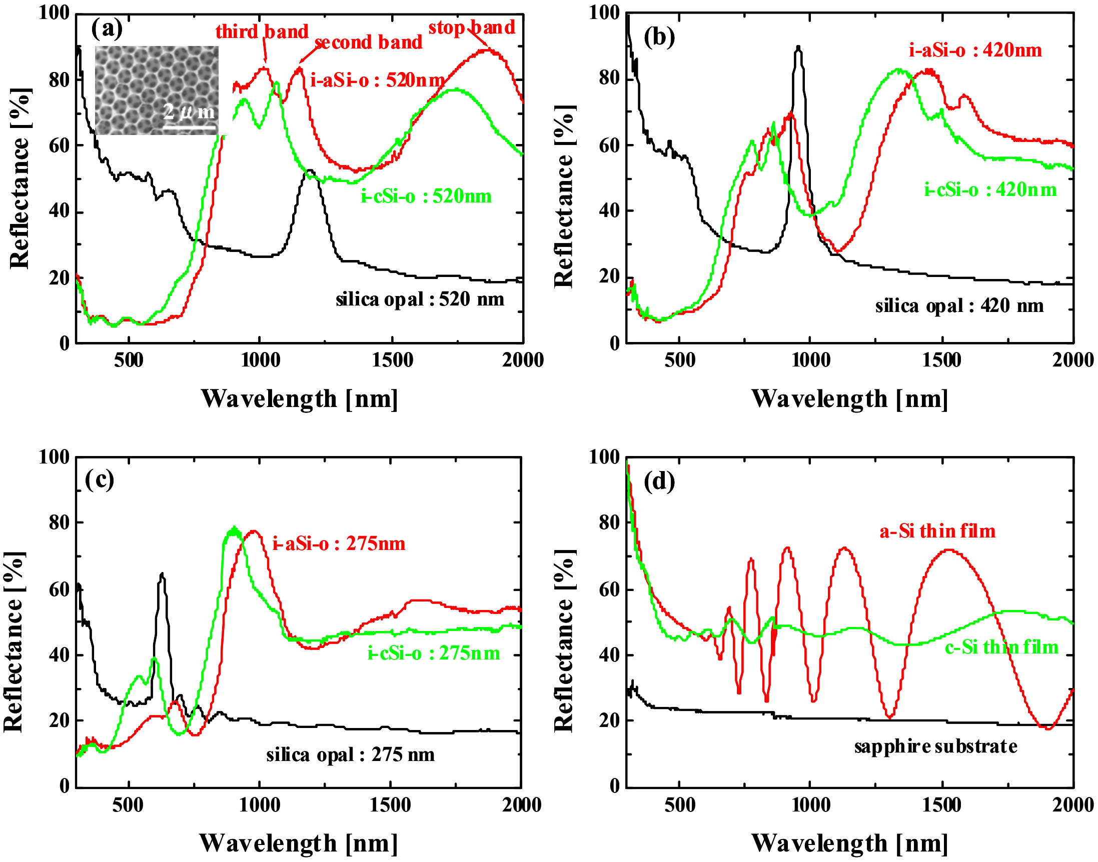

**Figure 3.2** Reflectance spectra of silica opal, inverse amorphous silicon opal (i-aSi-o) and inverse crystalline silicon opal (i-cSi-o) depicted as black, gray and light gray respectively for sphere sizes 520 nm (a), 420 nm (b) and 275 nm (c). The inset in (a) shows a SEM image of the i-cSi-o (scale bar is 2 μm). The position of the stop band and the first and the second higher energy bands of i-aSi-o are indicated by the arrows in (a). Reflectance spectra of the sapphire substrate, a-Si and c-Si thin film are shown in (d) for comparison.

### 3.2.2. Pre-sintering of Silica Microspheres

Cracking in the silica opal during photonic crystallization is very hard to prevent. The initial crystal consists of silica microspheres separated by nanometer thick hydration layer, and this layer subsequently evaporates and causes cracking through lattice contraction. It is almost impossible to eliminate such cracking completely, however it's possible to reduce this by optimization of process condition. Assuming such a well ordered, relatively crack-free silica opal can be obtained, subsequently that silica opal should be suffered high temperature process for silicon infiltration to achieve i-Si-o. Such process can cause serious cracking.

One solution is to perform the silica microsphere pre-sintering process. The pre-sintering process has been reported to reduce the cracking of i-Si-o film arising from thermal shrinkage of the spheres during the Si infiltration process.[4] In the pre-sintering process, silica microspheres were annealed at higher temperature than that of silicon infiltration process (in this work, 650 ˚C annealing at air ambient for 5 hours) before silica opal formation. Those annealed spheres were aggregated and sticking each other strongly, therefore re-dispersion of spheres by sonication was the key process for pre-sintering. Figure 3.3 shows comparison of reflectance spectrum for silica opal prepared from 600 nm spheres and that from pre-sintered 600 nm spheres. The reflectance spectrum from pre-sintered spheres (red) was observed blue sift, which told us silica microspheres shrunk to 550 nm by theoretical calculation (formula (1.3) and (1.4)), and showed the worse photonic crystallinity. It must be from insufficient re-dispersion, and sonication for re-dispersion of silica microspheres in water instead of ethanol, that was commonly used, made silica opal quality better (light green), see in Figure 3.3. In addition, silica opal film prepared from more concentrated solution (blue) showed sharper and higher peak at the stop band.

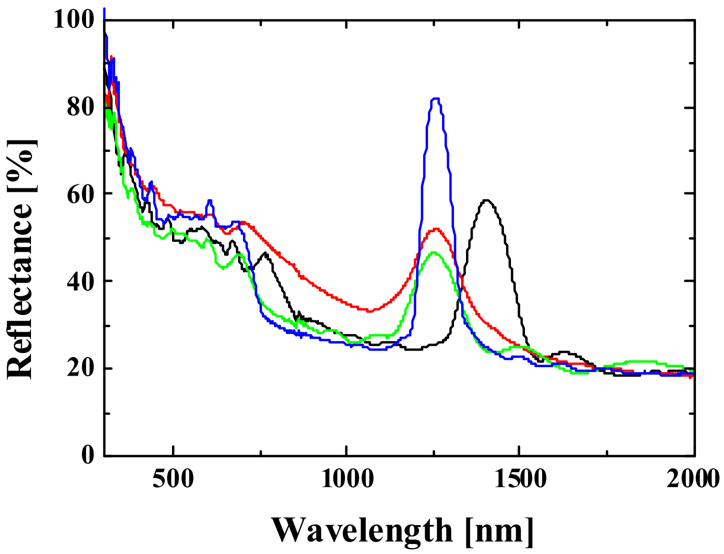

**Figure 3.3** Reflectance spectra for silica opal on sapphire substrate from 600 nm spheres (black), pre-sintered 600 nm spheres with same EISA process (red), water re-dispersion pre-sintered 600 nm spheres (light green) and that of more concentrated solution (blue)

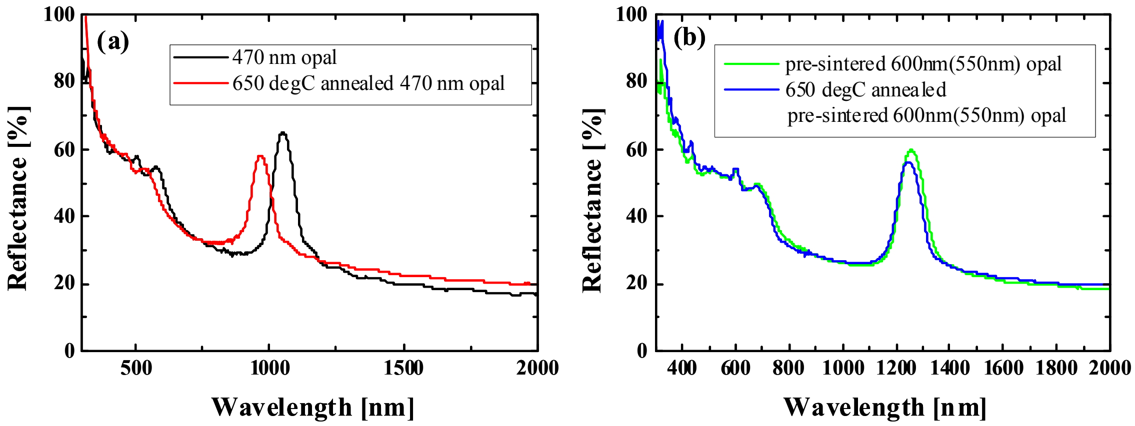

**Figure 3.4** The comparison of reflectance spectra for silica opals on sapphire substrate from 470 nm spheres before (black) and after (red) annealing at 650 ˚C in air ambient for 5 hours.(a) The reflectance spectra for silica opals from pre-sintered 600 nm spheres before (light green) and after (blue) annealing with the same condition.(b)

Moreover, each silica opal films formed from as synthesized 470 nm silica microspheres and pre-sintered 600 nm silica microspheres; those were actually shrunk to 550 nm; were annealed at 650 ˚C at air ambient for 5 hours to observe effects of pre-sintering process. The reflectance spectrum of the former silica opal showed blue sift, wider and shorter stop band peak and disappearance of some higher bands peaks after annealing, see in Figure 3.4a. On the contrary, the latter silica opal showed little change of its reflectance spectrum before and after annealing (see in Figure 3.4b); that was the clear proof for the effect of pre-sintering to prevent cracks in silica opals during high temperature process.

Figure 3.5 is a comparison of the microscope images of the surface of i-cSi-o made with as-synthesized microspheres (a) and with pre-sintered microspheres (b). The pre-sintering leads to much larger domains of i-cSi-o than that without pre-sintering. However both non-sintered and pe-sintered samples display roughly same width of stress induced cracks.

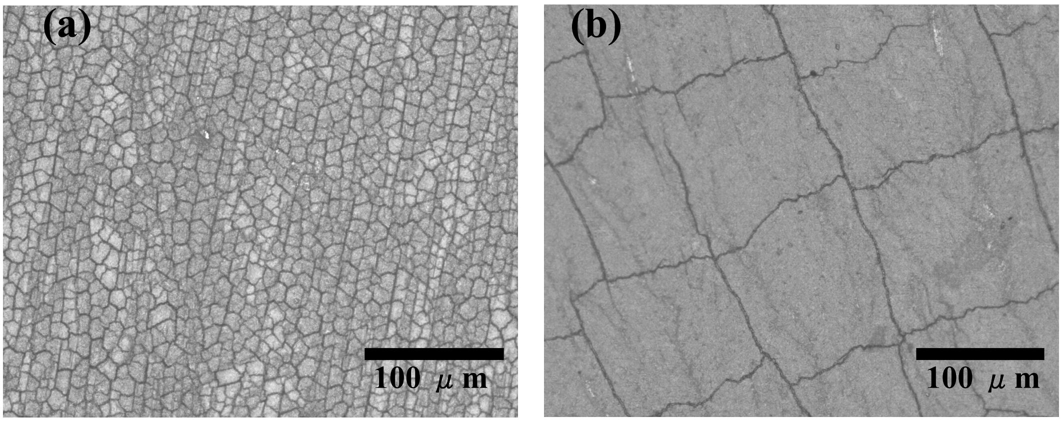

**Figure 3.5** A comparison of the microscope image of the surface on i-cSi-o made from without pre-sintered spheres (a) and with pre-sintered spheres (b). The pre-sintering made much larger domains of i-cSi-o than that of without pre-sintering. However both of them have roughly same width of cracks.

## 3.3 Electrical Properties for i-cSi-o

### 3.3.1. Two Probe Method

To measure the dc electrical dark conductivity ($\sigma_d$), two probe method was in practice, in which the current was recorded while the bias across the electrode pair was increased from -20 V to +20 V in increments of 5 V (Figure 3.6). Aluminum co-planar electrodes with a separation of 1 mm were evaporated on the surface of the samples by a physical vapor deposition apparatus (Varian/NRC, NRC3117). It should be noted that the aluminum film infiltrated negligibly into the i-cSi-o film but localized instead on the of top of i-cSi-o film. The $\sigma_d$ was determined from the resulting I-V curves, which linearity was implying a good ohmic contact between the aluminum and the i-Si-o, with the equation $\sigma_d = Il/VS$, where $l$ is the gap length between two electrodes and $S$ is the cross sectional area of the films. The area includes not only the Si framework but also the void spaces.

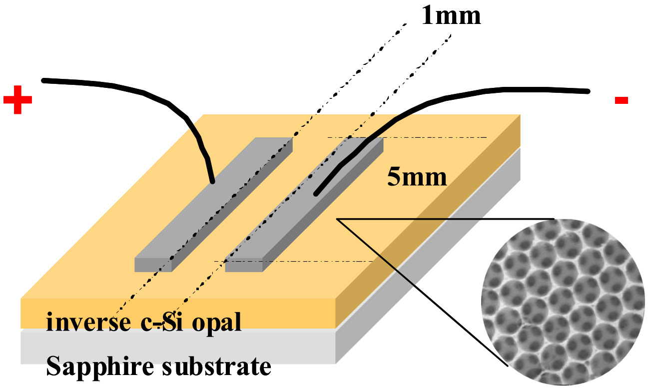

**Figure 3.6** A schematic diagram of two probe method for i-cSi-o

### 3.3.2. Size and Defects Dependence of Electrical Properties for i-cSi-o

Figure 3.7 shows the dc electrical dark conductivity of i-cSi-o made from different sphere sizes and that of a-Si and c-Si thin films for comparison. In addition, we investigated the effect of film cracking on i-cSi-o which can create critical defects for electrical conductance, by using pre-sintered silica microsphere opal templates. However, our results show that the pre-sintering had little effects on $\sigma_d$ of i-cSi-o. Considering that the density of cracks was ~10 times lower for i-cSi-o made from pre-sintered spheres than without pre-sintering (see Figure 3.5), it may be postulated that the cracks are at least partially infiltrated by Si such that conductivity is not hindered by the physical gaps. Therefore the cracks cannot be critical obstacles for electrical carrier transportation. Initially we also hypothesized some dependence of $\sigma_d$ on template sphere size as the thickness of the Si framework in i-cSi-o that provides the actual electrical paths decrease with reducing template sphere size. Figure 3.7

shows that this is not the case in practice: neither a clear dependence of the sphere size nor a pre-sintering effect is observed.

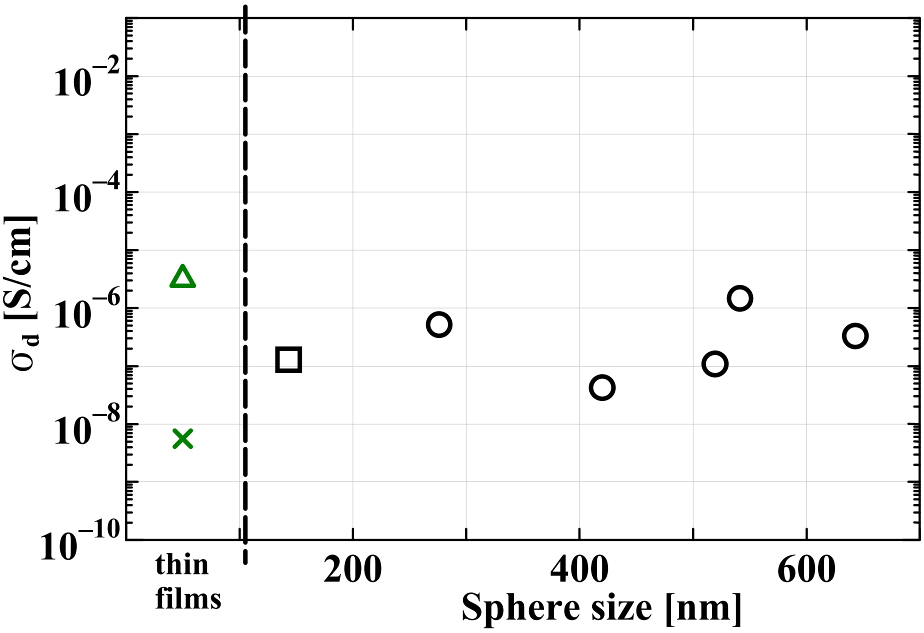

**Figure 3.7** A plot of $\sigma_d$ with respect to template sphere size for i-cSi-o obtained from as-synthesized sphere (open square) or pre-sintered sphere (open circle). The data for a-Si thin film (cross) and c-Si thin film (open triangle) are shown on the left for comparison.

### 3.3.3. Effect of Hydrogen Plasma Passivation

The hydrogen plasma passivation (HPP) is a well known technique to reduce the density of Si dangling bonds that serve as electronic trap states. [5] The solid phase crystallized (SPC) silicon thin films especially contain enormous amount of such trap states that must be a serious difficulty for electrical device applications. Therefore, the effect of HPP must be investigated to improve electrical properties of i-cSi-o.

Hydrogen plasma passivation was carried out in a dc saddle-field plasma enhanced CVD apparatus, with the substrate remote from the plasma, at a hydrogen pressure of 0.8 torr dc power of 0.1 W/cm$^2$, and substrate temperature of 300 °C.

Figure 3.8a shows the Raman spectrum of a-Si and c-Si thin films on sapphire substrate. The broad peak around 478 cm$^{-1}$ for a-Si thin film and the narrow peak at 520 cm$^{-1}$ for c-Si thin film correspond well to the TO phonon modes of each phase. The proportion of the crystalline to amorphous phase in c-Si is about 96%, as calculated from the relative intensity of the two peaks. [6-8] The average grain size of the c-Si estimated from the peak shift of TO phonon mode from that of single crystalline Si is about 10 nm, suggesting that the c-Si thin film is well crystallized after SPC. Under the same SPC conditions, i-cSi-o shows both the amorphous and crystalline Si peaks at 478 cm$^{-1}$ and at 512 cm$^{-1}$ (Fig. 3.8b). The crystalline fraction and average grain size of i-cSi-o are about 50% and 2 nm respectively, notably lower than the c-Si thin film. We believe this difference may have arisen from the low thermal conductivity and open silicon framework of i-Si-o. However, upon HPP, the crystallinity and average grain size of i-cSi-o increased significantly to 92% and 8 nm, respectively, as estimated from the sharp Raman peak at 518 cm$^{-1}$. This observation is consistent with previous reports that showed hydrogen plasma can crystallize amorphous Si even at 150°C.[9] By contrast, there is no change in the crystallinity of c-Si thin film after HPP (Fig. 3.8a) as almost all of the Si had already crystallized after SPC.

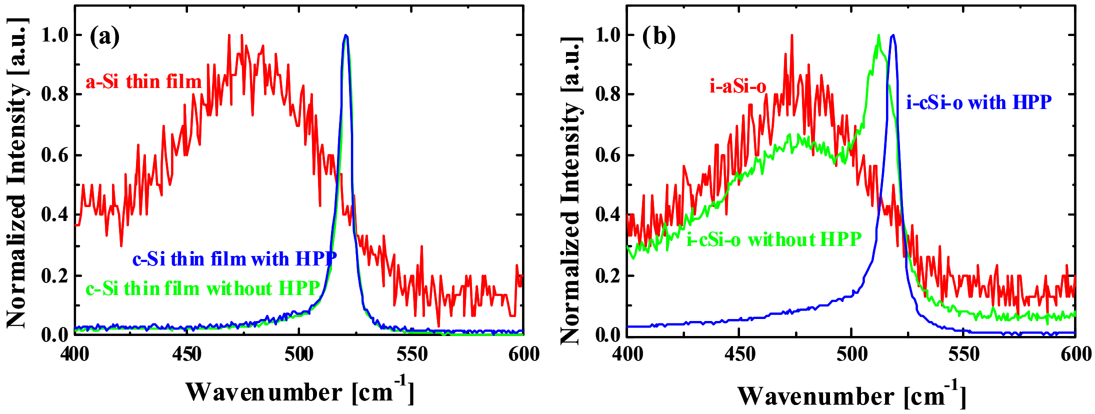

**Figure 3.8** A comparison of the Raman spectra of Si thin films (a) and i-Si-o (b) after each step: as-deposited amorphous Si (red), crystalline Si after SPC (light green) and crystalline Si after HPP (blue). Each spectrum is normalized with respect to the maximum intensity.

Figure 3.9 shows the dc electrical dark conductivity of i-cSi-o made from different sphere sizes with or without HPP and those of a-Si and c-Si thin films for comparison. The results

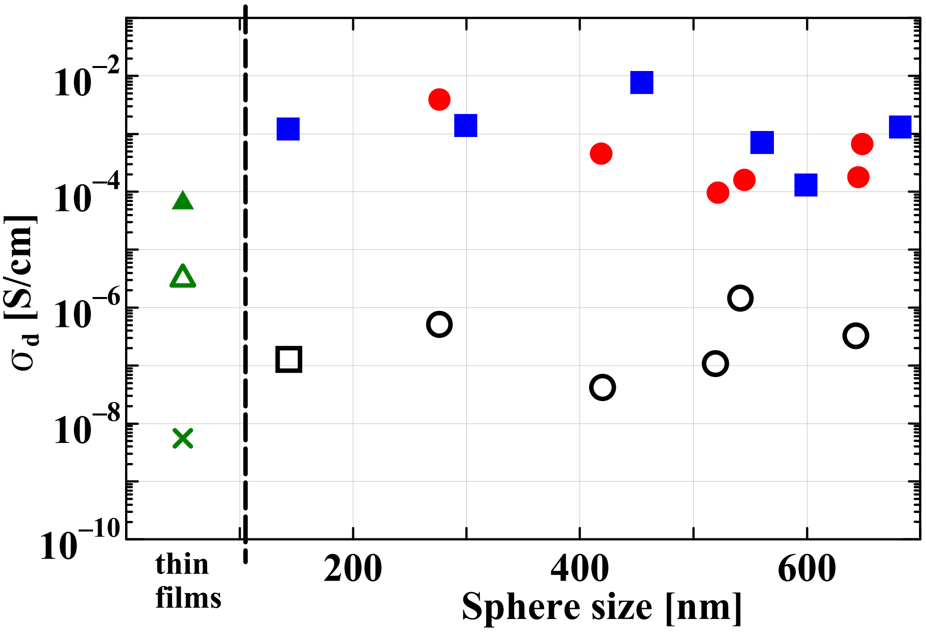

**Figure 3.9** A plot of $\sigma_d$ with respect to template sphere size for i-cSi-o with HPP (solid) or without HPP (open) obtained from as-synthesized sphere (square) or pre-sintered sphere (circle). The data for a-Si thin film (cross) and c-Si thin film (triangle) are shown on the left for comparison.

clearly demonstrate that HPP increases $\sigma_d$ of i-cSi-o by 2 to 4 orders of magnitude suggesting that for the sphere size range employed in this study, the dominant factors influencing $\sigma_d$ are the fraction of Si in i-cSi-o, which is comparable for all samples, and the population of Si dangling bonds rather than the thickness of Si framework in i-cSi-o. On the other hand, the effect of HPP on $\sigma_d$ for c-Si thin film is much smaller, with an increase of ~20 times. The rate of increase however is in the expected range of previous reports on polycrystalline Si. [10] Our result demonstrates that HPP increases the conductivity of i-cSi-o to a much greater extent than it does for the c-Si thin film. It is interesting to note that, for the case at hand, the electrical conductivity of i-cSi-o is slightly greater than of the c-Si thin film after HPP. The dramatic change in $\sigma_d$ for i-cSi-o after HPP is prominently due to the increase in crystallization from 50% to 92% by hydrogen plasma, as detected by Raman spectroscopy (Fig. 3.8b). However, the fact that the electrical conductivity of i-cSi-o exceeds that of the c-Si thin film after HPP even though its crystalline fraction is still lower (92% as compared to

98%) suggests that the HPP process is more effective for passivating Si dangling bonds within the grain boundaries and at the surfaces of the i-cSi-o structure as compared to the c-Si thin film. This result is reasonable considering the increased exposure of the open i-cSi-o structure to the hydrogen radicals during HPP as compared to its thin film counterpart. In addition, the direction of crystallization in the c-Si thin film may be different than that of i-Si-o and thereby influencing the orientation of grain boundaries that give rise to potential barriers in the conductivity measurement.

### 3.3.4. Temperature Dependence

In order to understand the quality of these Si samples as semiconductors, the temperature dependence of $\sigma_d$ were studied. Low temperature conductivity measurements were performed with a liquid nitrogen variable temperature cryostat (Janis Research Co., VPF-700) and the activation energy ($E_a$) was determined from a plot of $\sigma_d$ measured as function of reciprocal temperature using the same electrode configuration under a bias of 20 V.

Figure 3.10 shows the $\sigma_d$ of i-cSi-o and c-Si thin film with or without HPP as a function of reciprocal temperature. Without HPP, both i-cSi-o (open circle) and c-Si thin film (open triangle) show two conductivity regimes. Above 220 K, $\sigma_d$ shows activated behavior [11] with an activation energy of 0.479 eV for i-cSi-o and 0.538 eV for c-Si thin film. Below 220 K, a $T^{-1/4}$ behavior is observed, indicating variable range hopping conductivity, also known as Mott conductivity.[11] On the contrary, with HPP both i-cSi-o (solid circle) and c-Si thin film (solid triangle) show only activated behavior over the entire temperature range (130 K to 300 K). Moreover, the activation energy of HPP samples decreased from 0.479 eV to 0.310 eV for i-cSi-o and from 0.538 eV to 0.288 eV for c-Si thin film. The elimination of variable range hopping and the reduction of the activation energy by HPP are most likely due to a decrease in the grain-boundary potential barriers originating from the Si dangling bonds.[11] In addition, no saturated behavior is observed in the entire temperature range regardless of HPP, suggesting that the crystalline Si is relatively intrinsic or may contain deep dopant levels if there exist some donor- or acceptor-like impurities.[12] The overall $\sigma_d$ of i-cSi-o after HPP and its linear logarithmic temperature dependence suggest promising opportunities for their use as intrinsic semiconductors, which are often used as the conversion layer of thin film Si solar cells that require $\sigma_d$ in the range from $10^{-5}$ to $10^{-3}$ S/cm.[13]

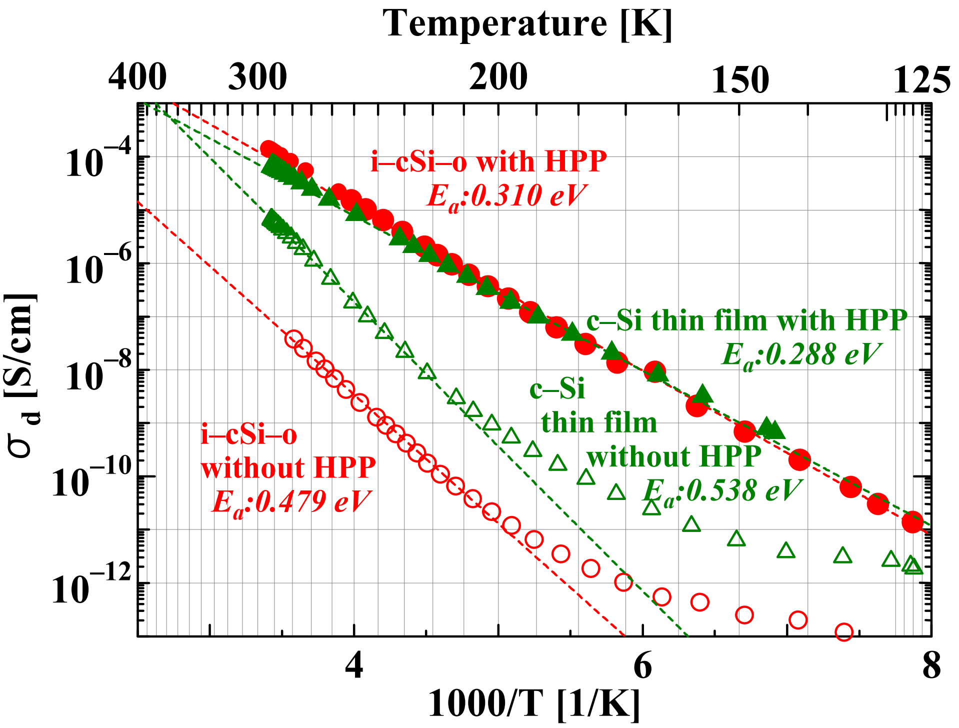

**Figure 3.10** Temperature dependence of $\sigma_d$ for c-Si thin films (triangles) and i-cSi-o (circles) with or without HPP (solid or open symbols, respectively). The data for c-Si thin film and i-cSi-o without HPP were fitted with exponential curves $\sigma_d = \sigma_0 \exp(-E_a/k_B T)$ for $T > 220$K, to obtain the activation energies 0.538eV and 0.479eV, respectively. The logarithm of σd for c-Si thin film and i-cSi-o with HPP are linear throughout the entire temperature range and yield activation energies of 0.288eV and 0.310eV, respectively.

## 3.4 Conclusions

In Summary, we have measured the electrical conductivity of inverse crystalline silicon opals (i-cSi-o) having different lattice constants, ranging from 145 nm to 700 nm, that were fabricated from as-synthesized or pre-sintered silica spheres. The electrical conductivity of i-Si-o is found to be independent of the periodicity of the crystal lattice as well as the inverse opal structural quality. Furthermore, the charge transport is significantly improved by crystallizing and hydrogen plasma passivating the silicon in the inverse opal framework. For the first time, electrical properties that are acceptable for device applications have been achieved in inverse silicon opal, paving the way to uniquely integrate the omni-directional photonic bandgap of i-cSi-o with the semiconductivity of silicon for the express purpose of enhancing the photon to electron conversion efficiency of silicon solar cells.

## 3.5 References

[1] E. Hecht, in *OPTICS 4th ed*, (Eds: A. Black), Addison Wesley, San Francisco, CA, USA **2002.**

[2] A. Toneva, T. Mihailova, P. Danesh, B. Pantchev, *Semicond. Sci. Technol.,* **1994***, 9,* 2285.

[3] K. Busch, S. John, *Phys. Rev. E.,* **1998***, 58,* 3896.

[4] A. A. Chabanov, Y. Jun, D. J. Norris, *Appl. Phys. Lett.,* **2004***, 84,* 357.

[5] V.M. Arole, R.O. Dusane, M.G. Takwale, B.R. Marathe, V.G. Bhide, *Solar Energy Mater.*, **1988**, *17*, 391.

[6] H. Richter, Z. P. Wang, L. Ley, *Solid State Commun.,* **1981***, 39,* 625.

[7] I. H. Campbell, P. M. Fauchet, *Solid State Commun.,* **1986***, 58,* 739.

[8] W. Weia, G. Xub, J. Wangc, T. Wang, *Vacuum,* **2007***, 81,* 656.

[9] D. Das, *Solid State Commun.*, **1998**, *108*, 983.

[10] V.M. Arole, R.O. Dusane, M.G. Takwale, B.R. Marathe, V.G. Bhide, *Solar Energy Mater.*, **1988**, *17*, 391.

[11] N. H. Nickel, in *Hydrogen in semiconductors II (semiconductors & semimetals vol 61)*, (Eds: R. K. Willardson, E. R. Weber), ACADEMIC PRESS, San Diego, CA, USA **1999.**

[12] J. M. Dusseau, J. L. Robert, *Journal of the Less-Common Metals*, **1981**, *82*, 137.

[13] J. Meier, S. Dubail, J. Cuperus, U. Kroll, R. Platz, P. Torres, J.A. Anna Selvan, P. Pernet, N. Beck, N. P. Vaucher, Ch. Hof, D. Fischer, H. Keppner, A. Shah, *J. Non-Crystal. Solids*, **1998**, *227–230*, 1250.

# CHAPTER 4

# Impurity Doping and Conductivity Control for i-cSi-o

## Abstract

While the silicon photonic crystals have promised revolutionary developments in the field of optical telecommunications and optical computing, it has only recently been realized that their prowess to trap and slow photons could potentially significantly improve the efficiency of silicon solar cells. In this chapter n-doped and p-doped inverse silicon opals are synthesized and processed to optimize their electrical charge transport properties, which are shown to be of semiconductor device quality.

## 4.1 Introduction

The previous chapter showed that the inverse crystalline Si opal (i-cSi-o) with its three-dimensional open-framework microstructure has comparable conductivity as intrinsic crystalline Si (c-Si) in spite of its high porosity. Hydrogen plasma passivation further enhances the conductivity to an acceptable level for the potential integration into an optically amplified silicon solar cell.[1,2] However, such an optoelectronic semiconductor device with i-cSi-o as a key component demands further exploration of the p-type or n-type doped structures, which are still unknown. Basically, one of the most important properties for a semiconductor is the controllability of its conductivity with the carrier type being either electrons or holes. The semiconductors with electrons as majority carriers are called n-type (negatively charged type) semiconductors while those with holes are p-type (positively charged type) semiconductors; either case usually has much higher conductivity than the intrinsic semiconductor. The properties of intrinsic, p-type and n-type semiconductors enable us to create many devices like pn-diode, MOS-transistor, TFT and solar cells. Therefore we decided to carry out an investigation to understand the electrical properties of p-type and n-type doped i-Si-o, focusing on the fabrication of the first-reported boron doped p-type and phosphorus doped n-type i-cSi-o photonic crystals and the effect of hydrogen plasma passivation on their electrical conductivities. We also prepared doped and non-doped c-Si thin films which were fabricated by the same procedures as i-cSi-o except without opal processing for comparison because the electrical properties of c-Si thin films are well known and exhibit typical semiconductor behavior.

## 4.2 Experimental Methods

### 4.2.1. PN Doping with Sol-Gel Precursors

To realize our objectives, we chose silica opals with 460 nm sphere diameter for templates on sapphire substrates because Chapter 3 showed little dependence of $\sigma_d$ on the photonic crystal lattice constant of i-Si-o. As it was already mentioned, the as-deposited Si in the interstitial voids of silica opals by CVD is intrinsically amorphous. To incorporate dopants into the i-cSi-o framework, we prepared sol-gel solutions containing boron or phosphorus precursors as dopant diffuser (Tokyo Ohka Kogyo, EPLUS SC-1006 or EPLUS SC-913) and spin-coated them on i-aSi-o. Subsequently the coated samples were annealed at 630˚C in nitrogen ambient for 24 hours in order to crystallize amorphous silicon using the solid phase crystallization (SPC) technique [3] and to facilitate the diffusion of boron or phosphorus atoms into the Si semiconductor crystal lattice in i-cSi-o. Undoped i-cSi-o was prepared as well to serve as a control. The doped i-cSi-o was then treated with HF to remove a thin oxidized $SiO_2$ layer resulting from the dopant precursor, and then the films underwent hydrogen plasma passivation (HPP) to reduce the density of Si dangling bonds that otherwise serve as electronic trap states. [4]

### 4.2.2. Energy Dispersive X-ray Spectroscopy (EDX)

Energy-dispersive X-ray spectroscopy (EDX) is an analytical technique used for the elemental analysis or chemical characterization of a sample. It is one of the variants of X-ray fluorescence spectroscopy which relies on the investigation of a sample through interactions between electromagnetic radiation and matter, analyzing X-rays emitted by the matter in response to being hit with charged particles. To stimulate the emission of characteristic X-rays from a specimen, a high-energy beam of charged particles such as electrons, is focused into the sample being studied. An atom within the sample contains ground state (or unexcited) electrons in discrete energy levels or electron shells bound to the nucleus. The incident beam may excite an electron in an inner shell, ejecting it from the shell while creating an electron hole where the electron was. An electron from an outer, higher-energy shell then fills the hole, and the difference in energy between the higher-energy shell and the lower energy shell may be released in the form of an X-ray. The number and energy of the X-rays emitted from a specimen can be measured by an energy-dispersive spectrometer. As the energy of the X-rays are characteristic of the difference in energy between the two shells, and of the atomic structure of the element from which they are emitted, this allows the elemental composition of the specimen to be measured.

### 4.2.3. Wavelength Dispersive X-ray Spectroscopy (WDX)

The Wavelength dispersive X-ray spectroscopy (WDX) is a method used to count the number of X-rays of a specific wavelength diffracted by a sample. The wavelength of the impinging x-ray and the sample’s crystal lattice spacings are related by Bragg's law and produce constructive interference if they fit the criteria of Bragg's law. Unlike the related technique of EDX, WDS reads or counts only the x-rays of a single wavelength, not producing a broad spectrum of wavelengths or energies. This generally means that the element must be known to find a crystal capable of diffracting it properly with roughly 10 to 100 times higher sensitivity than EDX. The technique is often used in conjunction with EDX, where the general chemical make-up of an unknown can be learned from its entire spectrum. WDX is mainly used in chemical analysis, in an X-ray fluorescence spectrometer, or in an electron microprobe. It is usually operated under vacuum to reduce the absorption of soft radiation (low-energy photons) by the air and thus increase the sensitivity for the detection and quantification of light elements (between boron and oxygen).

## 4.3 Characterization of Intentionally Doped i-cSi-o

### 4.3.1. Optical Properties of PN Doped i-cSi-o

Figure 4.1a shows the reflectance spectra of silica opal self-assembled using 460 nm diameter spheres and the corresponding inverse silicon opals i-cSi-o. The reflectance spectrum of silica opal template shows the stop-band reflection at 1036 nm with well defined peaks from higher energy bands and small reflections from Fabry-Pèrot interference, [5] evidence of a highly ordered opal lattice. The i-cSi-o has the stop-band reflection and two distinctive higher bands (“second band” and “third band”) reflections at 1349 nm, 884 nm and 804 nm, respectively. It should be noted that the position of the third band corresponds to the energy of the complete photonic bandgap according to theoretical calculations, [6] and its existence implies that i-cSi-o has retained the good structural order of the silica opal. Figures 4.1b, 4.1c and 4.1d show the reflectance spectra of boron-doped, phosphorus-doped samples and that of SEM image, respectively; Figures 4.1b and 4.1c both exhibit the aforementioned distinctive three bands (stop-, second- and third-band). It is noteworthy that reflections from the higher bands were still distinguishable after doping process, indicating the high structural quality of all the i-cSi-o samples. In addition, Figure 4.1d also shows their well ordered inverse opal structure.

Moreover, Figure 4.2 shows one example (phosphorus doped i-cSi-o) of a comparison for reflectance spectrum with theoretical calculation, that are well matched.

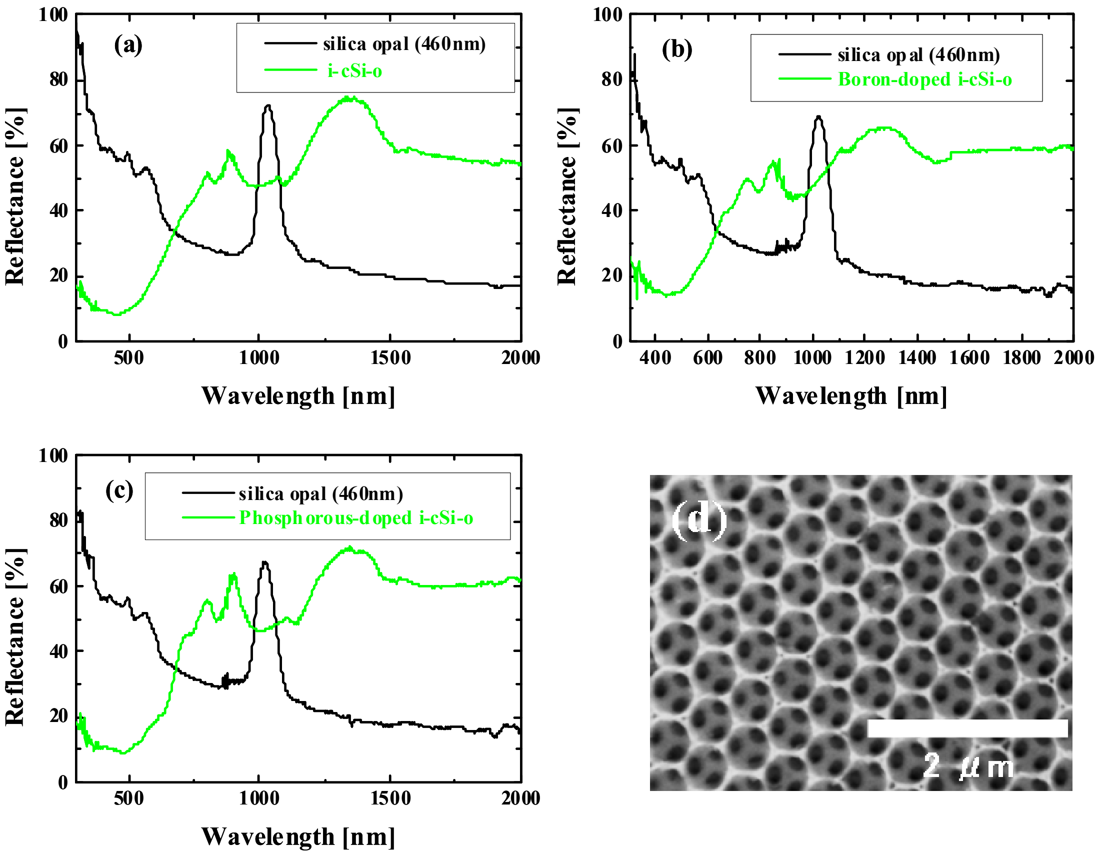

**Figure 4.1** Reflectance spectra of silica opal and inverse crystalline silicon opal (i-cSi-o) for sphere sizes 460 nm depicted as black and light green respectively for non-doped (a), boron-doped (b) and phosphorus-doped (c) films. SEM image of phosphorus-doped i-cSi-o (d).

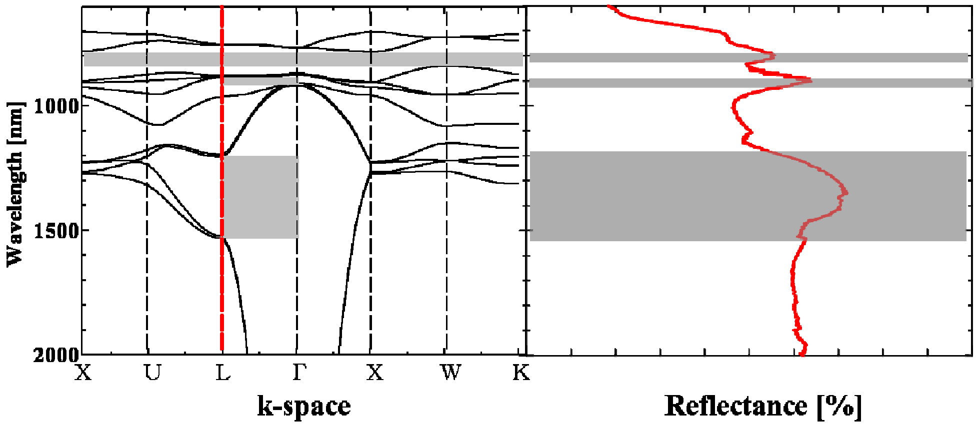

**Figure 4.2** A comparison of optical property of i-cSi-o from theoretical calculation and experimental result. The left side is a photonic band diagram for i-cSi-o fabricated by silica spheres with 460 nm for diameter from theoretical calculation. The right side is a Reflectance spectrum of i-cSi-o obtained from 460 nm spheres.

### 4.3.2. Electrical Properties of PN Doped i-cSi-o

Figure 4.3 shows the dc electrical dark conductivity ($\sigma_d$) of non-doped and doped i-cSi-o with or without HPP and that of c-Si thin film for comparison. Both p-type (boron-doped) and n-type (phosphorus-doped) i-cSi-o have higher $\sigma_d$ ($5.47\times10^{-4}$ S/cm and $4.27\times10^{-5}$ S/cm, respectively) than that of intrinsic (i-type) i-cSi-o ($1.45\times10^{-6}$ S/cm), suggesting that both boron and phosphorus were incorporated into the i-cSi-o as dopants and that they enhance the dc electrical dark conductivity of the inverse opal. Usually the process of dopant diffusion with such sol-gel type precursors requires higher annealing temperature (e.g. 900˚C); however our results show that the process was effective even at low temperature such as 630˚C upon prolonged annealing. This process is advantageous because it requires neither toxic doping gas nor substrates with high temperature resistivity.

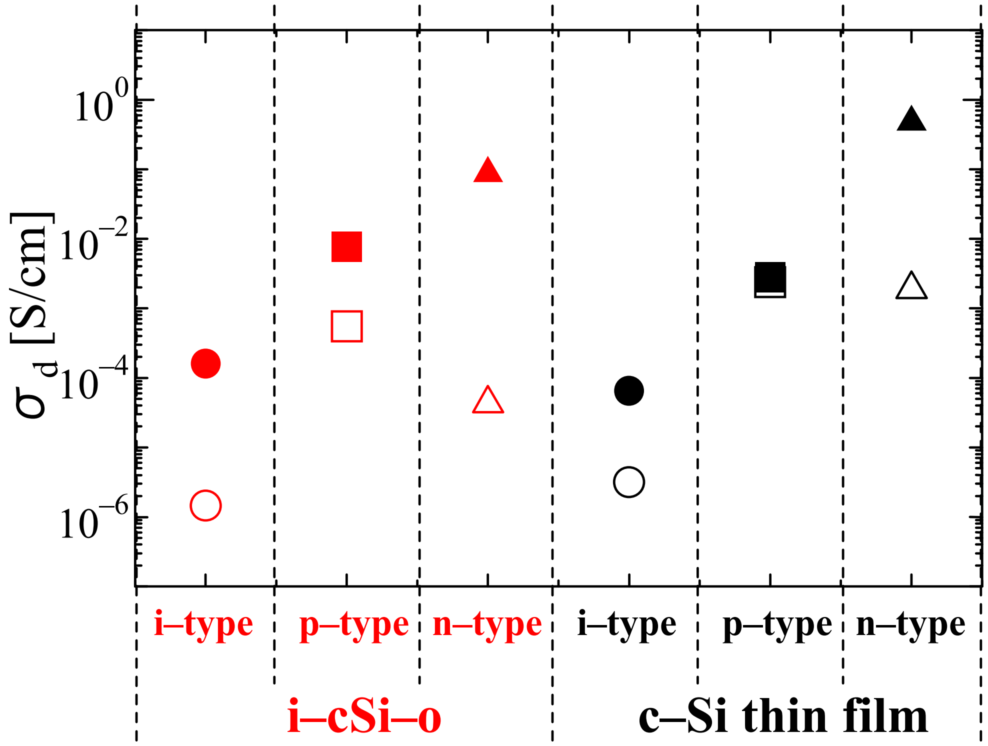

**Figure 4.3** A plot of σd with respect to i-type (circle), p-type (square) and n-type (triangle) for i-cSi-o (red) and c-Si thin film (black) with HPP (solid) or without HPP (open) obtained from 460 nm silica spheres.

As shown in Figure 4.3, HPP increases $\sigma_d$ for all films, with $\sigma_d$ reaching $1.60\times10^{-4}$ S/cm for i-type, $7.79\times10^{-3}$ S/cm for p-type and $8.72\times10^{-2}$ S/cm for n-type. The $\sigma_d$ increased by a factor of 110, 14 and 2045 for i-, p- and n-type, respectively, after HPP. On the contrary, the increase in $\sigma_d$ of c-Si by HPP is smaller (by a factor of 21, 1.2 and 254 for i-type, p-type and n-type, respectively) than for i-cSi-o. This finding suggests that HPP is more efficient for i-cSi-o than c-Si thin film, but to a different degree depending on the dopant. In i-cSi-o, the open framework structure with high porosity and large surface area allowed hydrogen radicals to penetrate more deeply inside the structure and efficiently terminate defects like dangling bonds, as reported in our previous work. However the effect of HPP on p-type and n-type i-cSi-o could be different from i-type. We believe that HPP not only passivates defects but also activates the dopants. For i-cSi-o and c-Si films, the n-type is much more sensitive to HPP than p-type. It may be due to the different energy states created in SPC Si by boron or phosphorus as the accepter state created by boron is deeper than the donor state created by phosphorus; hence boron in SPC Si is harder to activate than phosphorus.

To understand the quality of these Si samples as semiconductors, we studied the temperature dependence of $\sigma_d$. Figure 4.4 shows the $\sigma_d$ of i-cSi-o and c-Si thin film with HPP as a function of reciprocal temperature. All samples show activated behavior [8] over the entire temperature range with an activation energy of 0.272 eV for i-type, 0.049 eV for p-type, and 0.039 eV for n-type i-cSi-o, and 0.292 eV for i-type, 0.043 eV for p-type, and 0.023 eV for n-type c-Si thin films. As HPP decreased the grain-boundary potential barriers originated from the Si dangling bonds [8], the films exhibit linear logarithmic temperature dependence of $\sigma_d$. The data show that both i-type i-cSi-o and c-Si thin film are acceptable as high quality semiconductors.

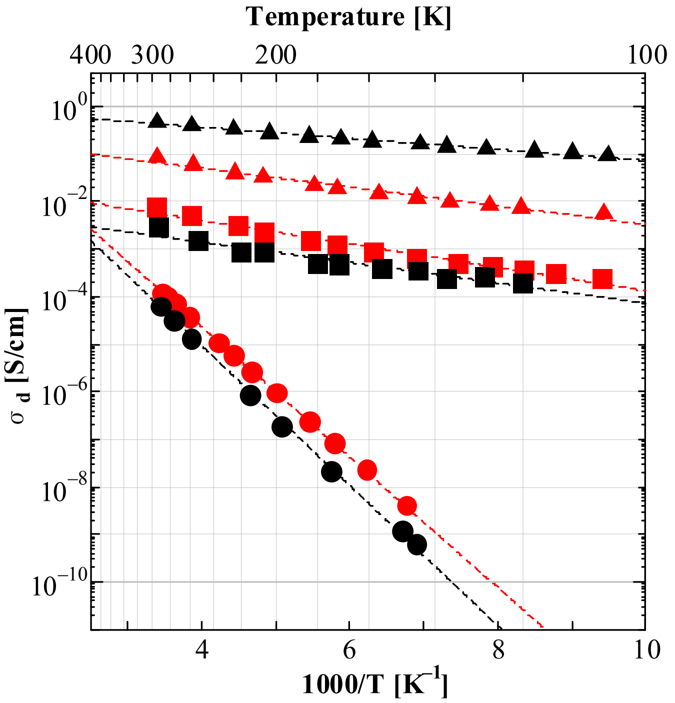

**Figure 4.4** Temperature dependence of $\sigma_d$ for i-type (circle), p-type (square) and n-type (triangle) c-Si thin films (black) and i-cSi-o (red) with HPP. The data were fitted with exponential curves $\sigma_d = \sigma_0 \exp(-E_a/k_BT)$ to obtain the activation energies.

Note that in both i-cSi-o and c-Si thin film, p-type and n-type samples show much smaller activation energies than i-type. The activation energy of doped semiconductors is strongly correlated to the donor or acceptor energy state, with their energy difference to conduction band or valence band being very close to the measured value of activation energy. Moreover, the activation energy of p-type is slightly larger than that of n-type in both cases, suggesting that boron created deeper energy state than phosphorus, also in line with our observation on the different changes in $\sigma_d$ upon HPP.

The results of $\sigma_d$ and the HPP effect provide adequate corroboration that boron and phosphorus sol-gel solutions are effective dopant diffusers for generating doped semiconductor materials. The overall $\sigma_d$ of i-type, p-type and n-type i-cSi-o after HPP and its linear logarithmic temperature dependence suggest promising opportunities for their use as semiconductors in devices like thin film Si solar cells that typically require $\sigma_d$ in the range from $10^{-5}$ to $10^{-0}$ S/cm.[7]

### 4.3.3. Dopant Detection

EDX and WDX technique were operated to detect dopants in i-cSi-o. Figure 4.5 shows the WDX spectra conjunct with EDX for i-cSi-o phosphorus doped i-cSi-o (a) and undoped i-cSi-o (b). Despite the signals were quite weak, the energy identified to phosphorus (2.01 keV) was detected for the sample of intentionally doped i-cSi-o (a), in contrast other one (b) had no specific structure in that spectrum around 2 keV. The sensitivity of WDX technique for phosphorus in silicon is no lower than 0.1 %, which is a reasonable value as phosphorus doping concentration.

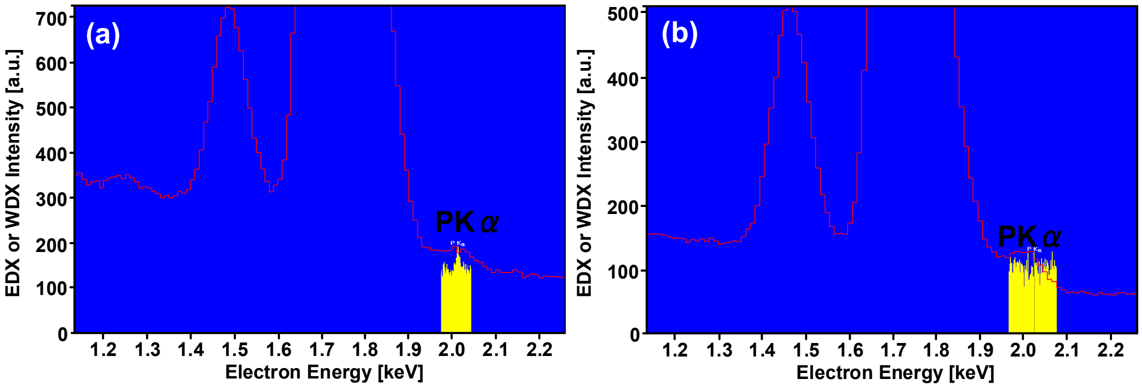

**Figure 4.5** WDX (yellow) spectra conjunct with EDX (red) for phosphorus doped i-cSi-o (a) and undoped i-cSi-o (b)

On the other hand, the WDX spectra for both boron doped i-cSi-o and undoped i-cSi-o show the weak peak at the energy assumed to boron (0.17 keV) in Figure 4.6a and b. It is assumed that the concentration of boron should be lower than the limit of WDX sensitivity and some noise signal must be observed because the detection of low contained boron is one of the most difficulties for WDX. However, that result was not so peculiar and told us that the concentration of boron in i-cSi-o must be lower than 0.1 % and in fact that value was quite reasonable from the results of conductivities which were 10 times lower than that of phosphorus doped i-cSi-o.

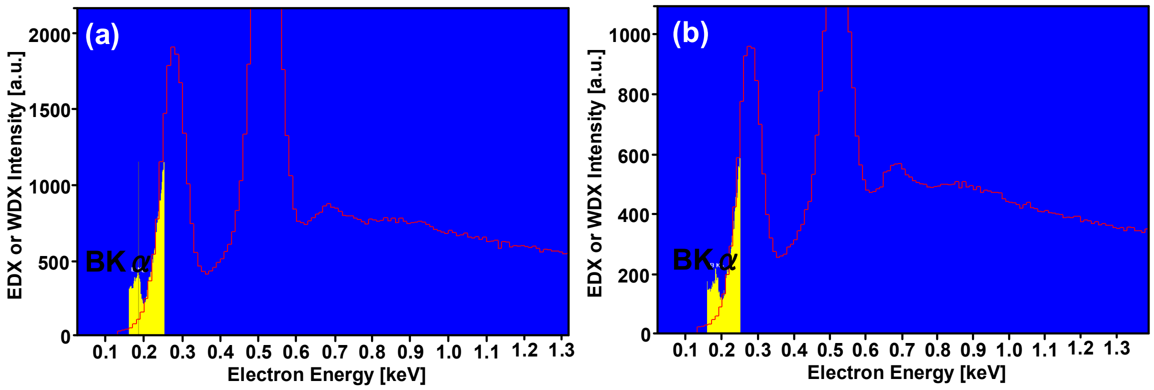

**Figure 4.6** WDX (yellow) spectra conjunct with EDX (red) for boron doped i-cSi-o (a) and undoped i-cSi-o (b)

## 4.4 Conclusions

In summary, the first examples of boron and phosphorus doped inverse crystalline silicon opals have been fabricated and evaluated their electrical conductivity. Hydrogen Plasma Passivation improved the conductivities of both doped and un-doped i-cSi-o; in particular the electrical conductivities of p-type and n-type i-cSi-o are higher than that of i-cSi-o. Through chemcially controlled doping we have achieved for the first time electrically conducting inverse silicon opals that are acceptable for device applications.

## 4.5 References

[1] T. Suezaki, P. G. O'Brien, J. I. L. Chen, E. Loso, N. P. Kherani and G. A. Ozin, Adv. Mater., 21, 559, **2009**.

[2] E. Yablonovitch, A. G. Fitzgerald, *J. Opt. Soc. Am.*, **1982**, *72,* 899.

[3] Y. Masaki, P. G. LeComber, A. G. Fitzgerald, *J. Appl. Phys.*, **1993**, *74,* 129.

[4] V.M. Arole, R.O. Dusane, M.G. Takwale, B.R. Marathe, V.G. Bhide, *Solar Energy Mater.*, **1988**, *17*, 391.

[5] E. Hecht, in *OPTICS 4th ed*, (Eds: A. Black), Addison Wesley, San Francisco, CA, USA **2002.**

[6] K. Busch, S. John, *Phys. Rev. E.,* **1998***, 58,* 3896.

[7] J. Meier, S. Dubail, J. Cuperus, U. Kroll, R. Platz, P. Torres, J.A. Anna Selvan, P. Pernet, N. Beck, N. P. Vaucher, Ch. Hof, D. Fischer, H. Keppner, A. Shah, *J. Non-Crystal. Solids*, **1998**, *227–230*, 1250.

[8] N. H. Nickel, in *Hydrogen in semiconductors II (semiconductors & semimetals vol 61)*, (Eds: R. K. Willardson, E. R. Weber), ACADEMIC PRESS, San Diego, CA, USA **1999.**

# CHAPTER 5

## Opto-Electrical properties of i-cSi-o

### Abstract

While the electrical properties of inverse silicon opals have been evaluated and revealed their promising qualities for semiconductor device application, it must be known about the behavior of optically generated electrical carriers for opto-electrical device applications like solar cells. In this chapter, spectral responses for the electrical properties of inverse silicon opals are evaluated and show a correlation with photonic band gaps. In particular, enhanced photoelectric generation by slow photons is observed at the bandedges of photonic bands.

### 5.1 Introduction

The previous chapters showed that the inverse crystalline Si opal (i-cSi-o) with its three-dimensional open-framework microstructure has comparable conductivity to crystalline Si (c-Si), controllable conductivity and therefore a capability for photovoltaics. [1, 2] However, to incorporate photonic crystals into photovoltaics as photoelectric generation layers to amplify photon to electron conversion efficiencies, it is important to exploit the unique features of photonic crystals, such as slow photons and forbidden optical stopgaps or complete photonic bandgaps for light trapping or suppression of carrier recombination. So far the correlations between photonic crystal structures and carrier transport are still unknown. Since one of the most interesting and essential slow photon effects is expected to be a significant enhancement for light trapping in photovoltaics, the spectral response of the electrical properties of i-cSi-o, focusing on the quantum efficiency of as-synthesized i-cSi-o and the effect of hydrogen plasma passivation on its quantum efficiency, were investigated.

## 5.2 Experimental Methods

### 5.2.1. Spectral Response measurement

The spectral responses for the electrical properties were measured at low temperature to reduce contributions of thermally activated carriers. Figure 5.1 shows a sketch of the measurement system for the spectral response of the electrical properties. The sample is placed on the sample stage of a low temperature measurement system (Nagase Co.), which has manipulative probes for electrical measurements and a quartz observation window above the sample stage. A focusing lens is set above the quartz window to focus monochromatic light just on the sample surface between two aluminum electrodes. A Xe lamp is used as a light source and the wavelength dependence of its power output is measured by a power meter after the lamp intensity had stabilized.

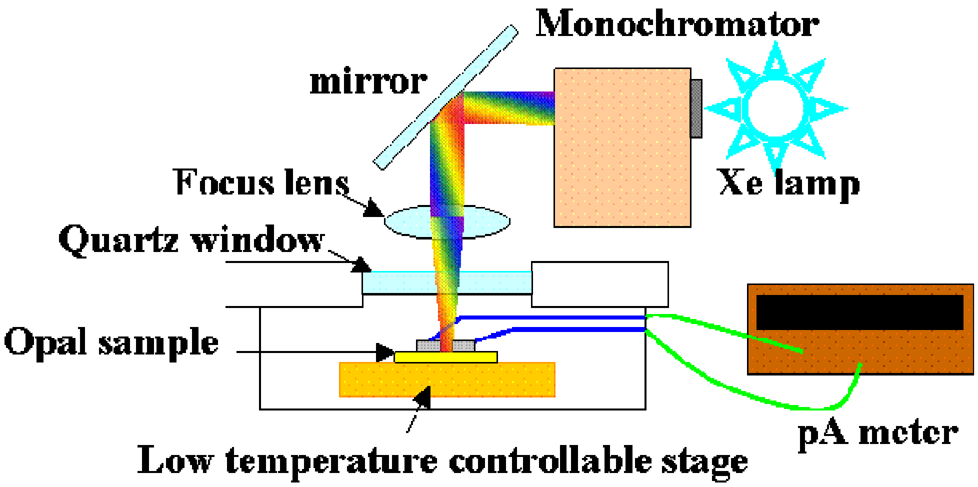

**Figure 5.1** Illustration of the measurement system for the spectral response of the electrical properties of i-cSi-o.

## 5.3 Internal Quantum Efficiency for i-cSi-o

### 5.3.1. Correlations of Photonic Band Gaps to Photo Conductivities for i-cSi-o

To evaluate the spectral response for the electrical properties of i-cSi-o, firstly the i-cSi-o films on sapphire substrates were fabricated, as reported previously. Silica spheres with

600 nm and 280 nm diameters for i-cSi-o templates were prepared to compare the correlation of slow photon driven electrical responses with photonic band structures. Each fabricated i-cSi-o from 600 nm or 280 nm spheres has approximately 11 layers or 26 layers respectively. [See in Figure 5.2] The reflectance spectra of i-cSi-o obtained from 600 nm and 280 nm silica spheres are depicted at Figure 5.3 with black and gray, respectively. The i-cSi-o from 600 nm has the stop band reflection at 1770 nm and two distinctive higher bands in the infrared range at 1146 nm and 1028 nm, with the latter corresponding to the energy of the complete photonic bandgap as predicted by theoretical calculations. [See in Figure 5.4] The i-cSi-o from 280 nm spheres; kept good fcc structure as well; has the stopband reflection at 926 nm and two distinctive higher bands at 604 nm and 546 nm (complete photonic bandgap), that correspond to the theoretical calculations and two higher bands were placed in visible range. Not only from SEM image but also the observation of higher order reflections and the correspondence to the theoretical predictions show that i-cSi-o has retained its good structural order as 3D photonic crystals.[1,2]

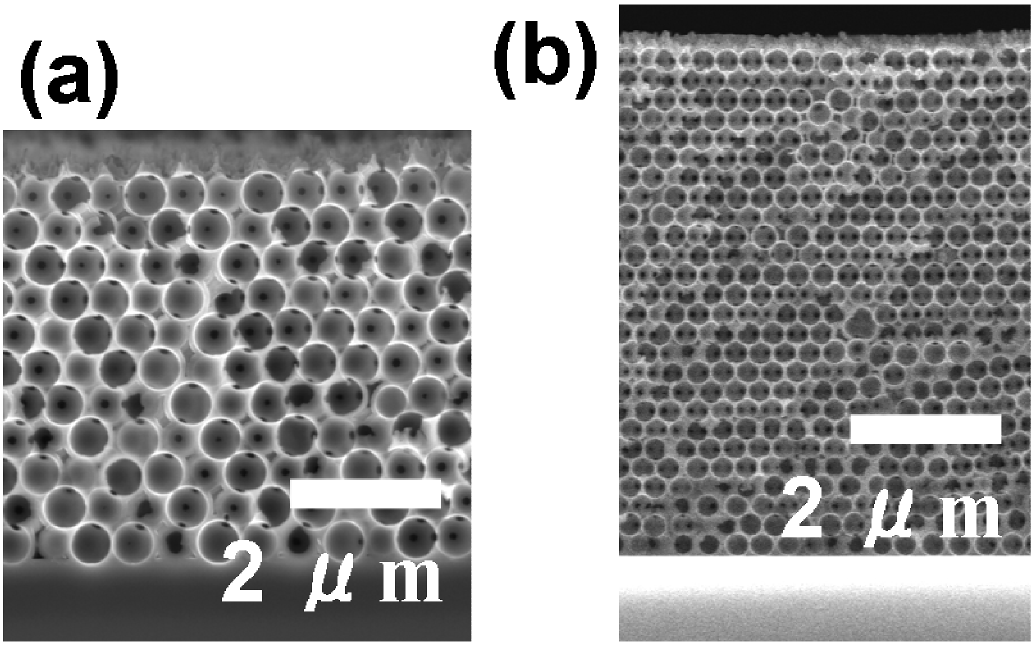

**Figure 5.2** Cross sectional SEM image of i-cSi-o obtained from 600 nm spheres (a) and 280 nm (b) on sapphire substrates. The bottom side of images is sapphire substrate.

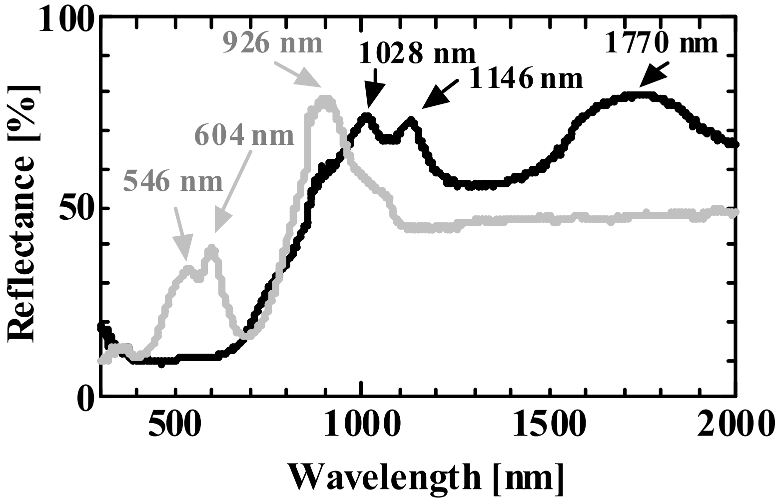

**Figure 5.3** Reflectance spectra of i-cSi-o obtained from 600 nm spheres (black) and 280 nm spheres (gray). The arrows with numbers point to the peak positions of reflectance spectra.

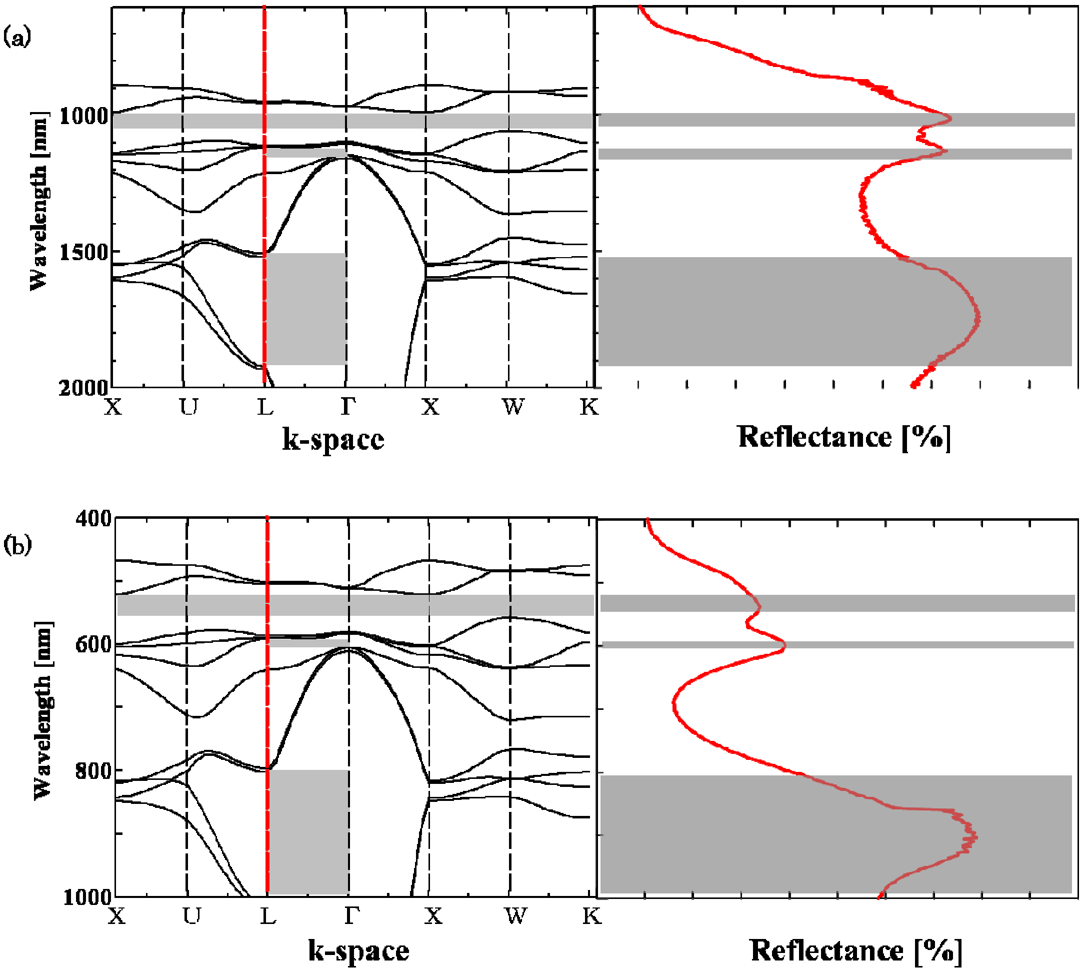

**Figure 5.4** Comparison of optical photonic properties of i-cSi-o from theoretical calculation and experimental result for that of obtained from 600 nm spheres (a) and 280 nm spheres (b). The left side is a photonic band diagram for i-cSi-o from theoretical calculation. The right side is the corresponding experimental reflectance spectrum of i-cSi-o.

Prior to studying the internal quantum efficiency (IQE) for the i-cSi-o, the temperature dependence of the dc electrical dark conductivity ($\sigma_d$) for i-cSi-o were measured using a two probe method to confirm the behavior of carrier transport in i-cSi-o. Aluminum co-planar electrodes with a separation of 1 mm were evaporated on the surface of the samples by a physical vapor deposition apparatus. To measure $\sigma_d$, the current was recorded while the bias across the electrode pair was increased from -100 V to +100 V in increments of 20 V. The $\sigma_d$ was determined from the resulting I-V curves, which were linear implying a good ohmic contact between the aluminum and the i-cSi-o, with the equation $\sigma_d$ =IL/VS, where L is the gap length between two electrodes and S is the cross sectional area of the films. The area includes not only the Si framework but also the void spaces. Figure 5.5 shows the $\sigma_d$ of i-cSi-o prepared from silica spheres with diameters at 600 nm or 280 nm as a function of reciprocal temperature. Above 133 K, $\sigma_d$ shows activated behavior with an activation energy of 0.285 eV for 600 nm and 0.276 eV for 280 nm. Below 133 K, another behavior is observed, consistent with variable range hopping conductivity, also known as Mott conductivity as we reported in Chapter 3. Therefore we compared the behavior of the dc photo current at 100 V dc bias for i-cSi-o with diameters of 600 nm and 280 nm under irradiation with various wavelength monochromatic light at 133 K, not only for reducing contributions of thermally activated carriers but also for minimizing the effect of currents from variable hopping.

The IQE is obtained from these equations,

$$\mathbf{IQE = EQE / (1\text{-}R\text{-}10^{-A})} \qquad \mathbf{(5.1)}$$

$$\mathrm{EQE} = \frac{\mathrm{electrons/sec}}{\mathrm{photons/sec}} = \frac{\mathrm{current/(charge\ of\ 1\ electron)}}{\mathrm{(total\ power\ of\ photons)/(energy\ of\ one\ photon)}} \qquad \mathbf{(5.2)}$$

where EQE is the external quantum efficiency, R and A are the reflectance and the absorbance. A was about 2 to 3 for the both i-cSi-o at the measured range, therefore the influence of absorbance was almost negligible.

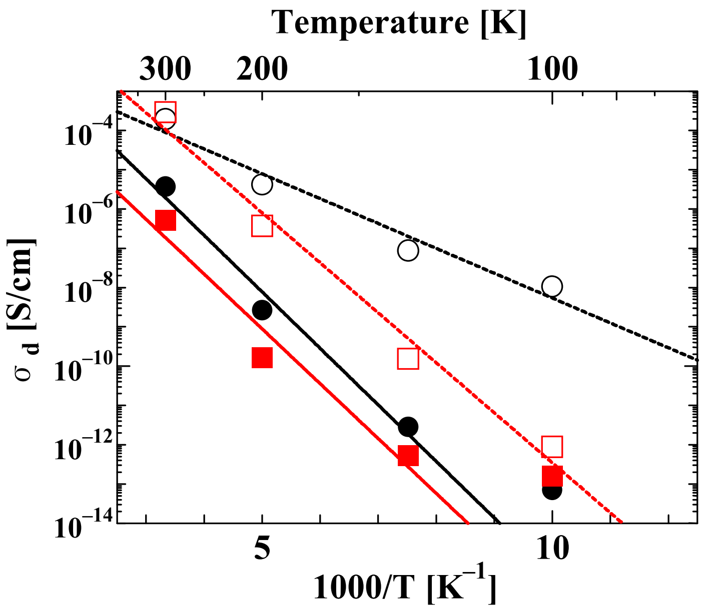

**Figure 5.5** Temperature dependence of $\sigma_d$ for i-cSi-o obtained from 600 nm spheres (black circle) and 280 nm spheres (red square); without HPP (solid) and with HPP (open). The data were fitted with exponential curves $\sigma_d = \sigma_0 \exp(-E_a/k_BT)$ to obtain the activation energies.

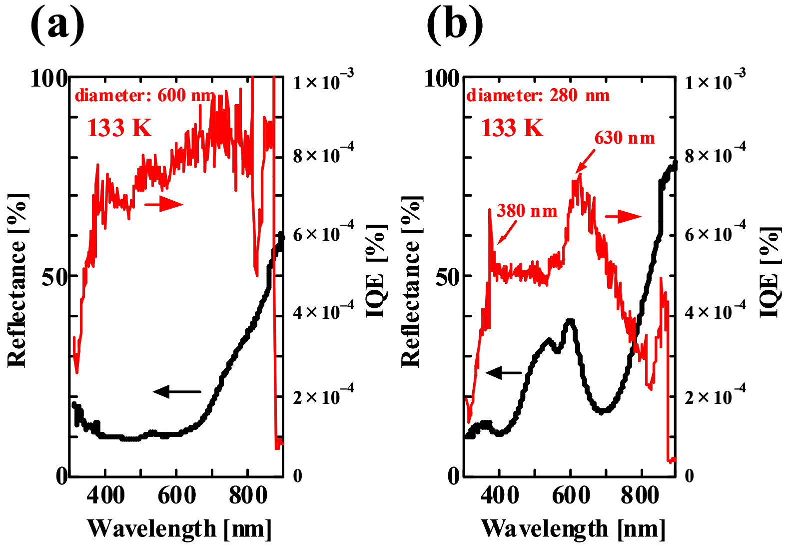

**Figure 5.6** (a) The IQE before HPP treatment at 133 K for i-cSi-o obtained from 600 nm spheres (red) and the corresponding reflectance spectrum (black). (b) The IQE before HPP treatment at 133 K for i-cSi-o obtained from 280 nm spheres (red) and the corresponding reflectance spectrum (black). The arrows with numbers point to the peak positions of the IQE spectra.

Figure 5.6a shows the IQE at 133 K for i-cSi-o made from silica spheres with a 600 nm diameter and the corresponding reflectance spectrum. The IQE for i-cSi-o from 600 nm didn't show any specific correlation to the reflectance spectrum. On the contrary, the IQE for i-cSi-o from 280 nm showed a relatively narrow peak at 630 nm and a shoulder at 380 nm, which almost coincide with its reflection spectrum (Figure 5.6b). It is interesting that both results showed the existence of a dependence of the IQE on the three dimensional architectures and spectral properties of the photonic crystal lattices.

### 5.3.2. Effect of Hydrogen Plasma Passivation to IQE

Both i-cSi-o films were then removed from the low temperature system and placed into a plasma treatment reactor for undergoing hydrogen plasma passivation (HPP). As it was reported in Chapter 3, HPP increases $\sigma_d$ for i-cSi-o films remarkably and decreases the grain-boundary potential barriers originated from the silicon dangling bonds. [1] Indeed $\sigma_d$ for both i-cSi-o films improved by a factor of 100 to 10000 times in this study too (Fig. 5.5). The difference between the activation energy of i-cSi-o from 600 nm (0.125 eV) versus 280 nm (0.252 eV) sphere templates is that the former may contain more deep dopant levels by contamination during the fabrication process than the latter.

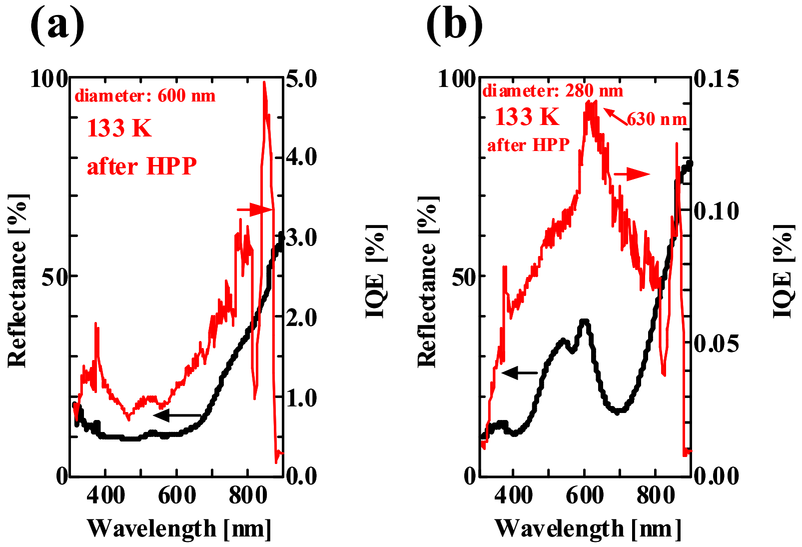

**Figure 5.7** (a) The IQE after HPP treatment at 133 K for i-cSi-o obtained from 600 nm spheres (red) and the corresponding reflectance spectrum (black). (b) The IQE after HPP treatment at 133 K for i-cSi-o obtained from 280 nm spheres (red) and the corresponding reflectance spectrum (black). The arrows with numbers point to the peak positions of the IQE spectra.

To observe the effects of HPP for IQE of i-cSi-o films, the IQE at low temperatures of the HPP treated i-cSi-o samples made from both 600 nm and 280 nm spheres were re-measured. Figure 5.7 shows shows the IQE spectra at 133K of the HPP treated i-cSi-o sample made from both 600 nm (a) and 280 nm (b) spheres and the corresponding reflectance spectrum, which also explain improvements of photo-conductivities by HPP. Photo-conductivity is strongly correlated to minority carrier lifetime that is influenced by defects, therefore the improvement of IQE was a proof of HPP effect. The IQE after HPP for i-cSi-o from 600 nm showed increasing trend via long wavelength, however no specific correlation with reflectance was observed. (discussed at 5.4) On the contrary, the IQE after HPP for i-cSi-o made from 280 nm kept a relatively narrow peak at 630 nm as well as before HPP; however a shoulder at 380 nm was almost disappeared; which almost coincide with its reflection spectrum as well.

## 5.4 Observation of Slow Photon Effect

Figure 5.8 shows the enhancement ratio of the IQE spectrum for i-cSi-o sample made from both 600 nm (a) and 280 nm (b) spheres; we defined the value of "(IQE after HPP) / (IQE before HPP)" as an enhancement ratio"; with the reflectance spectrum for i-cSi-o at 133 K after HPP. As mentioned above, i-cSi-o made from 280 nm spheres has the most obvious dependence of IQE with the photonic bands in the measured wavelength range and therefore it is expected that noticeable effects of HPP on the IQE should also be observed. Hence we firstly focus on the results for i-cSi-o made from 280 nm spheres. The average ratio for the IQE at the measured wavelength range is found to be 175, which is close to the ratio for $\sigma_d$ (290) by HPP. However, the enhancement ratio of IQE is not constant as a function of wavelength but instead possesses interesting behavior, which shows an increasing trend towards longer wavelength and a correlation with the reflectance spectrum.

It is assumed that the increasing trend could be explained by a mechanism for transportation of electrical carriers in the semiconductor with carrier trap states. The carriers that are generated by low energy longer wavelength photon have a small excess energy at the conduction states because carriers need a certain amount of energy to overcome electrical bandgaps. In the case of the semiconductor with a large amount of trap states, it is difficult for such generated carriers with small energy not to be trapped before reaching the electrodes. However, HPP deactivated those trap states remarkably and the IQE at longer wavelength improved much more than shorter wavelength.

It is also probable that the correlation of the effect of HPP on IQE is a sign of the operation of the slow photon effect which is expected to be observed at the edges of photonic bandgaps. As HPP decreased the grain-boundary potential barriers originating from the Si dangling bonds, the lifetime of photogenerated carriers improved and that could make the slow photon effect more obvious. In fact, our results showed a larger increase in the enhancement ratio not only on the edges of photonic band-gaps but also on the photonic bandgaps, likely originating from the structural imperfection of the i-cSi-o millimeter size samples. As it was mentioned in Chapter 2, i-cSi-o materials have some defects related structural disorder nevertheless it is quite remarkable that enhancement of the IQE by HPP were higher around photonic bandgaps even with such structural imperfection, and is considered to be an encouraging indicator of slow light trapping effects in silicon photonic crystal photovoltaics.

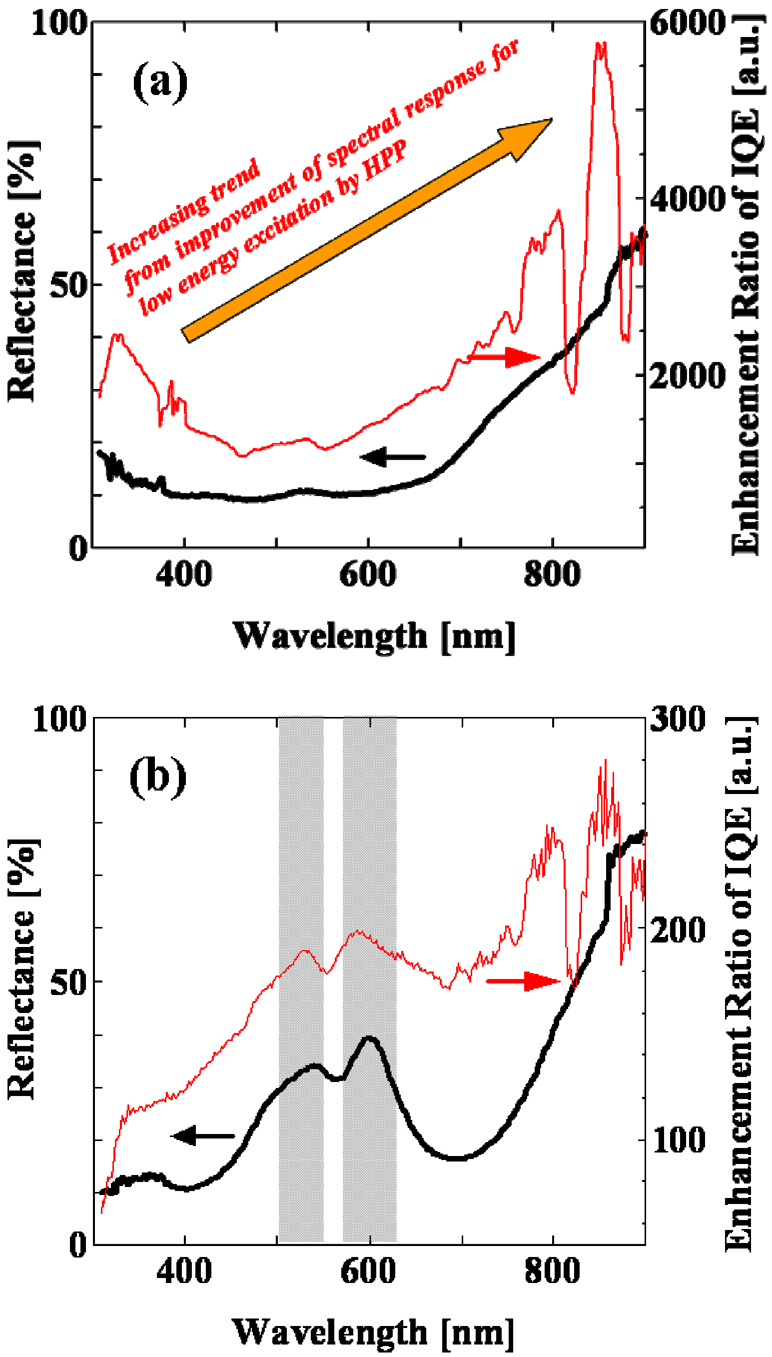

**Figure 5.8** The enhancement ratio of the IQE spectra (red) for i-cSi-o obtained from 600 nm (a) and 280 nm (b) spheres at 133 K after HPP with that of the corresponding reflectance spectra.(black). Shaded wavelength areas in (b) are assumed IQE enhancements by slow photon effect.

In contrast, the case of i-cSi-o obtained from 600 nm spheres does not seem to show slow photon correlation.(Figure 5.8a) However increasing trend via long wavelength are observed as well as Figure 5.8b because that effect should be originated from a mechanism for transportation of electrical carriers in the semiconductor with carrier trap states as it was discussed in the text. The behavior of the enhancement ratio for i-cSi-o made from 600 nm spheres  in the Ultra-Violet range was different and the ratio was slightly higher than visible range, which might come from complex surface conduction or influence of contamination in Si matrix on i-cSi-o. However, at least it is less important at the UV range behaviour for photovoltaic application due to existence of absorption loss by front TCO or emitter.

## 5.5 Conclusions

In summary, internal quantum efficiencies for inverse crystalline silicon opals were evaluated. The correlation between photonic band structures and IQE was observed clearly at low temperature. Hydrogen plasma passivation improved the IQE of i-cSi-o; in particular in the longer wavelength range because of the deactivation of trap states by HPP. Furthermore, slow photon enhanced photoconductivity effects of i-cSi-o were observed around photonic bandgaps providing evidence for enhancement of the photon to electron conversion efficiency of silicon solar cells.

## 5.6 References

[1] T. Suezaki, P. G. O’Brien, J. I. L. Chen, E. Loso, N. P. Kherani and G. A. Ozin, Adv. Mater., 21, 559, **2009**.

[2] T. Suezaki, J. I. L. Chen, T. Hatayama, T. Fuyuki and G. A. Ozin, Appl. Phys. Lett., 96, 242102, **2010**.

# CHAPTER 6

# Device Application for Optically Enhanced Thin Film Silicon Photonic Crystal Solar Cells

## Abstract

Up to now, silicon photonic crystals have been observed its promising properties for opto-electrical device application like solar cells. To demonstrate the potential of i-cSi-o for opto-electrical devices, a prototype p-i-n junction solar cell based on the inverse silicon opal is reduced to practice and its opto-electronic behaviors are evaluated.

## 6.1 Introduction

Since several studies have demonstrated the potential advantages of photonic crystals for many applications such as optical telecommunications,[1,2] light emitting diodes, [3] lasers,[4,5] waveguides, [6,7] photocatalysts, [8] displays[9,10] and solar cells.[11-13] As it has been discussed, the inverse silicon opal (i-Si-o) has a great potential for applications because of its demonstration of complete photonic bandgap and the ability to be synthesized on a large scale.[14] So far, previous chapters have showed that the inverse crystalline Si opal (i-cSi-o) with its three-dimensional open-framework microstructure has comparable conductivity as crystalline Si (c-Si) in spite of its high porosity and holds intriguing photonic properties for opto-electronic interactions. Therefore the first example of a simple photovoltaic device based on i-Si-o materials has been fabricated and evaluated its performance herein.

## 6.2 Experimental Methods

### 6.2.1. Fabrication of PIN Structures

On a borosilicate glass substrate, a n-type micro-crystalline Si (n:μc-Si) thin film was deposited of 100 nm thickness by RF plasma enhanced CVD (RF-PECVD) apparatus with monosilane, hydrogen and phosphine gas at a substrate temperature of 200˚C, on top of which an i-type i-cSi-o film, obtained from silica microspheres with diameter 460 nm, with 5 µm thickness was fabricated followed by HPP. After HPP processing, a p-type micro-crystalline Si (p:µc-Si) film was deposited on top of i-type i-cSi-o by the RF-PECVD apparatus with monosilane, hydrogen and diborane gas at substrate temperature of 200˚C through the 5 mm square sized holes of stainless steel mask. The indium tin oxide (ITO) front electrode was deposited on the p:µc-Si thin film layer by sputtering. It should be noted that the p:µc-Si and ITO film infiltrated negligibly into the i-cSi-o film but localized instead on the of top of i-cSi-o film. To obtain the back-side electrical contact, ultra-sonic soldering system was used to allow the solder to penetrate the i-cSi-o layer and reach n:µc-Si thin film layer. As a comparison, we also prepared same solar cell structure for i-type c-Si film with 1 µm thickness; the i-type c-Si volume is almost same as 5 µm i-type i-cSi-o; in the same process. Figure 6.1 shows a schematic of the cross section of the simple solar cell structure.

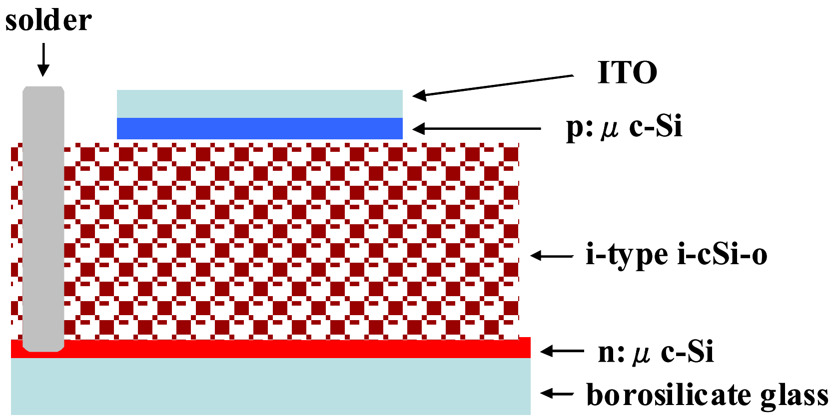

**Figure 6.1** Cross sectional schematic of the i-cSi-o solar cell structure.

### 6.2.2. I-V measurement of Solar Cells

The current-voltage characteristics of the pSi/i-cSi-o/nSi solar cell were measured under the air mass 1.5 radiation of solar simulator (Wacom) at 25 ˚C.

### 6.2.3. Measurement of External Quantum Efficiency for Solar Cells

The quantum efficiency was measured by a spectral response measurement system (BUNKOUKEIKI Co.,Ltd) at room temperature.

## 6.3 Photovoltaic Properties of Thin Film Silicon Photonic Crystal Solar Cells

The optical properties of the i-cSi-o on n:µc-Si deteriorated somewhat due to challenges of obtaining high quality opal templates on thin film silicon prepared on glass substrate because of low resistivity against HF etching process and different surface wettability. However, reflection from the photonic stop band is still observed around 900 nm; there should be two peaks of second and third band for the case of high quality; as seen in Figure 6.2.

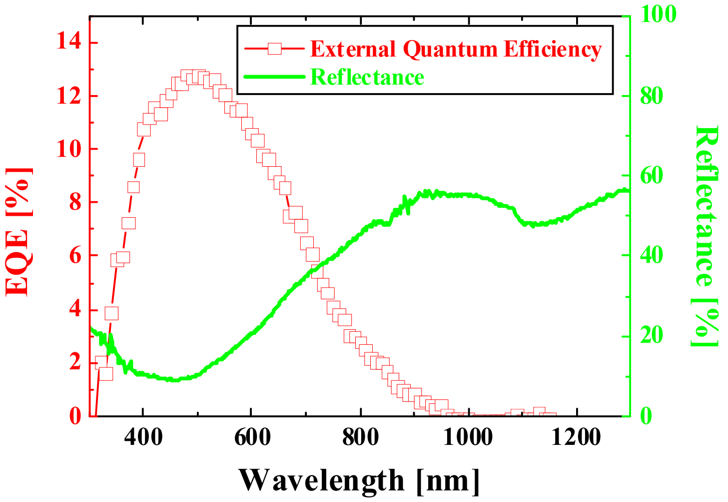

**Figure 6.2** The external quantum efficiency (open red square with red line) and the reflectance spectrum (light green line) of the i-cSi-o solar cell structure

Figure 6.3a shows the current-voltage characteristic of the structure with i-cSi-o under the air mass 1.5 radiation; the behavior typical of a photovoltaic device is observed. It is quite remarkable that the e-h charge carriers were able to separate across the macroporous i-type i-cSi-o layer and that such a p-i-n junction could be reduced to practice. The conversion efficiency of the first reported i-cSi-o solar cell is 0.32%. The photo-current at reverse bias voltage is reasonably high, which proves the existence of a sufficient population of photogenerated e-h carriers. The high response of the external EQE from 400 nm to 700 nm depicted in Figure 6.2 provides support for the sufficient number of e-h carrier excitations.

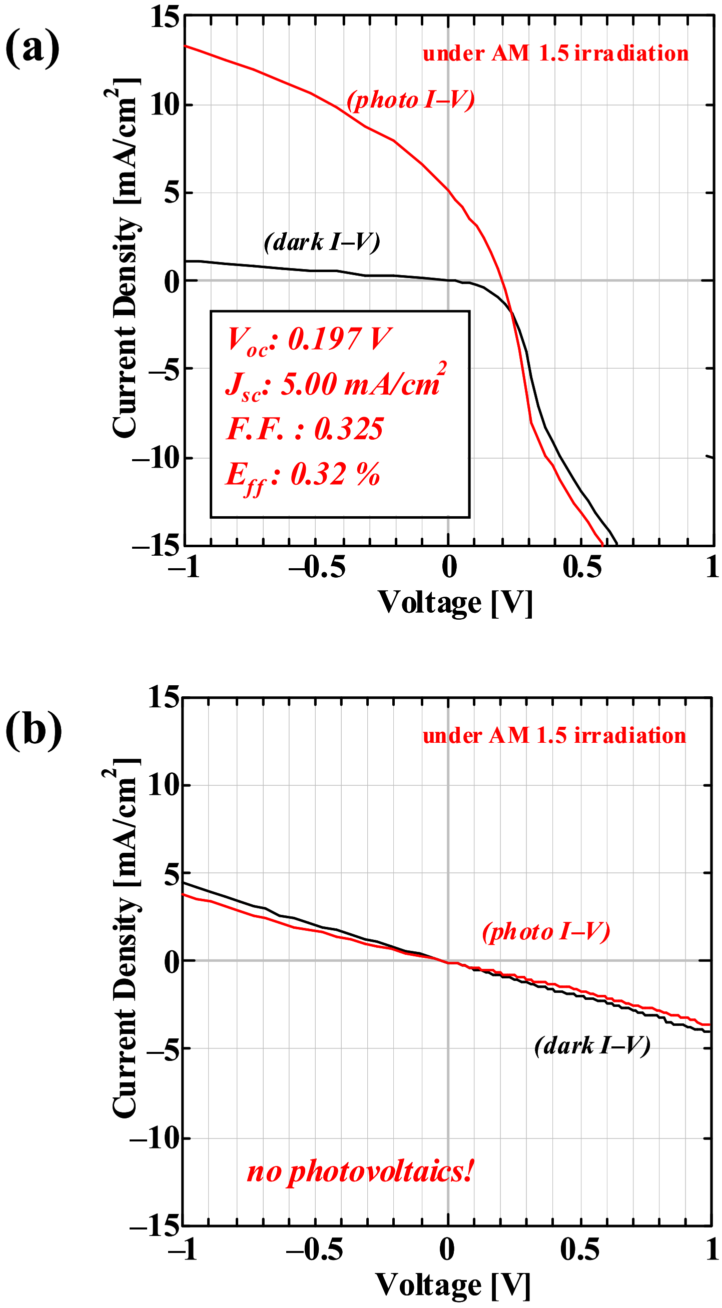

**Figure 6.3** The current-voltage characteristics of the i-cSi-o solar cell structure under dark condition (black) and under air mass 1.5 irradiation (red) are shown in (a). The current-voltage characteristics of the c-Si thin film solar cell structure under dark condition (black) and under air mass 1.5 irradiation (red) are shown in (b) for the comparison.

In contrast, the current-voltage characteristic of the structure with c-Si thin film doesn't show any photovoltaics (Figure 6.3b) due to its quite high resistance. Its performance and high possibility of a SPC solar cell has been investigated previously [15,16] where researchers studied several special techniques such as crystallization, passivation, doping layer activation, interface treatment and electrical contact to realize high performance. Note that executed SPC techniques were still very preliminary and n: μc-Si is not in contact with any other high conductive electrode like metals or conductive oxides. The bottom electrode was not incorporated in the device structure due to the HF etching process. Hence in this structure, the n-layer itself must also posses high conductivity in the plane of the device, which may explain the differences in solar cell performance between that of i-cSi-o and c-Si. For i-cSi-o solar cell, the high porosity of i-cSi-o allowed hydrogen radicals to reach the n-layer and consequently HPP efficiently enhanced the conductivity of n-layer to a level that yielded overall solar cell behavior. On the other hand, the dense 1μm thick i-type c-Si thin film in the reference cell prevented the hydrogen radicals from reaching the n-type layer; hence the resistivity was not improved and no photovoltaic behavior could be observed.

However more interesting and important result was that the present solar cell structure for i-type i-cSi-o showed certain photovoltaics and actually enough high photocurrent considering our simple processes. It is quite possible that the high porosity of i-cSi-o and its high sensitivity to HPP improve the quality of i-cSi-o by SPC and that possibility shows huge hope for i-cSi-o solar cell.  In addition, at this stage of the work, the most important parameter is the photo-current. This is because at the reverse bias voltage employed the cell had a high enough current even without any special light trapping technology especially for such a small thickness cell of only 5 μm, clearly the fabricated pin silicon photonic crystal solar cell design showed enough electron-hole pair generation to make it interesting as a first step towards continuing optimization which was typical of the approach adopted by researchers skilled in the art. It is very difficult to get high current at zero volt or forward bias without good electrodes and good contact. So this device structure is considered to be extremely simple and no special techniques have been used to reduce the series resistance which is the main cause of the small current at zero volt or forward bias. It represents a significant step towards the practical realization of an optically enhanced solar cell based on i-cSi-o, which could show new and effective light trapping by slow photon and long life time for minority carriers from recombination inhibition by the feature of omni-directional photonic bandgap.Those distinctive feature of i-cSi-o can make conversion efficiency higher by high current and good fill factor. The efficiency can further be improved by some further processing, like treating the interface before the deposition of each layer, optimizing SPC condition, passivating with silicon nitride instead of hydrogen plasma, enhancing structural order of the opal film and device structure.

## 6.4 Conclusions

The first solar cell structure with an i-cSi-o active layer was fabricated, which will lead the way to uniquely integrate the omni-directional photonic bandgap of i-cSi-o with the semiconductivity of silicon for the express purpose of enhancing the photon to electron conversion efficiency of silicon solar cells. Further studies and improvements on the design, self-assembly and evaluation of i-cSi-o based silicon solar cells are underway.

## 6.5 References

[1] A. Blanco, E. Chomski, S. Grabtchak, M.Ibisate, S. John, S. W. Leonard, C. Lopez, F. Meseguer, H. Miguez, J. P. Mondia, G. A. Ozin, O. Toader, H. M. van Driel, *Nature,* **2000**, *405,* 437.

[2] Q. Yan, L. Wang, X. S. Zhao, *Adv. Funct. Mater.,* **2007***, 17,* 3695.

[3] Z. Xu, L. Cao, Q. Tan, Q. He, G. Jin, *Opt. Comm.,* **2007***, 278,* 211.

[4] T. Matsui, R. Ozaki, K. Funamoto, M. Ozaki, K. Yoshino, *Appl. Phys. Lett.,* **2002***, 81,* 3741.

[5] M. Ozaki, M. Kasano, D. Ganzke, W. Haase, K. Yoshino, *Adv. Mater.,* **2002***, 14,* 306.

[6] L. Vogelaar, W. Nijdam, H. A. G. M. van Wolferen, R. M. de Ridder, F. B. Segerink, E. Flück, L. Kuipers, N. F. van Hulst, *Adv. Mater.,* **2001***, 13,* 1551.

[7] F. Benabid, F. Couny, J. C. Knight, T. A. Birks, P. St J. Russell, *Nature,* **2005***, 434,* 488.

[8] J. I. L. Chen, G. von Freymann, S. Y. Choi, V. Kitaev, G. A. Ozin, *Adv. Mater.,* **2006***, 18,* 1915.

[9] R. C. Schroden, M. Al-Daous, C. F. Blanford, A. Stein, *Chem. Mater.,* **2002***, 14,* 3305.

[10] A. C. Arsenault, H. Miguez, V. Kitaev, G. A. Ozin, I. Manners, *Adv. Mater.,* **2003***, 15,* 503.

[11] S. Nishimura, N. Abram, B. A. Lewis, L. I. Halaoui, T. E. Mallouk, K. D. Benkstein, J. van de Lagemaat, A. J. Frank, *J. Am. Chem. Soc.,* **2003***, 125,* 6306.

[12] M. Florescu, H. Lee, I. Puscasu, M. Pralle, L. Florescu, D. Z. Ting, J. P. Dowling, *Solar Energy Mater. Solar Cells.,* **2007**. *91.* 1599.

[13] P. G. O'Brien, N. P. Kherani, S. Zukotynski, G. A. Ozin, E. Vekris, N. Tetreault, A. Chutinan, S. John, A. Mihi, H. Míguez, *Adv. Mater.,* **2007***, 19,* 4177.

[14] K. Busch, S. John, *Phys. Rev. E.,* **1998***, 58,* 3896.

[15] T. Matsuyama, N. Terada, T. Baba, T. Sawada, S. Tsuge, K. Wakisaka, S. Tsuda, J. Non-Crystal. Solids, 198-200, 940, **1996**,.

[16] M. J. Keevers, A. Turner, U. Schubert, P. A. Basore and M. A. Green, Proc. 20th European Photovoltaic Solar Energy Conf., Barcelona, 1305, **2005**.

# CHAPTER 7

# Outlook and Future Directions

## 7.1 Improvement Device Fabrication Process

The potential to enhance the photovoltaic efficiency of solar cells by inverse silicon opals has been explored in detail. While progress is still needed for actual devise applications (as discussed in Chapter 6), the use of some process optimizations that have been improved and utilized in semiconductor technology could solve problems.

### 7.1.1. Installation of Back Electrode

As it is discussed in Chapter 6, the pin solar cell with i-cSi-o for i-layer prepared in this work possessed high series resistance because of without collaboration of back electrodes. The n:μc-Si layer employed in this study formed i/n junction and internal electrical field, which could collect photo-generated electrons, however n:μc-Si layer by RF-PECVD is not high enough conductive electrically in the lateral direction. In general, a sheet resistance with less than 10 Ω/□, which can be converted to $10^4$ S/cm for 100 nm, is required for electrodes for solar cells. Either mono-crystalline or multi-crystalline (bulk) silicon solar cell is able to achieve such electrode with incorporation of relatively high conductive p or n-type layer by dopant diffusion techniques and grid electrodes. On the other hand, it is quite difficult for p or n-type layer of thin film μc-Si prepared by a standard RF-PECVD technique to get such high conductivity because of much higher electrical defects than that of bulk silicon, therefore metals or metal oxides or both of them are formed to make the ohmic contact with p or n-type layer and cover lateral electrical conduction. Even for thin film silicon, there exist a way to realize very high conductive n-type layer, [1] it needs quite high temperature processes.

For incorporation of back electrodes to solar cell structure with i-cSi-o for i-layer, HF etching process; which can etch metal or conductive metal oxide much faster that silica; is the biggest problem. There must be solutions for this difficulty and in fact one idea to resolve this problem is introducing here. Figure 7.1 shows the sketch of this process. Instead of silica opal, polystyrene opal is prepared on n: μc-Si film that is deposited on the aluminum doped zinc oxide (AZO) layer on silver (Ag) layer coated borosilicate glass. The polystyrene opal have been reported a lot [2, 3] and it's structural and optical qualities are enough comparable to silica opals. The polystyrene opal is then covered with silica thin layer (less than 10 nm) by layer-by-layer deposition that is alternating gas-phase treatment of silicon tetrachloride ($SiCl_4$) and water vapor ($H_2O$). [4] Following silica thin layer formation on polystyrene opal, CVD process for silicon infiltration and the over-layer removal by RIE are operated under the condition mentioned in Chapter 2. Even after CVD process at 480 ˚C, the opal structure is kept; that has been confirmed experimentally; due to silica thin layer on polystyrene microspheres. It is easy to remove polystyrene opal with organic solvent such as toluene or ashing in air plasma or air anneal and then i-aSi-o coated with silica thin layer is obtained. In addition, we can remove the silica thin layer by short HF treatment without damaging back electrodes or maybe a silica thin layer can be left because its influence for optical properties must be negligible. Moreover, electrical properties wouldn't be affected since the silicon frameworks are still connected and actually the silica coverage will be the good surface passivation. And then by SPC process; we can use the completely same process as discussed in Chapter 6; we will be able to achieve the solar cell structure with i-cSi-o for i-layer and high conductive back electrodes.

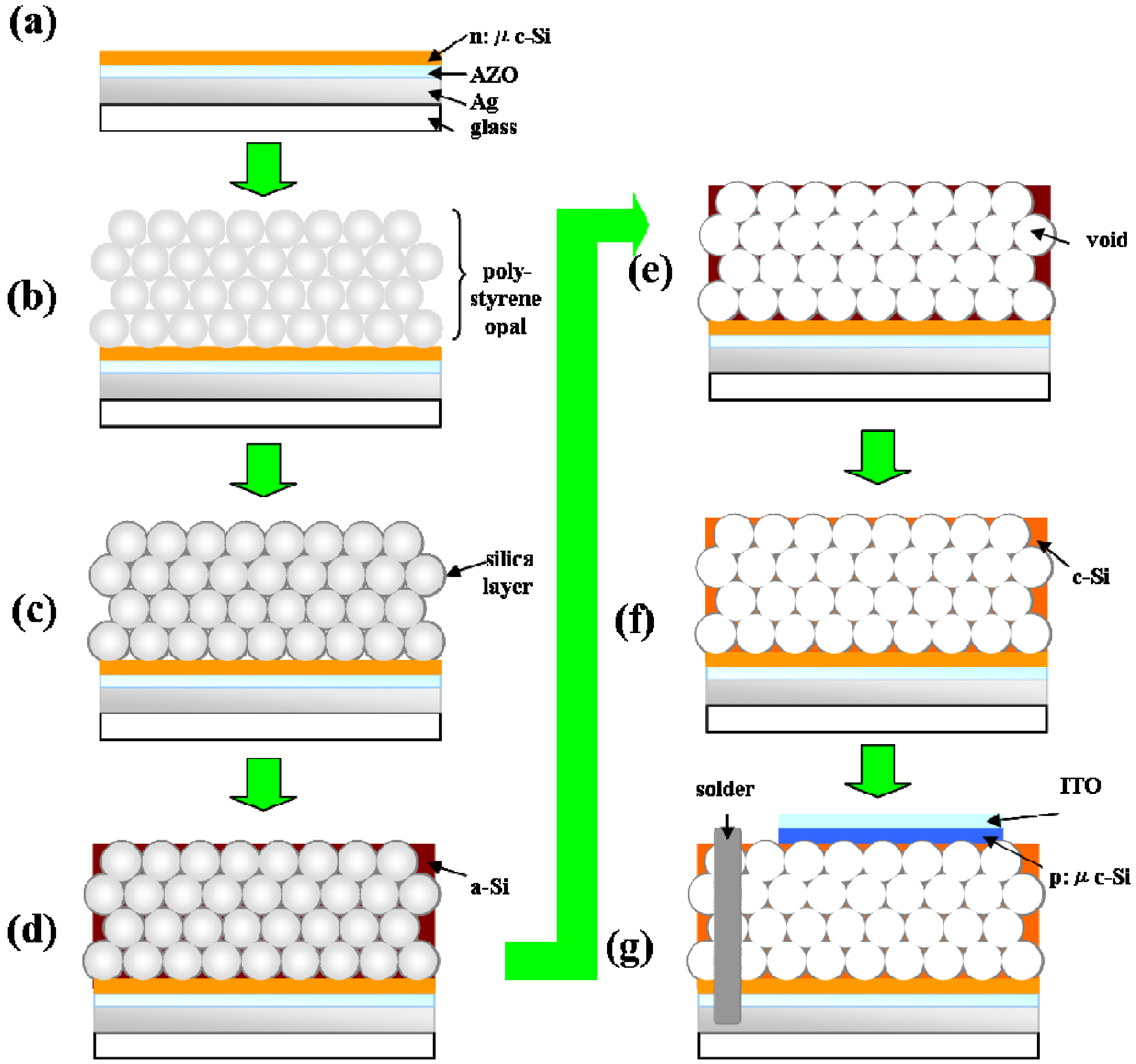

**Figure 7.1** The new process flow for solar cell structure with i-cSi-o for i-layer. Preparations for back electrodes and n: μc-Si layer (a). Polystyrene opal fabrication (b). Silica thin layer coating on polystyrene opal (c). Silicon infiltration and over layer removal by RIE (d). Polystyrene etching (e). SPC and HPP (f). Preparations for p: μc-Si layer, ITO electrode and solder contact (g).

### 7.1.2. Higher Quality Silicon with Photonic Crystals

The process must be cleaner and less contamination is required in semiconductor device especially for minority carrier device such as solar cells. It has a lot of chance to be contaminated at each step of fabrication. We have to improve the processes and optimize sample cleaning process at the each step.

In addition, crystalline silicon quality also must be improved. Instead of SPC silicon, PECVD silicon is attractive in spite of its difficulty for deposition into interstitial voids as it was discussed in Chapter 2. However, it may be possible to solve this problem for dedication of Pulse RF PECVD technique, which was reported for silica deposition instead of silicon into the interstitial voids. [5]

### 7.1.3. Effective Passivation and Activation

As it has been discussed, hydrogen plasma passivation (HPP) is quite effective for improvement of electrical properties for solid phase crystalline silicon. However the executed HPP condition was still elementary condition, which can be optimized more. [4] It's also quite important to activate the doped layers for improvement of the solar cell efficiency, in fact, the rapid thermal annealing (RTA) technique has been investigated and showed its good performance.[6]

## 7.2 Synergy with Quantum Dots

Many approaches for so called "third generation solar cells" have been investigated, [7-9] however every study is still at a primary stage, which hasn't shown actual improvement for the conversion efficiency. The third generations usually apply "quantum dots (QD)" or "nano dots" to their concepts for manipulation of photon or exciton, and those effects have been observed in spite of their low yields of effect. It is indispensable for the realization of "third generation solar cells" to enhance the effect from QD and collaboration with photonic crystals must be a good candidate to solve this issue.

### 7.2.1. Intermediate Band Structure

To capture and use photons having energies lower than the bandgap energy, intermediate band (IB) solar cells can be used that are based on the so-called IB materials.[8] These materials are characterized by the existence of an IB located between conduction band (CB) and valence band (VB) of a conventional semiconductor (Figure 7.2). QDs have been proposed [10] as one of the means of manufacturing the IB solar cell. The basic structure of QD-IB solar cell prototype cells consists of 10 layers of InAs/GaAs QDs sandwiched by p and n GaAs emitters and grown by molecular beam epitaxy in the Stranski - Krastanov growth mode.[11] However, the contribution to the total current of the cell below bandgap energy photons is small (1%). In this case, poor absorption; because carrier (electron) can not be caught to intermediate band gap easily and carrier is deactivated immediately on intermediate band gap by recombination; provided by the QDs is unable to overcome the open - circuit voltage loss.

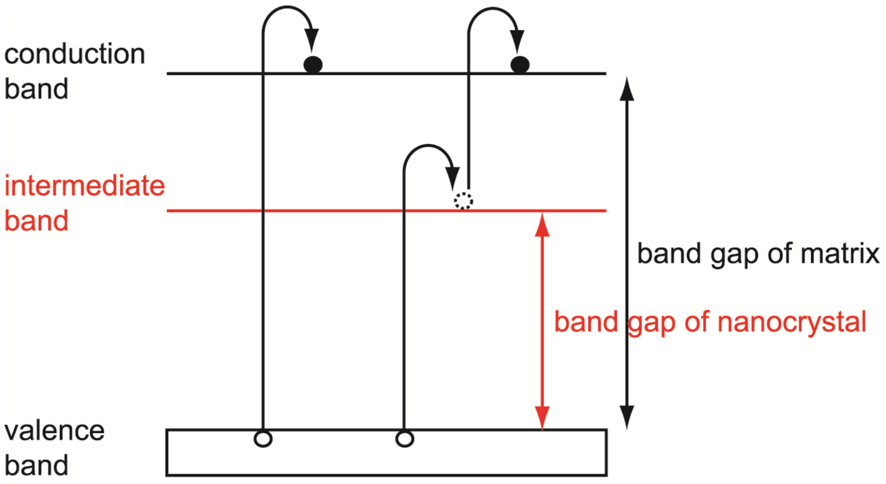

**Figure 7.2** Structure of intermediate band

I'm proposing new way to overcome this poor absorption by utilizing photonic crystals. Figure 7.3 shows the sketch of the concept for collaboration with inverse silicon opal and QDs, especially nano-crystal germanium (ncGe). There are possibilities such that (a) ncGe creates intermediate bandgap (0.67eV) in the bandgap (1.12eV) of inverse silicon opal (i-Si-o), (b) the carrier is captured into intermediate bandgap by the effect of slow photon and comprehensive effect of i-Si-o and (c) the carrier is stabilized by inhibiting light radiation due to recombination at photonic band of i-Si-o. This approach is quite unique and further studies and improvements are underway.

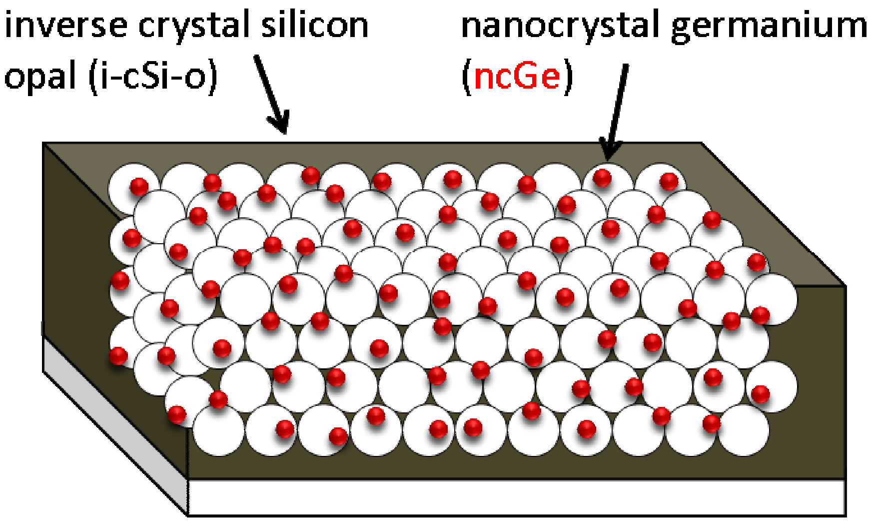

**Figure 7.3** The sketch of the concept for collaboration with inverse silicon opal and QDs.

### 7.2.2. Spectrum modification

Spectrum modification is a well researched topic in physics and in chemistry and has been applied, for example to infrared quantum counter (IRQC) [12] or efficient lamp phosphors [13]. It is also one of the third generation concepts suggested to overcome the classical efficiency limit of silicon solar cells [14]. While the classical efficiency limit is currently estimated to be 29% [15], detailed calculations show that this could improve to approximately 37% [16,17] using spectrum modification at one sun. There are three ways in which the cell efficiency of silicon solar cells may be improved by better exploitation of the solar spectrum; down-conversion (cutting one high energy photon into two low energy photons), photoluminescence (shifting photons into wavelength regions better accepted by the solar cell) and up-conversion (combining low energy photons to one high energy photon). Every approach apply QD doped rare-earth ion for spectrum modification. However the improvement of conversion efficiency hasn't been observed in spite of observation of spectrum modification since its effect is still very primary and low.

I also believe that it is possible to overcome this problem and enhance the effect collaborating inverse silicon opal with QD. There is a possibility that the photon is stabilized by inhibiting light radiation with photonic band of i-Si-o and that stabilized photon get higher chance to progress next step for spectrum modification. This approach is also quite promising, and further studies and improvements are underway.

## 7.3 Other Concepts for Device Application

Lastly, I present some other concepts for device application in this section.

### 7.3.1. Inverse pin Junction Opal Solar Cells

Figure 7.4 shows the different concept to utilize opal structure for solar cell. Instead of silica microspheres, zinc oxide (ZnO) microspheres are used for opal building blocks. ZnO is the one of the most familiar transparent conductive oxide (TCO), and its refractive index is 2. ZnO opal is formed on ZnO coated glass, and then n or p thin layer infiltrate into the interstitial void of ZnO opal. Intrinsic amorphous silicon germanium (a-SiGe) film is infiltrated on thin n (or p) layer with thickness of 30 to 50 nm and then p (or n) thin layer infiltration is proceeded. To collect the photo-current, aluminum (Al) thin layer infiltrated on p (or n) thin layer and this Al layer has the continuous connection to the another side of the opal (back side). This structure has micro p-i-n junction and both side electrode to collect the photo-current. In this structure, the contrast of refractive index is more than 2.2 (a-SiGe: n ~4.5), that contrast can open the complete photonic band even the opal is not removed. In addition, a-SiGe has very high absorption for visible range; because it has the optical bandgap around 550 nm and direct transition; therefore even thin layer such as 30 to 50 nm can generate enough photo-current, and this huge surface structure and photonic crystals properties can enhance the photo-current as well.

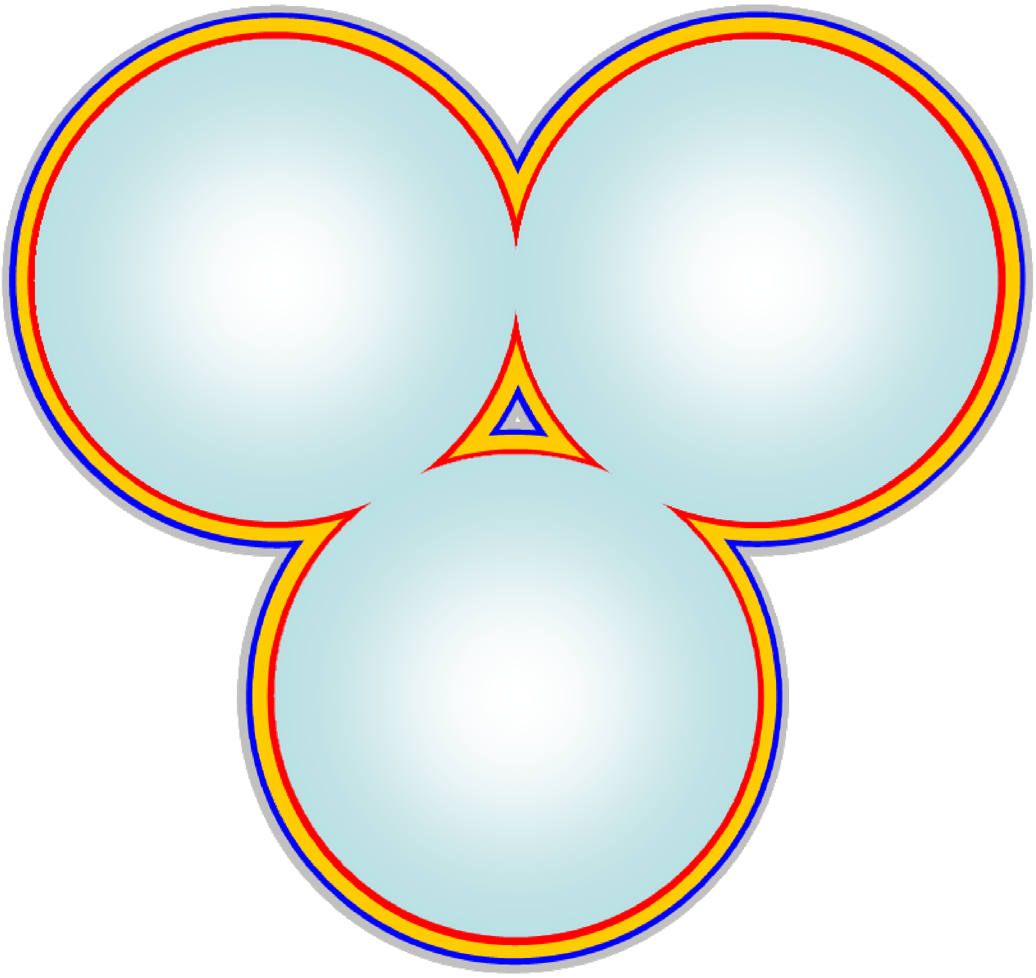

**Figure 7.4** The structure of new concept for solar cell. The light blue spheres are ZnO microspheres. On the ZnO, n (or p) thin layer (red), i-type a-SiGe layer (orange), p (or n) thin layer (blue) and Al thin layer (light gray) formed in this order.

### 7.3.2. Nano materials for LED or LD application

Nano materials have quite different feature from the bulk materials because of the finite number of atoms and the influence of the borders. There are many researches to utilize nano materials for device application especially to optical device such as light emitting diodes (LED) or laser diodes (LD), however it needs precise size control and mono dispersion; it's difficult to achieve by chemical synthesize or physical top down process; to realize the device application. I propose new way to prepare nano materials with fine dispersion and uniform size in Figure 7.5. At the formation of inverse silicon opal, the thickness of silicon layer on silica microsphere surface depends on the diameter of silica microspheres since the interstitial void size is determined by the size of silica microspheres. Therefore, it's possible to create mono disperse nano silicon, that is placed in 3D ordered photonic structures, which is able to be utilized for optical enhancement. Of course, not only for silicon but also for other materials, this concept can be applied.

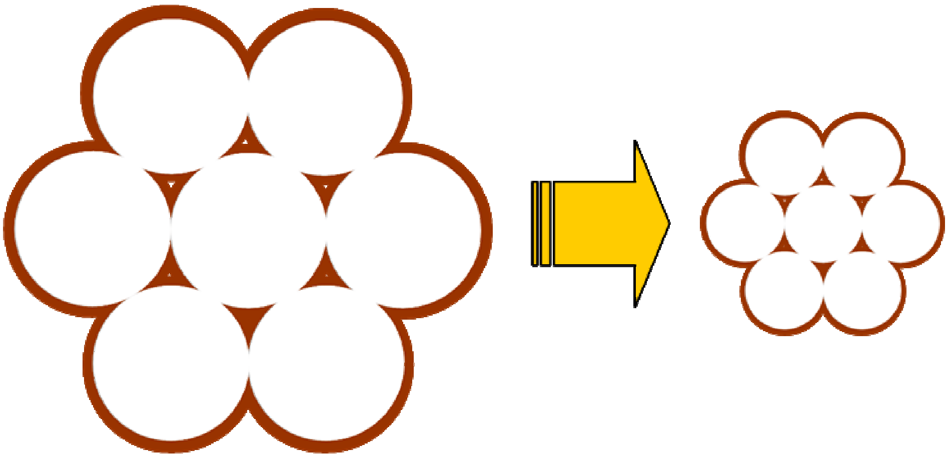

**Si thickness depends on the diameter of spheres for opal template.**

**Si thickness = 0.0773 × (sphere diameter)**

**Small sphere size template gives mono disperse nano Si with 3D ordered structure.**

**Figure 7.5** The new way to prepare nano materials with fine dispersion and uniform size by utilizing inverse opal structure.

## 7.4 References

[1] M. J. Keevers, A. Turner, U. Schubert, P. A. Basore and M. A. Green, Proc. 20th European Photovoltaic Solar Energy Conf., Barcelona, 1305, **2005**.

[2] Nishimura, S.; Shishido, A.; Abrams, N.; Mallouk, T. E. Appl. Phys. Lett. 2002, 81, 4532.

[3] Kishimoto, H.; Takahama, K.; Hashimoto, N.; Aoi, Y.; Deki, S. J. Mater. Chem. 1998,

8, 2019.

[4] H. Míguez, N. Tétreault, B. Hatton, S. M. Yang, D. Perovicb and G. A. Ozin, Chem. Commun., 22, 2736, **2002**

[5] Q. Wu, A. D. Ross, K. K. Gleason, Plasma Process. Polym. **2005**, 2, 401–406

[6] B. Rau, T.Weber, B. Gorka, P. Dogan, F. Fenske, K.Y. Lee, S. Gall and B. Rech, Mater. Sci. Eng. B (2008), doi:10.1016/j.mseb.2008.05.007

[7] R.J. Ellingson, M.C. Beard, J.C. Johnson, P. Yu, O.I. Micic, A.J. Nozik, A. Shabaev, and A.L. Efros, Nano Lett. 5 (2005) p. 865.

[8] A. Luque and A. Martí, Phys. Rev. Lett. 78 (1997) p. 5014.

[9] C. Strümpela, , M. McCanna, G. Beaucarneb, V. Arkhipovb, A. Slaouic, V. Švrčekc, C. del Cañizod, I. Tobias, Solar Energy Materials & Solar Cells 91 (2007) 238–249

[10] A. Martí, L. Cuadra, and A. Luque, in Proc. 28th IEEE Photovoltaics Specialists Conf. (IEEE, Piscataway, NJ, 2000) p. 940.

[11] Y. Nakata, Y. Sugiyama, and M. Sugawara, in Self - Assembled InGaAs/GaAs Quantum Dots, Semiconductors and Semimetals, Vol. 60, edited by M. Sugawara (Academic Press, San Diego, 1999) p. 117.

[12] N. Bloembergen, Phys. Rev. Lett. 2 (3) (1959) 84.

[13] C. Ronda, J. Alloys Compd. 225 (1995) 534.

[14] M. Green, Third Generation Photovoltaics, Springer, Berlin, 2003.

[15] R. Swanson, Approaching the 29% limit efficiency of silicon solar cells, in: 31th PVSC, Orlando, Florida, 2005.

[16] T. Trupke, M. Green, P. Wu¨ rfel, J. Appl. Phys. 92 (3) (2002) 1668.

[17] T. Trupke, M. Green, P. Wu¨ rfel, J. Appl. Phys. 92 (7) (2002) 4117.